Charles University in Prague
Faculty of Mathematics and Physics

DOCTORAL THESIS

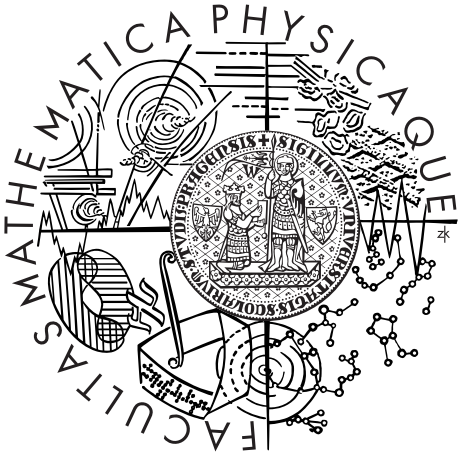

Josef Hanuš

Asteroid Models from Sparse Photometry

Astronomical Institute of the Charles University

Supervisor of the doctoral thesis:	Mgr. Josef Ďurech, Ph.D.
Study programme:	Physics
Specialization:	Theoretical physics, astronomy and astrophysics

Prague 2013

First of all, I thank my supervisor Josef Ďurech for allowing me working on this interesting topic and giving me precious guidance. I thank Marek Wolf, the director of the Astronomical Institute of the Charles Universithy, for providing me ideal working conditions; Miroslav Brož for his help with the research presented here; Franck Marchis for providing me adaptive optics images from the Keck II telescope and for the hospitality during my week stay at the SETI Institute; my colleagues Brian Warner, David Polishook, Benoit Carry, Anna Marciniak, Petr Mat Pokorný, Jaroslav Pat Haas; my co-authors; observers of asteroids, without which there would be no results in this Thesis, our secretary Hana Mifková, the staff of the Astronomical Institute, and of course, I thank my beloved family.

I declare that I carried out this doctoral thesis independently, and only with the cited sources, literature and other professional sources.

I understand that my work relates to the rights and obligations under the Act No. 121/2000 Coll., the Copyright Act, as amended, in particular the fact that the Charles University in Prague has the right to conclude a license agreement on the use of this work as a school work pursuant to Section 60 paragraph 1 of the Copyright Act.

In Prague January 25, 2013 .....

Název práce: Modely planetek z řídké fotometrie

Autor: Josef Hanuš

Katedra: Astronomický ústav UK

Vedoucí disertační práce: Mgr. Josef Ďurech, Ph.D., Astronomický ústav UK

Abstrakt: Zkoumáme fotometrickou přesnost řídkých dat astrometrických přehlídek, jež jsou volně k dispozici díky databázi AstDyS. Řídka data ze sedmi astrometrických přehlídek s nejlepší fotometrickou přesností používáme v kombinaci s hustou relativní fotometrií a metotodou inverze světelných křivek odvozujeme ∼300 nových fyzikálních modelů planetek (tzn., konvexní tvary a rotační stavy). Pro ověření věrohodnosti nových modelů představujeme několik metod jejich testovaní. Dále zkoumáme rotační vlastnosti našeho vzorku planetek hlavního pásu (∼450 modelů odvozených zde nebo převzatých z databáze DAMIT), zaměřujeme se převážně na rozdělení směrů rotačních os v prostoru. Z našeho vzorku modelů je zřejmé, že malé planetky ($D \lesssim 30$ km) mají značně neizotropní rozdělení směrů rotačních os, a to i po odstranění vlivu metody inverze světelných křivek: většina rotačních os směřuje mimo rovinu ekliptiky. Pozorovanou anizotropii vysvětlujeme jako výsledek působení negravitačních sil na tato tělesa (YORP efekt), jelikož bez započtení těchto sil nedokážeme zreprodukovat pozorované rozdělení rotačních os pomocí našeho modelu vývoje rotačních stavů planetek. Odhadujeme též rozměry pro 41 a 10 planetek škálovaním jejich konvexních modelů pomocí snímků pořízených adaptivní optikou a pozorovaní zákrytů hvězd planetkami.

Klíčová slova: Řídká fotometrie – planetky – konvexní modely tvaru

Title: Asteroid Models from Sparse Photometry

Author: Josef Hanuš

Department: Astronomical Institute of the Charles University

Supervisor: Mgr. Josef Ďurech, Ph.D., Astronomical Institute of the Charles University

Abstract: We investigate the photometric accuracy of the sparse data from astrometric surveys available on AstDyS. We use the data from seven surveys with the best accuracy in combination with relative lightcurves in the lightcurve inversion method to derive ∼300 new asteroid physical models (i.e., convex shapes and rotational states). We introduce several reliability tests that we use on all new asteroid models. We investigate the rotational properties of our MBAs sample (∼450 models here or previously derived by the lightcurve inversion), especially the spin vector distribution. It is clear that the smaller asteroids ($D \lesssim 30$ km) have strongly anisotropic spin vector distribution even when we remove the bias of the lightcurve inversion, the poles are clusterred towards ecliptic poles. We explain this anisotropy as a result of non-gravitational torques (YORP effect) acting on these objects, because without accounting this torque, we were not able to create such anisotropic distribution by our model of the spin evolution. We also estimate sizes for 41 and 10 asteroids by scaling their models to fit the adaptive optics profiles and occultation observations, respectively.

Keywords: sparse photometry – asteroids – convex shape models

Contents

Preface

Over the past decade, more than one hundred asteroid models were derived by the lightcurve inversion method. This method was developed by Kaasalainen and Torppa (2001) and Kaasalainen et al. (2001) and it allows us to derive physical models of asteroids (the rotational state and the convex shape) from their disk-integrated photometry. We briefly describe this method in Chapter 2. Measured by the number of derived models, lightcurve inversion has become the leading method for asteroid shape determination. Parameter data sets (rotational states, shapes) combined from results based on different methods are affected by complicated (usually unknown) biases and thus are difficult to interpret.

By having a larger number of models with known physical properties based only on one method, we can gain a better insight into the nature of individual objects and into the whole asteroid population such as near-Earth asteroids (NEAs), main-belt asteroids (MBAs) or even individual families. Current distributions of periods and spin axes are the direct result of the evolution of these objects starting with their formation until the present time (several hundreds of Myr to $\sim$ 4 Gyr for most studied asteroids) and can be used, e.g., for comparison with results from numerical simulations of asteroid temporal evolution. The knowledge of the shape can be used for several purposes, e.g.: (i) in the construction of a thermal model (e.g., Müller et al. 2011), where values for geometric albedo, size, and surface properties can be determined, (ii) a sample of real shapes instead of a synthetic one can be used for the statistical study of the non-gravitational forces (Yarkovsky and YORP effects), (iii) in combination with stellar occultations by asteroids, when these events (observed for hundreds of asteroids) give us additional information about the shape (e.g., non-convexities) and can lead to a size estimate with a typical uncertainty of 10% (see Ďurech et al. 2011), or (iv) in combination with disk-resolved adaptive optics images, where the size can be also determined.

Prior this Thesis, majority of derived asteroid models was based on dense photometric data (about hundred models). Since 2008, the number of such new models grew very slowly (less than 10 per year) because of the limited amount of new dense photometric data. To overcome this difficulty, we focus on sparse photometric data produced, as a by-product, by astrometric surveys. These data are publicly available on AstDyS site (Asteroids, Dynamic Site).

The aim of this Thesis is to study the properties of the currently available sparse data and derive, by the lightcurve inversion method, as many asteroid models as possible. Because of the huge amount of sparse data, we have to automatize the pipeline of the data download, the data processing, and the model derivation and testing. We also have to optimize the lightcurve inversion scheme to

be ready for new sparse photometric data that are or will be produced by projects Pan-STARRS, Gaia satellite or Large Synoptic Survey Telescope (LSST).

In Chapter 3, we gather and investigate the sparse data available on AstDyS. Only data from seven astrometric observatories appear to be enough accurate to be used in the lightcurve inversion. These sparse data are combined together with all available relative data. About 300 new asteroid models derived by the lightcurve inversion are presented in Chapter 5. The reliability of new models is carefully tested by several tests described in Chapter 4. In Chapter 6, we analyze asteroid rotational parameter properties. Finally, in Chapter 7, we scale in size some of the derived shape models by their stellar occultation measurements or disk-resolved adaptive optics images.

Chapter 1

Introduction

1.1 Asteroids

Our solar system is filled with millions of objects in the size range between several meters to a few thousand kilometers. According to the definition of the International Astronomical Union (IAU), we call these objects small solar system bodies (SSSBs) and subdivide them into asteroids, centaurs (orbiting between Jupiter and Neptune), Neptune trojans, transneptunian objects (TNOs) and comets. In August 2006, IAU defined a new class of objects: a dwarf planet, where Ceres, a former asteroid, Pluto, a former planet, and Eris were included. In this work, we mainly study *asteroids* (from Greek asteroeidēs, "star-like") where belong:

- Objects between the orbits of Mars and Jupiter with semi-major axes of 2.1–3.2 AU[1]. These so called main-belt asteroids (MBAs) are surrounded by the secular ν_6 resonance with Saturn and the 2:1 mean motion resonance with Jupiter. In the primordial solar nebula, several planetesimals were created between Mars and Jupiter, but instead of merging together and creating another terrestrial planet, these planetesimals underwent a violent collisional evolution because of the gravitational perturbations of giant planets, and most of them shattered. This process is still in progress. The asteroid families represent the direct evidence of past collisional events, when large bodies were disrupted into millions of smaller fragments. Objects smaller than ∼50 km are then affected by non-gravitational forces and consequently removed from the main belt via the resonances. According to current estimates, there are more than one million objects larger than one kilometer among MBAs. Typical albedos (the fraction of the scattered and incident solar radiation) are ∼10–20% for objects in the inner part of the main belt (silicate composition) and ∼5% for objects in the outer part (carbonaceous composition).

- Objects in the 1:1 mean motion resonance with Jupiter – the Jupiter trojans. Their albedos are very low (∼2–5%), suggesting a composition of ice and dust similar to comets. Their numbers are comparable to that of MBAs:

[1] An astronomical unit, 1 AU is the mean Sun-Earth distance, recently defined by IAU to 149 597 870 700 meters

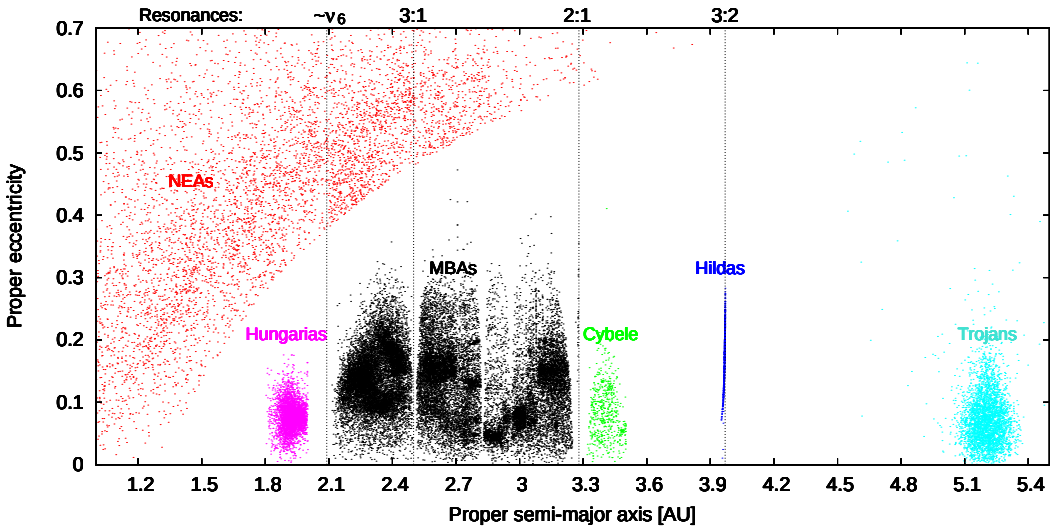

Figure 1.1: *Asteroids in the inner solar system: Proper semi-major axes and proper eccentricities for 6 300 NEAs, 4 424 Hungarias, ∼30 000 MBAs, 588 Cybeles, 836 Hildas and 5 188 Jupiter trojans. Vertical lines correspond to major resonances. Proper elements were taken from AstDyS catalog (Novaković, Knežević and Milani, October 2009).*

about a million larger than one kilometer. So far, only ∼5 000 trojans are known (because of their distance and low albedos).

- Objects behind the main belt in the 3:2 (Hildas, about 1 000 known members) and 4:3 (Thule, 3 objects) mean motion resonances with Jupiter.

- The Cybele group, which consists of objects behind the main belt with semi-major axes 3.3–3.5 AU.

- Hungaria asteroids, which are orbiting the Sun between 1.8 and 2.0 AU.

- Objects which orbits intersect the orbits of terrestrial planets. In the case of the Earth orbit, we call them near-Earth asteroids (NEAs). There are more than 6 000 known NEAs. There should be in total ∼1 000 objects larger than one kilometer orbiting in the terrestrial planets space.

In Figure 1.1, we show the orbital properties (proper semi-major axis vs. proper eccentricity) of major asteroid classes in the inner solar system.

1.2 Photometry

The important source of information about asteroid physical parameters is photometry. The photometry can be divided into disk-integrated, where we measure the total brightness of the object, and disk-resolved. The second case is currently possible only by a few biggest telescopes with adaptive optics systems (such as Keck, VLT or Gemini telescopes) and the Hubble Space Telescope (HST).

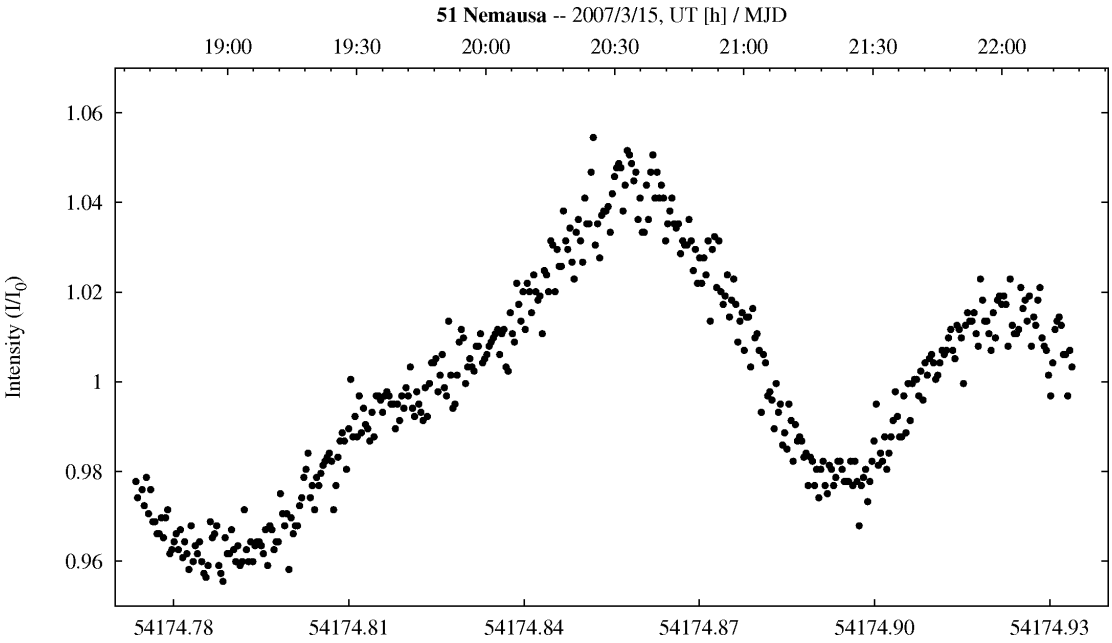

Figure 1.2: *Dense disk-integrated photometry of asteroid (51) Nemausa observed by Marek Wolf and Josef Hanuš at Ondřejov observatory.*

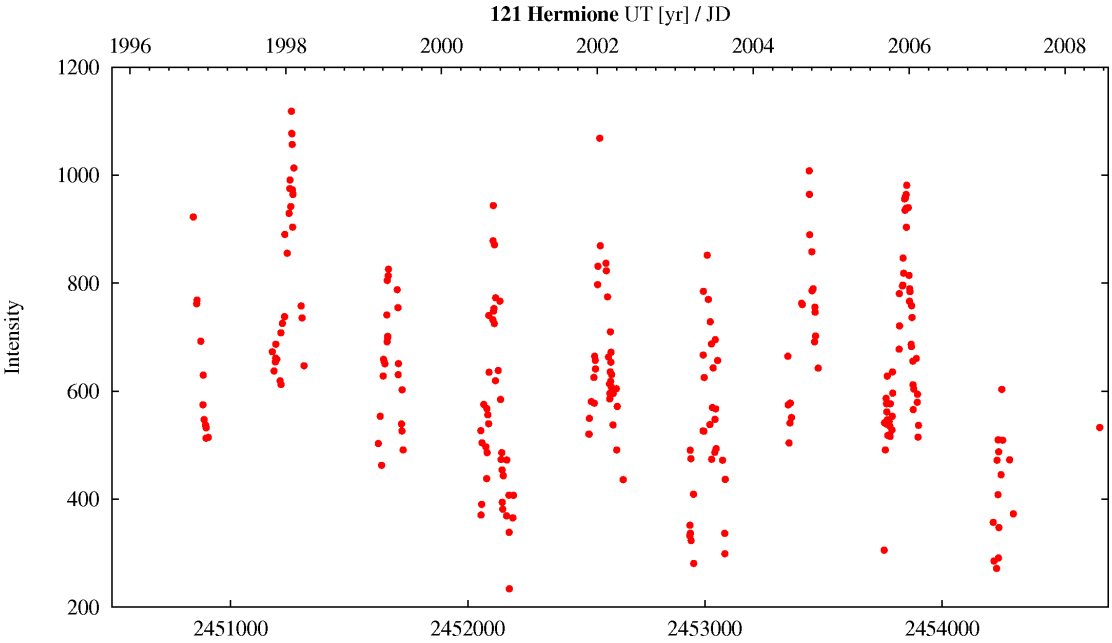

Figure 1.3: *Sparse disk-integrated photometry of asteroid (121) Hermione from USNO-Flagstaff station (IAU code 689).*

We call the time evolution of asteroid brightness *a lightcurve*. The brightness (we are interested in the visual and the very near infrared part of the light spectra) is changing for several reasons:

- The usually non-spherical asteroid is rotating around its rotational axis, and so the illuminated part of the body with respect to the observer is changing. For single objects observed near the opposition[2], we have a typical double sinusoidal pattern.

- The geometry of observation affects the brightness of the asteroid. The closer to the opposition the asteroid is, the brighter it gets, because the part of the surface both illuminated by the Sun and observable from the Earth has its maximum there (the geometry of observation can be described by the solar phase angle, which is the Sun–asteroid–Earth angle). The solar phase angle is close to zero near the opposition. Typical photometric observations of main-belt asteroids are taken with solar phase angles $\lesssim 30°$. Lightcurves observed at larger phase angles are more affected by the shape irregularities and thus are more far from the double sinusoidal pattern.

- Albedo influences the absolute brightness of the asteroids, but has the same effect as the dimension of the object: increasing albedo is equivalent to expanding the body and vice versa.

- The scattering parameters describe how the surface reflects the incident light. Several scattering laws can be found in the literature, some of them are described in Section 2.3.6. The opposition effect is an example of a light scatter where the lack of shadowing and the coherent backscattering close to the opposition cause a significant growth (usually described by an exponential function) of the asteroid brightness.

Two different types of disk-integrated photometry are used: (i) *dense-in-time*, which typically consists of tens to a few hundreds of individual data points observed during one revolution (typically several hours), and (ii) *sparse-in-time*, where the typical separation of individual measurements is large compared to the rotation period. For sparse data, we usually have a few measurements per night in a particular sequence (e.g., for data from the Catalina Sky Survey project, we have typically four individual observations separated by $\sim$ 20 minutes). Under sparse data, we usually mean photometry produced by astrometric sky survey projects. There is no exact boundary between dense and sparse data, because of course, one can create an observational strategy that is in some aspects similar to both dense and sparse data. Based on the type of the photometry, we use the terms "dense lightcurves" and "sparse lightcurves".

Dense data well define the rotational period. Dense lightcurves are typically observed by different "backyard" observers, but also by professionals, who, for example, dedicate their observational campaigns to particular asteroid groups.

[2]We use the terms opposition for the geometry when the Sun, the Earth and the asteroid lie on a straight line or close to this configuration, and apparition for the time of several months, when the asteroid is observable from the Earth (i.e., one observational season).

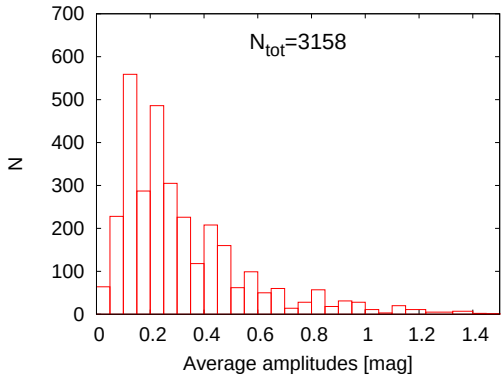

Figure 1.4: *Histogram of average amplitudes for 3 158 asteroids based on the Minor Planet Lightcurve Database (Warner et al. 2009).*

The information about the absolute calibration of the dense lightcurves is usually missing or not reliable, and thus we use this photometry only as relative. Lightcurves from one apparition (i.e., one observational season, typically ∼3–4 months) can be processed by the Fourier analysis and the synodic rotational period can be easily found. On the other hand, sparse data usually cover a long time interval, typically over several apparitions, and carry information about brightness variations for different geometries, which constrains the pole orientation.

A typical example of a dense lightcurve is plotted in Figure 1.2, and of a sparse lightcurve in Figure 1.3.

A priori information about rotational periods of asteroids plays an important role in the process of the model determination. When an approximate period is known, we search for the solution near this value (details in Section 5.1) and thus we considerably save computational time. We use the latest update of the Minor Planet Lightcurve Database[3] maintained by Warner et al. (2009) to check for previously derived periods. For most asteroids, only sparse data from different astrometric observatories are available but no dense lightcurves.

Sparse photometric measurements are produced by many astrometric surveys, but mostly as a by-product. In most cases, asteroid magnitudes are given to only one decimal place, i.e., the accuracy is 0.1 mag at best. Whether or nor this is sufficient for a unique shape determination for reasonable number of asteroids can be deduced from the asteroid lightcurve amplitudes distribution. We used lightcurve amplitude data for 3 158 asteroids from the Minor Planet Lightcurve Database and found that about a half of the asteroids have average lightcurve amplitudes greater than ∼0.25 mag. For 20% of asteroids, their amplitudes are even greater than ∼0.5 mag. The histogram of the average amplitudes is plotted in Figure 1.4. This means that, in principle, photometry with an accuracy of ∼0.1 mag carries sufficient information about rotational states and shapes for a significant number of asteroids.

[3] `http://cfa-www.harvard.edu/iau/lists/LightcurveDat.html`

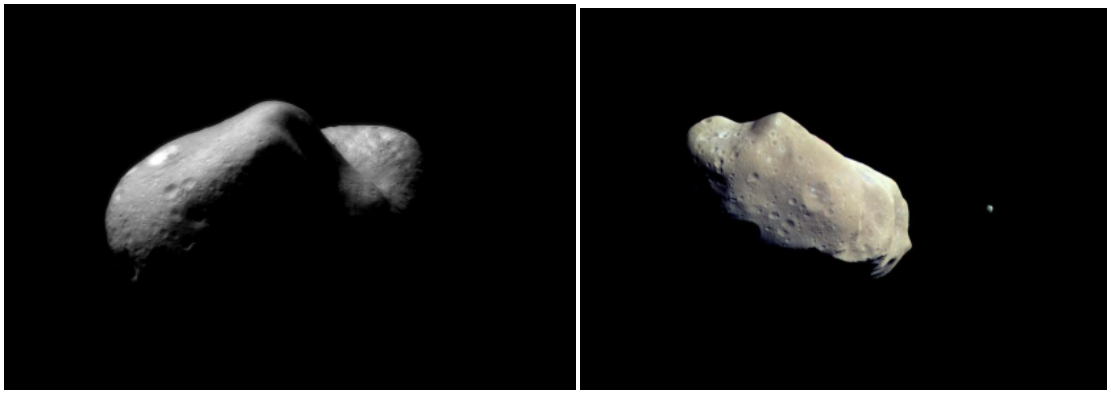

Figure 1.5: Left panel: *Asteroid (433) Eros imaged by NEAR Shoemaker, NASA.* Right panel: *Asteroid (243) Ida with its moon Dactyl observed by Galileo, NASA.*

1.3 Physical models of asteroids

Orbital parameters are currently known for more than 500 000 asteroids. On the other hand, rotational states and shapes were determined only for a small fraction of them. In the Minor Planet Lightcurve Database, periods for $\sim 3\,500$ asteroids are stored. Shapes and spin vectors have been determined, prior this work, only for ~ 100 asteroids.

Most detailed shapes can be determined by the space probe flybys. So far (January 2013), 11 asteroids were visited and photographed by several space probes, such as near-Earth asteroid (433) Eros by NEAR Shoemaker or main-belt asteroid (243) Ida with its moon Dactyl by Galileo (Fig. 1.5). The typical asteroid shape is non-spherical with non-convex features, the surface is covered by impact craters of diverse sizes (the largest recorded craters have diameters of a third of the whole asteroid sizes) and boulders, we can also see long and deep valleys and sharp edges. The largest asteroids are not far from a spherical or tri-axial ellipsoidal shape (some of them are even differentiated), on the other hand, smaller asteroids are more irregular.

The shape can be successfully derived also from radar observations. Shape models that describe global features and contain no information about low-scale structures such as craters are usually presented, see e.g., Ostro et al. (2000, 2002); Chapman (2002); Cheng (2002). However, radar observations of some NEAs taken during their close encounters (e.g., Toutatis in 2012) revealed structures reminding craters and boulders. The interpretation of such features is still unclear and cannot be successfully modeled by curent models. In Figure 1.6, we show radar observations of asteroid (216) Kleopatra and its shape model.

Disk-resolved images and stellar occultations give us momentary two-dimensional shape projections of the asteroids. Disk-resolved images of asteroid (4) Vesta observed by the Hubble Space Telescope (Fig. 1.7) reveal the non-spherical nature of this large ($D = 525$ km) body. Such observations can also expose non-convexities and constrain the size. Asteroids can be resolved only by a few ground based 8-10m class telescopes equipped with adaptive optics systems (VLT, Keck, Gemini) or Hubble Space Telescope. On the other hand, stellar occultations such

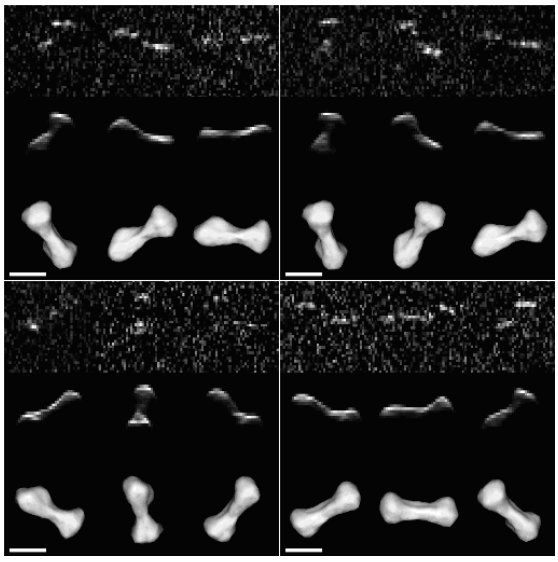

Figure 1.6: *Radar observations of asteroid (216) Kleopatra and its reconstructed "bone-like" shape model. Each quadrant shows Arecibo delay-Doppler images (top), corresponding images calculated from the shape model (middle), and corresponding plane-of-sky views of the model (bottom), Ostro et al. (2000).*

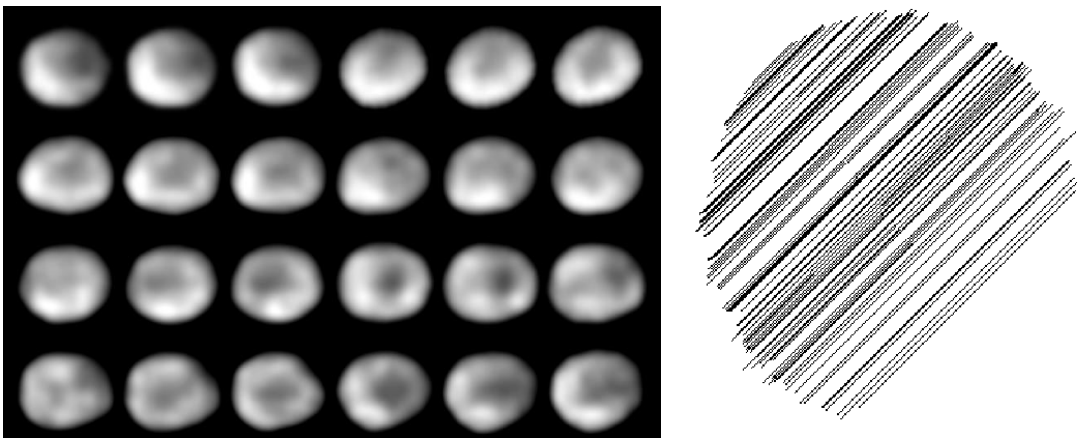

Figure 1.7: Left panel: *Series of disk-resolved images of asteroid (4) Vesta imaged by the Hubble Space Telescope, NASA, 1994.* Right panel: *2D profile of asteroid (2) Pallas reconstructed from several simultaneous observations of the 1983 occultation of 1 Vulpeculae from different locations (Dunham et al. 1990).*

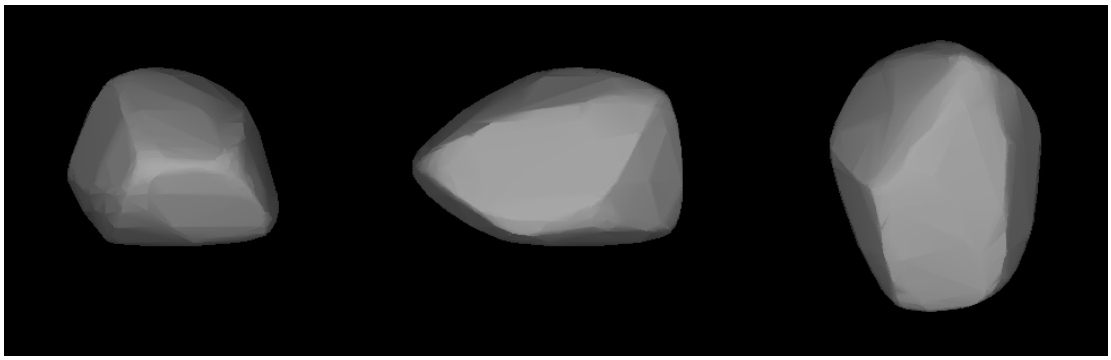

Figure 1.8: *Shape model of asteroid (312) Pierretta based on 4 dense lightcurves (Mohamed et al. 1994) and three sparse lightcurves (from astrometric observatories with IAU codes 689, 703, E12). The first two figures are shown at equatorial view with rotational phases* 90° *apart, the third one is a pole-on view. From Hanuš et al. (2011).*

as the one of (2) Pallas in 1983 (Fig. 1.7) are a domain of amateur observers or semi-professionals.

Shape models of asteroids can be also derived from disk-integrated photometry by the lightcurve inversion method. It is a gradient-based method that allows us to derive also basic physical properties such as the rotational state (see Kaasalainen and Torppa 2001; Kaasalainen et al. 2001, 2002a). The resulting shape model well corresponds to the convex hull of the real shape, so the model is a good global approximation of the asteroid, but does not describe the low-scale surface structures. Convex shapes and spin axis directions were derived, prior this work, only for ~ 100 asteroids, these three-dimensional models of asteroids are available in the Database of Asteroid Models from Inversion Techniques[4] (DAMIT, Ďurech et al. 2010) maintained by the Astronomical Institute of the Charles University in Prague, Czech Republic. A typical example of a convex shape model is plotted in Figure 1.8, it belongs to asteroid (312) Pierretta.

[4] `http://astro.troja.mff.cuni.cz/projects/asteroids3D`

Chapter 2

Lightcurve inversion method

The lightcurve inversion method is a powerful tool that allows us to derive basic physical properties of asteroids (the rotational state and the shape) from their disk-integrated photometry. This photometry can be *dense-in-time* and *sparse-in-time*. All asteroid models derived in this work are based on the lightcurve inversion method developed by Kaasalainen and Torppa (2001) and Kaasalainen et al. (2001).

To obtain a unique spin and shape solution, we need a set of at least a few tens of dense lightcurves observed during at least three apparitions for a MBA. Kaasalainen (2004) showed that we can also use only sparse data for the inversion technique. In such case, a unique model can be derived from more than about one hundred calibrated measurements observed during 3–5 years if the photometric accuracy is better than ∼5% (Ďurech et al. 2005, 2007). Sparse data available so far are not that accurate. Nevertheless, for many asteroids with high lightcurve amplitudes, it is possible to derive their models from current sparse data (see Section 1.2 for more details). We can also combine sparse and dense data to derive models. First results from this approach were presented by Ďurech et al. (2009), where sparse data from the US Naval Observatory in Flagstaff (USNO-Flagstaff station) were used.

Currently (January 2013), there are 213 models of asteroids derived by the lightcurve inversion method that are stored in the Database of Asteroid Models from Inversion Techniques (DAMIT, Ďurech et al. 2010). About a half of these models were derived purely from dense lightcurves, the rest is based on combined dense and sparse data.

In this chapter, we list important historical work dedicated to asteroid shape determination (Section 2.1), define the direct problem, which is based on computing brightness of an object with a know shape (Section 2.2), and describe the convex inverse problem, thus shape determination from a set of lightcurves (Section 2.3.1).

2.1 Historical background

In the early 20th century, there were two hypothesis explaining the temporal brightness evolution of asteroids: (i) the existence of spots on the surface, and (ii) the non-spherical shape. Both hypothesis were investigated by Russell (1906)

with a conclusion that the lightcurve changes are caused by both these effects (i) and (ii). Russell assumed the asteroid in the *opposition* (i.e., with a zero solar phase angle) and showed that the shape cannot be reconstructed, because the solution of the lightcurve inversion is not unique (infinite number of solutions is possible).

Not much progress were made on the lightcurve inversion until the eighties. The main problems were insufficient number of quality observations for different geometries and the poor knowledge of the scattering law. Only simple shape models were used – tri-axial rotational ellipsoid and its modifications. The major progress in the field of the shape modeling was achieved in the last thirty years. Here we summarize basic results:

- Convex two-dimensional projections of asteroids were derived from several lightcurves by Ostro and Connelly (1984) and Ostro et al. (1988).

- Karttunen (1989) and Karttunen and Bowell (1989) studied the influence of small craters and irregularities of the ellipsoidal shape on the lightcurves. This effect was beyond the noise level.

- Pole orientations can be derived from the photometry without the knowledge of asteroid shapes by studying the amplitudes, magnitudes and epochs of the observed lightcurves (a short review of such methods can be found in Magnusson 1986). These methods usually assume a tri-axial ellipsoidal shape model.

- Cellino et al. (1989) approximated the shape by octants from ellipsoids with different axes. Two axes of the accessory ellipsoids were always same. They also presented a systematic analysis of the effect of large-scale deviations from the tri-axial ellipsoidal shape on the lightcurves.

- The first general analysis of the inversion technique was presented in papers by Kaasalainen et al. (1992a,b). This method does not assume an a priori shape model and uses all available photometric data. The only requirements are the convex shape, the knowledge of the scattering law and a large number of lightcurves observed at different geometries. The quality of the data and their variety are essential for the stability and uniqueness of the solution. A quality data set can lead to a shape model that is very close to the convex hull of the real shape. This method was successfully used on real data of two asteroids.

- Barucci et al. (1992) presented a shape model of asteroid (951) Gaspra derived by three different approaches: by the method of Kaasalainen et al. (1992a,b), of Cellino et al. (1989) and of their own, which finds the best ellipsoidal approximation and then removes parts of the shape, adds craters, etc. The results were compared with the images acquired by the space probe Galileo: all three methods gave reliable results.

- After the important theoretical work was done, several papers with shape models and asteroid physical parameters derived by the above described

methods were published, e.g,, by Michałowski (1996) and Kryszczynska et al. (1996).

- Models of tumblers and binary asteroids were presented, e.g., by Kaasalainen (2001), Mottola and Lahulla (2000) or Pravec and Hahn (1997).

- A robust and widely applicable inverse technique based on the rather theoretical work of Kaasalainen et al. (1992a) and Kaasalainen et al. (1992b) was developed by Kaasalainen and Torppa (2001); Kaasalainen et al. (2001). All asteroid models in our work are derived by this method, which is described in Section 2.3.

- By far the best shape models are available thanks to several space probes rendezvouses with asteroids, such as Galileo flybys of (951) Gaspra and (243) Ida and the NEAR Shoemaker flyby of (253) Mathilde and its one year orbit around (433) Eros (Veverka et al. 2000). The lightcurve inversion method was in Kaasalainen et al. (2001) validated on asteroids (243) Ida, (433) Eros, and (951) Gaspra, for which images from space probes were available. The convex shape models well corresponded to the convex hulls of the real shapes and the spin axis directions were similar within few degrees. This demonstrates the importance of studying asteroids by different techniques (photometry, radar observations, space probes) to have the possibility of comparing results derived by independent methods and from different data sets. Moreover, combined data allow us to get more information about the objects.

2.2 Direct problem – computing the brightness of an object with the known shape

In order to solve any inverse problem, we need to precisely define the direct problem first. In our case, we want to compute the brightness for an object with the known shape and the geometry of observation (i.e., the location of the object, the Earth and the Sun in the solar system in some reference frame) for particular time epochs that usually correspond to the observational data.

The time evolution of the object brightness $L(t)$ can be described as a function of parameters defining the shape (R_i), the light scattering on the surface (S_j), the rotational state (D_k) and the orbital motion of the observer and the asteroid (O_l, A_m):

$$L(t) = L(R_i, S_j, D_k; O_l, A_m; t). \tag{2.1}$$

The total brightness L of a convex object in a particular time and geometry of observation is given by

$$L(\vec{E}, \vec{E}_0, S_j) = \int_\Sigma S(\mu, \mu_0, \alpha, \vec{P})\, \varpi_0(\vec{r})\, \mathrm{d}\sigma, \tag{2.2}$$

where Σ is a part of the surface both visible from the Earth and illuminated by the Sun, $\mathrm{d}\sigma$ is a surface element, $\vec{r}$ is a radius vector to the surface, $\varpi_0(\vec{r})$ is albedo,

$\vec{E}$ and $\vec{E}_0$ are unit vectors pointing to the observer and the Sun, respectively, $\mu = \vec{E} \cdot \vec{n}$, $\mu_0 = \vec{E}_0 \cdot \vec{n}$, $\vec{n}$ is a unit normal vector of the surface element $\mathrm{d}\sigma$ and $S = S(\mu, \mu_0, \alpha, \vec{P})$ is the scattering law with parameters $\vec{P}$ and α is the solar phase angle. Different types of scattering laws are described in Section 2.3.6, where we also derive the relation (2.2).

For the practical purposes, we need to discretize the Equation (2.2). The shape can be represented by a convex polyhedron with triangular facets, the transformation from the continuous shape to the polyhedron is performed by a standard discretization method, we use the *octant procedure* that is described, e.g., in Kaasalainen and Torppa (2001).

The known facet $\mathrm{d}\sigma$ of the polyhedron contributes to the total brightness L by an element of $\mathrm{d}L$:

$$\mathrm{d}L(\vec{E}, \vec{E}_0, S) = S(\mu, \mu_0, \alpha, \vec{P})\, \varpi_0(\vec{r})\, \mathrm{d}\sigma. \tag{2.3}$$

The total brightness is then a sum over all both illuminated and visible facets:

$$L(\vec{E}, \vec{E}_0, S) = \sum_{i=1}^{p} S(\mu_i, \mu_{0i}, \alpha, \vec{P})\, \varpi_{0i}(\vec{r})\, \Delta\sigma_i, \tag{2.4}$$

where p is the number of all facets. The contribution of facets for which $\mu_i < 0$ or $\mu_{0i} < 0$ is zero, because at the same time, they are not illuminated by the Sun and visible from the Earth.

For non-convex objects, the situation is more complicated. In addition to testing the illumination and visibility of the facet via the positive values of μ a μ_0, we need to account for the shadowing caused by other facets. The total brightness of a non-convex body can be also affected by multiple scattering on facets. A possible numerical algorithm can be found, e.g., in Kaasalainen and Torppa (2001). On the other hand, Lagerros (1997) suggests that the multiple scattering is of a minor importance with respect to the total brightness. The validity of the multiple scattering omission depends on the nature of the solved problem. Generally, the multiple scattering can be neglected for objects with low albedo.

2.3 Convex inversion

Here we present the inversion method of Kaasalainen and Torppa (2001) and Kaasalainen et al. (2001) based on the previous rather theoretical papers of Kaasalainen et al. (1992a,b).

2.3.1 Inverse problem

The idea of the inverse problem is to express the observed asteroid brightness as a function of all quantities that influence it. According to equation (2.1), these quantities are the shape, the surface scattering properties, the rotational state, the geometry of observation and the time. To do that we have to parametrize these quantities by as few parameters as possible. The convex lightcurve inversion problem can be then expressed as:

$$\vec{L} = A\,\vec{g}, \tag{2.5}$$

where $\vec{L}$ is a vector of the observed brightnesses, $\vec{g}$ a vector of parameters to solve and matrix A ties both quantities together. Vector $\vec{g}$ can represent (i) the objects curvature function (commonly called Gaussian surface density), which defines the shape unambiguously, (ii) albedo surface variations or (iii) their multiplication. We usually use the case (i). Vector $\vec{g}$ does not contain parameters of the scattering law.

Two different choices for $\vec{g}$ can be used:

- Areas of facets of a convex polyhedron.
- Coefficients of spherical harmonics series.

Both options are described in the next two Sections (2.3.2 and 2.3.3).

Due to physical reasons, we have to add additional assumptions on the solution: we want to have positive areas of the facets of the convex polyhedron or everywhere positive the curvature function (we model the shape as convex). Both choices of $\vec{g}$ are equivalent. Moreover, the number of parameters has to be large in order to well describe the irregular shape ($\sim$ 1000 polyhedron facets) and to ensure that the solution will not be dependent on the orientations of the surface normals.

2.3.2 Model of the convex polyhedron

Vector $\vec{g}$ represents here the areas of facets of a convex polyhedron (we do not know the vertices). The requirement on positive areas of facets can be expressed as $g_j \geq 0$ for all facets j. Let n_j be an outward normal of the facet j, then we have a convexity constraint:

$$\sum_j \vec{n}_j\, g_j = 0. \tag{2.6}$$

Normals n_j can be chosen freely. In practice, a sphere or an ellipsoid is used: their surface is discretized to a polyhedron with triangular facets (by an octant triangulation) and the normals of these facets are used. In order to avoid the solution dependence on the choice of the surface normals, the number of optimized shape parameters needs to be of the order of thousand. The constraint (2.6) is important for the polyhedron to be formally convex.

By comparing equations (2.4) and (2.5), we get for matrix A:

$$A_{ij} = S_j(\mu^{(ij)}, \mu_0^{(ij)})\,\varpi_j, \tag{2.7}$$

where S_j and ϖ_j denote scattering law and albedo at facet j, i represent the observations, i.e., $\mu^{(ij)} = \vec{E}_i \cdot \vec{n}_j$ and $\mu_0^{(ij)} = \vec{E}_{0i} \cdot \vec{n}_j$. Matrix element A_{ij} is zero if at least one of the quantities $\mu^{(ij)}$ and $\mu_0^{(ij)}$ are lower than or equal to zero.

The problem (2.5) is solved by a standard least-square method by minimization of:

$$\chi^2 = \|\vec{L} - A\,\vec{g}\|^2, \tag{2.8}$$

The relation (2.8) can be solved numerically by standard methods, but we have to assure that for all j, $g_j > 0$. This can be achieved by representing g_j exponentially

$$g_j = \exp(a_j), \tag{2.9}$$

and by optimizing exponentials of parameters a_j. The surfaces of constant χ^2 are convex in the $\vec{g}$-space, so there exists only one vector $\vec{g}$ with all $g_j > 0$ that minimizes the χ^2. From the monotonous nature of the exponential function implies that only one vector $\vec{a}$ corresponds to $\vec{g}$. So, in the exponential formalism, the solution with the lowest χ^2 is unique. The problem is now nonlinear, however, any reasonable optimization method can find the correct solution that corresponds to the lowest χ^2. To minimize (2.8), we use the conjugate gradient method (see Press et al. 1994). By this process, we determine the areas of the facets of the convex polyhedron, but we still do not know the polyhedron itself (we have only areas of the facets and normals to them). To find the vertices of the polyhedron, we use a method called Minkowski minimization.

Minkowski minimization is a numerical method (see, e.g., Kaasalainen et al. 1992a; Lamberg and Kaasalainen 2001) that converts the shape represented by areas of facets and their normals into the shape represented by a convex polyhedron with polygonal facets. This step plays an important role in the lightcurve inversion while it stabilizes the solution. An object can be, in principle, described by a large variety of area facets and their normals. In practice, we can get from the lightcurve inversion even for slightly different initial parameters (from which we converge to the same local minimum) very different area facets. However, the Minkowski minimization produces for all these areas of facets similar shapes represented by the convex polyhedron with triangular facets. This is the reason, why convex inversion is so robust and widely applicable. The stability of the Minkowski minimization allows us also to tolerate a small residuum in the convexity constraint (2.6). This residuum can be compensated by adding a corresponding dark facet to fulfill (2.6). This additional facet is absolutely dark, does not affect the global shape and is important for the successful run of the Minkowski minimization.

In reality, the object brightness is dependent on its distance to the Sun and the Earth, and also on the solar phase angle, the brightness increases towards the opposition. Therefore, it is convenient to re-normalize the lightcurves to unity and solve

$$\chi^2_{\mathrm{ren}} = \sum_i \left\| \frac{\vec{L}^{(i)} - A^{(i)}\,\vec{g}}{\bar{L}^{(i)}} \right\|^2, \tag{2.10}$$

where i corresponds to the individual lightcurves and $\bar{L}^{(i)}$ is the mean brightness of the i-th lightcurve. Different geometries have then the same weights.

2.3.3 Spherical harmonics series

The object's curvature can be represented also by an exponential of spherical harmonics series. In this case, the positivity constraint of the curvature is ensured. The problem (2.5) is again nonlinear, but can be still solved by standard methods. Let us denote

$$G(\vartheta,\psi) = \exp\left(\sum_{l=0}^{\infty}\sum_{m=-l}^{l} a_{lm} Y_l^m(\vartheta,\psi)\right), \tag{2.11}$$

where (ϑ,ψ) are spherical coordinates of the surface normal, Y_l^m a spherical function of degree l and order m and a_{lm} its coefficients. By including albedo variegations into G, we get for the observed brightness:

$$L(\vec{E},\vec{E}_0) = \int_{\Sigma} S(\mu,\mu_0)\, G(\vartheta,\psi)\, \mathrm{d}\sigma. \tag{2.12}$$

We integrate over the area Σ on the unit sphere of normal directions, where $\mu,\mu_0 \geq 0$, $S(\mu,\mu_0)$ is the scattering law and $\mathrm{d}\sigma$ an element of surface on the sphere. The integral can be replaced by a finite sum: we cover the unit sphere by enough triangles, e.g., by an octant triangulation. For the number of facets of the order of thousand, the difference between integral (2.12) and its discretized version is negligible. This process corresponds to neglecting the high order terms of the spherical harmonics expansion. The equation (2.12) is modified to:

$$L(\vec{E},\vec{E}_0) = \sum_i \sum_j S_j(\mu^{(ij)},\mu_0^{(ij)})\, G(\vartheta_j,\psi_j)\, \Delta\sigma_j, \tag{2.13}$$

where j corresponds to individual surface areas, i to the observations and areas $\Delta\sigma_j$ to normals (ϑ_j,ψ_j).

By comparing equations (2.5), (2.7) and (2.13), we get:

$$g_j = G(\vartheta_j,\psi_j)\, \Delta\sigma_j, \tag{2.14}$$

and we solve similar problem to (2.8). In this case, we use the Levenberg-Marquardt optimization scheme (Press et al. 1994). As initial shape for the iteration, a tri-axial ellipsoid is usually chosen.

After we solve the curvature $G(\vartheta,\psi)$, we discretize it in order to represent the areas of the facets of a convex polyhedron. The easiest way to do that is to use g_j directly from the equation (2.14). Vertices of the convex polyhedron can be derived again by the Minkowski minimization.

The advantage of this method is its fast and efficient convergence even with a poor choice of the initial shape. It is convenient to use this method for the first rough shape determination, and then take this shape as an initial guess for the polyhedron model, which greatly profits from a more realistic initial shape model. The strong convergence of the spherical harmonics series model remains, even if we change some parameters from fixed to free and include them into the optimization (e.g., parameters of the scattering law or the rotational state).

2.3.4 Albedo variegations

Large asteroids often have significant albedo variegations on the surface (e.g., asteroid (4) Vesta). The effects of the shape and the albedo on the lightcurves are in principle indistinguishable. As shown by Kaasalainen et al. (1992a,b), it is possible in some special circumstances to determine the albedo variegations on the surface. The observations need to be realized for large solar phase angles

when the shape rather than the albedo is dominant for the lightcurves. Such observations were used, e.g., in the work by Cellino et al. (1987), Degewij et al. (1979) or Drummond et al. (1988a).

On the other hand, it was confirmed by space probes that smaller asteroids have more or less constant albedos. The lightcurve changes are dominated by the shape (Barucci et al. 1989), which can be then quite accurately determined.

A method for determination of the albedo variegations on the asteroid surface was presented, e.g., by Lagerros (1997). The incident light on the asteroid is partly scattered and partly absorbed. The surface is heated and the absorbed energy is lated irradiated in the infrared wavelengths. The parts of the surface with higher absorption irradiate in the infrared more than parts where the scattering dominates (i.e., parts with the higher albedo). In visible wavelengths, the effect is exactly opposite: stronger absorption is responsible for a smaller light scatter. Both infrared and visible lightcurves can be then compared.

After each iteration step of the parameter optimization, the term (2.6) is computed and compensated by a so called dark facet, which does not contribute to the total brightness, but keeps the shape formally convex. If the dark facet is large (more than a few percent), the optimization scheme tries to decrease its value during the next iteration step. Cases when this fails suggest albedo variegations on the surface and more complex analysis can be introduced (see, e.g., paper by Kaasalainen and Torppa 2001).

2.3.5 Absolute vs. relative photometry

The absolute brightness is a function of the solar phase angle. As a result, for each lightcurve there exists a scale factor dependent on the geometry of observation. This dependence is called a phase curve. The object is brighter closer to the opposition. We need to know the phase function to solve equations (2.8) and (2.10). If we are not able to determine the phase curve, we have to use only relative photometry and minimize the measure

$$\chi^2_{\mathrm{rel}} = \sum_i \left\| \frac{\vec{L}^{(i)}}{\bar{L}^{(i)}} - \frac{A^{(i)}\,\vec{g}}{\langle A^{(i)}\,\vec{g}\rangle} \right\|^2, \tag{2.15}$$

where $\langle A^{(i)}\,\vec{g}\rangle$ is a mean brightness of the i-th model lightcurve that fit the i-th observed lightcurve.

Both observed and modeled brightnesses are divided by the mean brightnesses of the corresponding lightcurves and oscillate around unity. In other words, the scale factors of individual lightcurves remain free parameters. The equation (2.15) is convenient if the shape is represented by the spherical harmonics series, because all the scale factors can be omitted and the number of free parameters stays as low as possible. According to Kaasalainen and Torppa (2001), the approach based on (2.15) is reliable and the solution based on the relative photometry is equivalent to the one based on the absolute photometry. The reasons are obvious: the lightcurve appearance is given mainly by the shape and the rotational state. On the other hand, the absolute brightness is connected more with the surface scattering properties. By using (2.15), we in fact separate one set of parameters from the rest.

2.3.6 Scattering laws and phase functions

Here we derive the Equation (2.2), which we use in Section 2.2. This theory is valid for a particular wavelength of the light (monochromatic light), we get the bolometric quantities by integrating over the whole light spectrum. The dependence on the wavelength is not explicitly expressed in the following relations due to transparency.

Let F_{tot} be the total radiative flux density passing from the Sun in the distance of an asteroid per unit area and time. For each unit surface element we have the incident radiative flux density F_{inc}:

$$F_{\mathrm{inc}} = F_{\mathrm{tot}}\,\mu_0, \tag{2.16}$$

where $\mu_0 = \cos\theta_0$, θ_0 is the incident angle. After the scattering we have the flux density F_{scat}.

The amount of teh scattered radiative flux density is dependent on the surface properties. Into a unit solid angle (θ, φ) is scattered the radiative flux density

$$I(\theta,\varphi) = R(\mu_0,\varphi_0,\mu,\varphi)\,F_{\mathrm{tot}}\,\varpi_0, \tag{2.17}$$

where $R(\mu_0,\varphi_0,\mu,\varphi)$ is the reflectance coefficient and ϖ_0 the single-scattering albedo (the fraction between the scattered and the total radiative flux density). $I(\theta,\varphi)$ is usually called intensity.

In practice, rather than $R(\mu_0,\varphi_0,\mu,\varphi)$ the scattering law $S(\mu_0,\varphi_0,\mu,\varphi)$ is used. The scattering law can be defined via the radiation power scattered into the solid angle Ω, for which we have the natural relation

$$\mathrm{d}P_\Omega(\theta,\varphi) = I(\theta,\varphi)\,\mathrm{d}\sigma\,\mu, \tag{2.18}$$

where $\mathrm{d}\sigma$ is the surface element, where the radiation is scattered and $\mu = \cos\theta$, and also via the relation with the scattering law:

$$\mathrm{d}P_\Omega(\theta,\varphi) = S(\mu_0,\varphi_0,\mu,\varphi)\,\mathrm{d}\sigma\,\varpi_0\,F_{\mathrm{tot}}. \tag{2.19}$$

Let Ω_{obs} be the solid angle, for which we see from the location of the scattering the effective area A_{eff} of the observational instrument. Let assume that Ω_{obs} is small and the flux inside is constant. For the observed radiation flux from the surface element, we have

$$\mathrm{d}F_{\mathrm{obs}} = \frac{\mathrm{d}P_\Omega(\theta,\varphi)\,\Omega_{\mathrm{obs}}}{A_{\mathrm{eff}}}. \tag{2.20}$$

Combination of Equations (2.19) and (2.20), and the knowledge that $\Omega_{\mathrm{poz}} = A_{\mathrm{eff}}/r^2$, where r is the distance between the observer and the surface element, give us

$$\mathrm{d}F_{\mathrm{obs}} = \frac{F_{\mathrm{tot}}}{r^2} S(\mu_0,\varphi_0,\mu,\varphi)\,\mathrm{d}\sigma\,\varpi_0. \tag{2.21}$$

In the case of asteroids, the scattering law does not depend on φ and φ_0. If the asteroid distance R from the Sun is known, the total radiative flux density F_{tot} can be computed.

The observed brightness of the surface element $\mathrm{d}L_{\mathrm{obs}}$ can be expressed with the help of the Equation (2.21)

$$\mathrm{d}L_{\mathrm{obs}} = \mathrm{d}F_{\mathrm{obs}} \frac{r^2}{F_{\mathrm{tot}}} = S(\mu, \mu_0)\, \mathrm{d}\sigma\, \varpi_0. \tag{2.22}$$

Here described lightcurve inversion method assumes the explicit knowledge of the scattering law $S(\mu, \mu_0)$. In reality, $S(\mu, \mu_0)$ needs to be parametrized and these parameters need to be somehow included into the optimization process. Accurate and general model describing the surface scattering properties of asteroids with only a few free parameters does not exist. Commonly used scattering models, such as Hapke or Lumme-Bowell (see, e.g., Bowell et al. 1989) are not suitable for solving the inverse problem. For example, these scattering laws can produce ambiguous and unrealistic parameter values (Karttunen and Bowell 1989). If we cannot describe accurately the brightness vs. the solar phase angle relation, fitting absolute photometry is meaningless and we should rather use relative brightnesses instead of absolute. The second reason for using relative photometry is the usually poor accuracy of the absolute photometry caused by the difficult data reduction and by the combination of data from various sources.

To successfully solve the inversion problem, we need to use a scattering law that is as simple as possible, too many parameters cause the instability of the solution. Scattering laws such as Hapke or Lumme-Bowell, which carefully describe the physical surface properties of asteroids, are not needed for the inversion. All we want is to describe only the basic photometric properties of the surface, therefore we can choose a more simple scattering law. We use the relation (see Kaasalainen et al. 2001):

$$S(\mu, \mu_0, \alpha) = f(\alpha)\, [S_{\mathrm{LS}}(\mu, \mu_0) + c\, S_{\mathrm{L}}(\mu, \mu_0)], \tag{2.23}$$

which combines Lommel-Seeliger S_{LS} and Lambert S_{L} scattering laws, the second one is weighted by a factor c. For S_{LS} and S_{L}, we have:

$$S_{\mathrm{LS}} = \frac{\mu\, \mu_0}{\mu + \mu_0}, \tag{2.24}$$

$$S_{\mathrm{LS}} = \mu\, \mu_0. \tag{2.25}$$

The Equation (2.23) becomes:

$$S(\mu, \mu_0, \alpha) = f(\alpha)\, \mu\, \mu_0 \left(\frac{1}{\mu + \mu_0} + c \right). \tag{2.26}$$

Due to practical reasons we multiply the relation for the sum of a single and a multiple scattering by the phase function $f(\alpha)$, which describes the dependence of the asteroid brightness on the solar phase angle α. This approach can be justified by the fact that there is an ambiguity in the process of single and multiple scattering on inhomogeneous material consisting of smaller parts, which are subsequently formed by even smaller parts.

The phase function can be computed from a set of scale factors. Each scale factor corresponds to one photometric lightcurve. For relative lightcurves, the scale factor is a ratio between the average observed brightness and the model

brightness computed for the unit asteroid–Sun distance. These parameters are not required for determination of other parameters. The usual choice of the phase function is the exponential-linear model (Kaasalainen et al. 2001; Muinonen et al. 2002):

$$f(\alpha) = a\ \exp\left(-\frac{\alpha}{d}\right) + k\alpha + 1 \tag{2.27}$$

where a and d are the amplitude and the scale of the opposition effect, respectively, and k corresponds to the overall slope of the phase function. The linear part is for a zero solar phase angle normalized to unity.

The scattering law we use has only four free parameters: c, a, d, k. During the inversion, we usually use a fixed value for c ($c = 0.1$).

In the case of relative lightcurves, the phase function is rather a former issue, it has a physical meaning for the absolute brightness, where it describes the real dependence of the asteroid brightness on the solar phase angle. The relative photometry looses this information, so fixed typical values for a, d and k are used. If we use calibrated sparse photometry in the inversion, computing the phase function parameters becomes quite easy: sparse data well define the phase function, which can be directly fitted. Originally, values of a, d and k were computed during the lightcurve inversion. However, from the physical point of view we should assure that the value of a is positive and the value of k negative. To do that, we modified the classical lightcurve inversion scheme and fit the exponential values of these parameters (i.e, $\exp(a)$, $\exp(d)$ and $\exp(k)$ similarly to Equation (2.9)). The phase function (2.27) is a usual, but not necessarily, choice.

Because this model of the scattering law is not based on the accurate physical nature of the scattering, the inversion gives only an empirical result that does not describe the physical surface properties. Nevertheless, for a successful inversion, it is often better to avoid the physical scattering laws. In order to describe the opposition effect by the phase function $f(\alpha)$, we need to have enough lightcurve observations for low phase angles.

2.3.7 Rotational state of asteroids

According to the rotation, single asteroids can be divided into two groups: (i) principal rotators, which rotational state can be described by the rotational period and the orientation of the spin axis, where majority of asteroids belongs, and (ii) objects in the excited rotational state (tumblers).

In the last case, we have multi-periodic lightcurves. Asteroid in a relaxed rotational state (principal rotator) rotates around its axis with a maximum momentum of inertia. Rotational state can be described by an orientation of the spin axis and the angular velocity ω. To describe the pole orientation, we use the ecliptic polar angle $\tilde{\beta}$ and the longitude λ with the convention: the angle $\tilde{\beta}$ is measured from the positive z-axis, lies in an interval $[0,\pi]$ and we consider the rotation around the polar axis positive ($\omega > 0$). The sense of rotation seen from the Earth is given by $\tilde{\beta}$, which is connected with the ecliptic latitude by the relation $\beta = 90\,^\circ - \tilde{\beta}$.

The first synodic period estimate can be usually determined from lightcurve observations during only a few days by finding a repeating pattern. Such data

can be processed by a Fourier analysis to gain a more accurate value. Sidereal rotational period is similar to the synodic period only if the orbital motion of the asteroid seen from the Earth is slow with respect to the rotational period. For multiple apparition data, the sidereal rotational period can be, for example, determined by the lightcurve inversion technique where we simultaneously solve the rotational state with the shape.

In the ecliptic astrocentric coordinate system we parametrize the pole orientation by the longitude λ (measured in the ecliptic plane from the vernal equinox) and latitude β (measured from the ecliptic plane). Let us define in this coordinate system a vector r_{ecl}, which has its origin inside the asteroid and points along the rotational axis to the surface. In the coordinate system fixed to the asteroid, we have a vector r_{ast} that can be derived from r_{ecl} by a transformation:

$$r_{\mathrm{ast}} = R_{\mathrm{z}}(\Phi_0 + \omega(t - t_0))\, R_{\mathrm{y}}(90\,^\circ - \beta)\, R_{\mathrm{z}}(\lambda)\, r_{\mathrm{ecl}}, \tag{2.28}$$

where $R_i(\lambda)$ is a rotational matrix describing the rotation around the axis i by an angle λ, for example:

$$R_{\mathrm{z}}(\lambda) = \begin{pmatrix} \cos\lambda & \sin\lambda & 0 \\ -\sin\lambda & \cos\lambda & 0 \\ 0 & 0 & 1 \end{pmatrix}. \tag{2.29}$$

Parameter t denotes time, both the angle Φ_0 and the epoch t_0 can be chosen freely.

According to the equation (2.28), the directions to the Earth and the Sun from the perspective of the asteroid are only functions of β, λ and ω. Because we know the positions of the Sun and the Earth in the astrocentric ecliptic coordinates (i.e., the geometry of observation), we can easily include parameters β, λ and ω (i.e., the pole orientation and the period) in the inversion process and optimize them.

By including the rotational parameters into the optimization process, we loose the uniqueness of the lightcurve inversion method. As a result, the parameter space is filled with a forest of local minims. In order to find the global minimum, we have to choose various initial pole orientations and periods and compute models for all of them. Each model is described by a χ^2-value, which corresponds to the quality of the fit (the lower the χ^2 is the better the model fits the observed data). We have to choose the initial poles and periods in the way that we compute models for all the local minims. The model with the lowest χ^2 belongs to the global minimum. The typical dependence of the χ^2 in the period space is shown in Figure 2.1. For each initial period, several pole orientations are tested (typically six or ten) and only the one with the lowest χ^2 is used for the model quantification.

If the photometric data cover several apparitions, the parameter space of periods is densely filled with local minims. The lowest distance between two local minims ΔP is described by the approximate relation:

$$\frac{\Delta P}{P} \approx \frac{1}{2}\,\frac{P}{T}, \tag{2.30}$$

where $T = \max(t - t_0)$ in the whole data set (time span of the observations). This relation is derived from the fact that by changing P by ΔP, the minims and maxims of the modeled lightcurve gain in time $t_0 \pm T$ a phase shift π. In the case

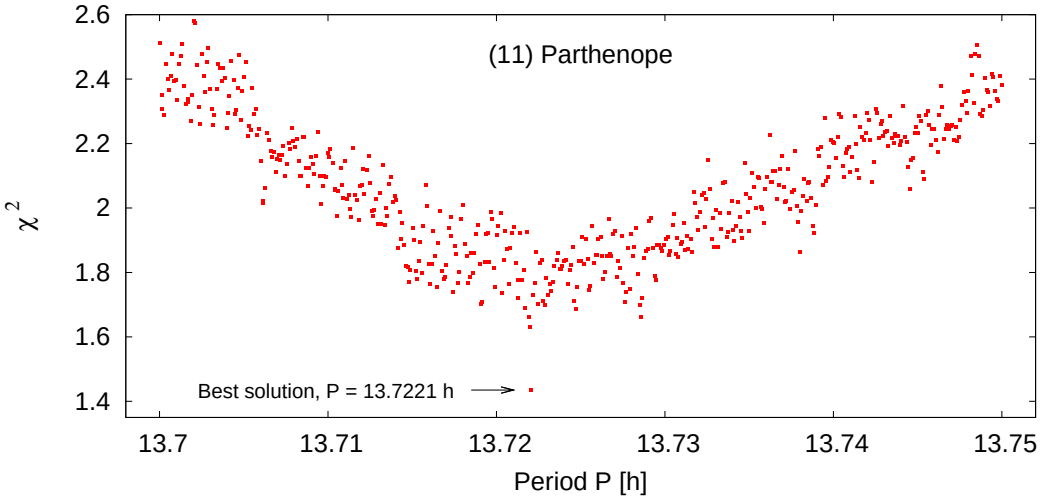

Figure 2.1: *Dependence of the quality of the fit (described by a χ^2) on the rotational period P for asteroid (11) Parthenope. For each period, several pole orientations were tested and only the one with the lowest χ^2 is plotted.*

of principal rotators, we can assume the typical double-sinusoidal pattern in the lightcurves, so the minims and maxims shift into the similar positions.

In practice, we test only period values close to the expected sidereal period, which can be determined from the single apparition lightcurves (e.g., by a Fourier analysis) or adopted from previous publications. A large database of asteroid rotational periods was presented by Warner et al. (2009) and is called Minor Planet Lightcurve Database[1]. For each asteroid, we scan an interval centered at the reported period value P with a range of $\pm 1\%$, $\pm 5\%$, and $\pm 20\%$ of P for reliability codes 3, 2+, and 2/2-, respectively. If we find a global minimum in the period that is significantly better than all other minims with different initial periods (the meaning of "significantly better" will be discussed later), we test then dozens of pole directions with a better shape resolution (i.e., more shape parameters) to find the best pole solution.

A straightforward method for determination of the pole and the period uncertainties does not exist. Former errors, such as square roots of the elements of the covariance matrix, are in practice irrelevant, this effect of random noise is contrary to the systematic and model uncertainties mostly negligible. According to Kaasalainen et al. (2001), even a high photometric noise was responsible in the numerical simulations for a maximal error lower than 2° in the pole orientation and only a few thousandths of the ΔP in P. The shape was affected minimally. Finding the real uncertainties is possible, e.g., by a set of optimizations for different scattering laws and initial parameter values. The dispersions of derived parameters correspond to the lower estimates of the errors. Another method for error estimation is based on a numerical simulation and is presented in Section 6.1.1. The typical pole uncertainty is $\sim 5 - 10^\circ$.

[1] `http://cfa-www.harvard.edu/iau/lists/LightcurveDat.html`, see this page for an explanation and more details about the reliability codes that quantify the quality of derived periods.

The period uncertainty is determined mainly by the time span of the photometric data. In the ideal case of a deep (significant) minimum near a period P in the $\chi^2(P)$-space, the error is $\sim 0.01\Delta P$. So, the period is accurate for data covering several decades of observations and vice versa. If we have insufficient data and therefore fail to find a deep minimum in the $\chi^2(P)$-space, the period P is uncertain. We usually have several possible period solutions in an interval with a width of several ΔP.

The method of Kaasalainen et al. (2001) uses all available photometric data from different apparitions to determine the sidereal rotational period. Additional parameters need to be included for tumbling asteroids (Kaasalainen 2001).

2.4 Practical approach, a unique solution

The lightcurve inversion scheme we use in this work was developed by Mikko Kaasalainen (Kaasalainen and Torppa 2001; Kaasalainen et al. 2001). The program `convexinv` was originally written in Fortran, but later was transformed into the C language by Josef Ďurech. The C version of the program together with a user guide is available on DAMIT. Recently, we modified the program in some minor aspects to better comply with our requirements (specific changes are discussed in Sections 2.4.1, 2.4.2 and 2.4.3). The program `convexinv` takes the observed lightcurves with the precomputed geometry of observations and, based on the initial choice of the rotational period and the pole orientation, finds the best set of solved parameters by a gradient-based optimization method. The solution corresponds to one local minimum in the parameter space and its "quality" is described by a χ^2-value. To investigate the whole space of free parameters, we have to run `convexinv` for all relevant initial parameter choices (of the rotational state) in a loop. In practice, we test periods from a particular interval (see Section 2.3.7) with a step of $0.5\Delta P$ (equation (2.30)). For each initial period, we test six (or ten) pole orientations isotropically distributed on a sphere. Only the best pole solution is used for the periodogram construction (see Figure 2.1), where we plot the dependence of the quality of the fit on the initial periods. If a unique period is found in the periodogram, we enlarge the shape resolution and we test for this period typically 48 pole orientations. If we have enough photometric data, we find a global minimum of the scanned parameter space that we call a *unique solution*.

A *unique solution* is defined as follows: (i) the best period has at least 10% lower χ^2 than all other periods in the scanned interval, (ii) for this period, there is only one pole solution with at least 10% lower χ^2 than the others (with a possible ambiguity for $\lambda \pm 180°$), and (iii) this solution fulfills our additional tests (see Section 4.1). The value of 10% was determined according to our experience rather than some exact relations, because of the typically unknown and various accuracy of individual lightcurves. Sometimes we understand under "unique solution" a solution that fulfills only (1) and (2), if we add (3), we can call the solution "reliable unique". What we mean by the unique solution should be clear from the context.

The ambiguity in the ecliptic longitude is caused by the symmetry of the inversion method and can be expressed as an ambiguity theorem, see Kaasalainen and Lamberg (2006) for its full definition and the proof. The theorem claims

that if we observe a body orbiting exactly in the ecliptic plane, it is not possible to distinguish between its two orientations, which correspond to rotation in the ecliptic longitude λ by 180 ° and to simultaneous reflection in the z-axis (reflection towards the xy-plane). The theorem applies for asteroids that orbit exactly in the equatorial plane, however, most asteroids have non-zero orbital inclinations. In practice, we usually get an ambiguous pole solution even for asteroids with inclinations over 20°. The reasons are observational errors, usually poor data coverage in the time, when the object is far from the ecliptic and systematic errors of the method.

2.4.1 Weights of the sparse lightcurves

Sparse data are usually of a worse quality than dense data by a factor of $\gtrsim 3$. If we use both data types in the lightcurve inversion as equal, the resulting model χ^2-values are significantly affected by the larger noise of the sparse data and, as a result, the unique solution can be lost in the forest of equally good solutions. In order to avoid this unwanted effect on the χ^2, we penalize the sparse data with respect to the dense data. We modified the lightcurve inversion scheme as follows: weights w_i of the individual lightcurves were introduced and the problem (2.10) was solved in the form:

$$\chi^2_{\mathrm{ren}} = \sum_i w_i \left\| \frac{\vec{L}^{(i)} - A^{(i)}\,\vec{g}}{\bar{L}^{(i)}} \right\|^2 . \tag{2.31}$$

Measure (2.31) turns into (2.10) if all weights w_i are unity. We use unity weights for the relative lightcurves and values lower than 0.5 for sparse data (weights of the sparse data from different astrometric sources are determined in Section 3). If we want to investigate particular asteroid more individually, it can be sometimes useful to use non-unity weights also for some dense lightcurves. Typically, we penalize the lightcurves with the worst photometric quality. We can even give zero weights to some lightcurves that will not be then used for the parameter optimization. However, contrary to removing such lightcurves from the data set, this approach allows us to still compare these observed lightcurves with the modeled ones (i.e., modeled lightcurves are computed also for lightcurves with zero weights). Of course, we can also favor some lightcurves by increasing their weights beyond unity.

2.4.2 χ^2-values of individual sparse lightcurves

Program `convexinv` gives the χ^2-value that corresponds to the whole data set, it is the sum over all data points in all lightcurves, see equation (2.10). This means that the rms, computed from the χ^2 by the equation:

$$\mathrm{rms} = \sqrt{\frac{\chi^2}{N}}, \tag{2.32}$$

where N is the number of data points and χ^2 can be computed by (2.10), (2.31) or (2.15), is also for the whole data set rather than for individual lightcurves. If we use weights for the sparse data, the χ^2-value is computed differently by (2.31).

Typically, weights of the sparse lightcurves are < 0.5, so the χ^2-value computed from equation (2.31 is lower than from (2.10). Thanks to that, the rms is also affected by the non-unity weights and is not then the real difference between the observational data and the model.

In order to gain the information about the χ^2-values and rms for only relative data and for each individual sparse lightcurve, we modified the program `convexinv`: the program can create a "rms" file with the values of the χ^2 and rms computed by Eqs. (2.10) and (2.32), i.e., all weights are 1, for: (i) all data, (ii) only relative data, and (iii) each individual sparse lightcurve.

2.4.3 Optimization of the convexity weight

As described in Section 2.3.2, the convexity condition (2.6) is computed after each iteration step of the lightcurve inversion is performed and the dark facet, which compensate the residuum in (2.6), is added. In the next step, the method tries to lower the residuum in (2.6) down. How quick the lowering should be and how big the residuum will be after the minimization depend on the convexity regularization parameter $c_{\rm conv}$. Typically, a value $\lesssim 1\%$ is acceptable for the dark facet. However, if the $c_{\rm conv}$ is low, high dark facet is usually produced. On the other hand, if $c_{\rm conv}$ is too high, the dark facet is very close to zero, and because the shape is forced too be convex "too much", we can get a worse fit (higher χ^2 than with a more convenient $c_{\rm conv}$). To find the optimal value for $c_{\rm conv}$, we run the `convexinv` first with a small $c_{\rm conv}$ for several initial periods and compute the average dark facet. If the average dark facet is close to one percent, we use this $c_{\rm conv}$ value for all initial periods. Otherwise, we enlarge the value of $c_{\rm conv}$ and repeat the procedure until we found a $c_{\rm conv}$ value that gives reasonable dark facets (i.e., close to 1%).

Chapter 3

Sparse data from AstDyS

Convex asteroid shape models can be derived from two different types of disk-integrated photometry: dense or sparse in time. Originally, only dense photometry was used. About 20 dense lightcurves from at least 4 or 5 apparitions are necessary for a unique shape determination. By this approach, $\sim$ 100 asteroid models were derived (e.g., Kaasalainen et al. 2002b, 2004; Torppa et al. 2003; Slivan et al. 2003; Michałowski et al. 2004, 2005, 2006; Ďurech et al. 2007; Warner et al. 2008a,b; Dunckel et al. 2009; Marciniak et al. 2007, 2008, 2009a,b, 2011). Deriving models from dense data is usually connected with gathering all available lightcurves that have been published and combining them with own observed data. This approach is rather expensive (demanding on fundings) and can produce only a limited number of new models (typically, $\sim$ 10 models are published annually). However, due to the limited amount and the poor quality of the currently available sparse data, using dense data in the shape modeling will stay important also in the future.

In order to significantly enlarge the number of asteroid models, sparse photometric data were studied and used in the LI: Ďurech et al. (2009) determined 24 asteroid models from a combination of dense data with sparse photometry from the USNO-Flagstaff station.

Sparse photometric measurements are produced by many astrometric surveys, but mostly as a by-product. In most cases, asteroid magnitudes are given to only one decimal place, i.e., the accuracy is 0.1 mag at best. In Section 1.2, we have shown that about a half of the asteroids have average lightcurve amplitudes greater than $\sim$0.25 mag and almost 20% of asteroids even greater than $\sim$0.5 mag. This means that, in principle, photometry with an accuracy of $\sim$0.1 mag carries sufficient information about rotational states and shapes for a significant number of asteroids and so its use in the lightcurve inversion for model determination is justified.

Our goal was to find out which astrometric observatories produce photometry suitable for lightcurve inversion and to use these data for determining new asteroid models. Through to September 2009 (the time of the data download), data for more than 350 000 objects from almost 1 500 observatories were archived on the AstDyS server (Asteroids, Dynamic Site[1]). Some of the observatories contributed with only a few data points, while others contributed with tens of thousands

[1] `http://hamilton.dm.unipi.it/`

of photometric measurements (e.g., large sky surveys such as the Catalina Sky Survey, LONEOS, or Siding Spring Survey).

The quality of the sparse photometry archived on the AstDyS varies significantly. We investigated the photometry carefully by establishing criteria for its quality. Then, using those criteria, we choose only those data that were useful for the inversion and determine their weights with respect to the dense data.

For each observatory, we extracted photometric data for the first 10 000 numbered asteroids if there were at least 30 data points in a single lightcurve. We transformed this photometry to the standard format used in lightcurve inversion: we computed geometry of observations (astrocentric ecliptic coordinates of the Sun and the Earth), corrected the epochs for the light-time, normalized the brightness to the distance of 1 AU from the Sun and the Earth, and excluded clear outliers.

For further investigation, we selected 13 observatories that fulfilled the condition of having data for more than ∼50 asteroids. This resulted in almost 30 000 sparse lightcurves for ∼9 000 asteroids. In the next step, we estimated mean uncertainties of individual observatories and, based on these uncertainties, we assigned relative weights to the data from each observatory. In this process, we assumed that the brightness vs. solar phase angle relation can be fitted for each sparse lightcurve with a simple relation:

$$f(\alpha) = \cos^2\left(\frac{\alpha}{2}\right)\left[a\,\exp\left(-\frac{\alpha}{b}\right) + c\,\alpha + d\right], \tag{3.1}$$

where α is the solar phase angle[2] and a, b, c and d are free parameters. Then, we constructed histograms of residuals (rms) for each observatory comparing actual data against the model given by Eq. (3.1). Histograms for all 13 studied observatories are plotted in Fig. 3.1. The dispersion is caused by observational uncertainties and by the amplitudes of the lightcurves. From these histograms, we estimated the "FWHM"[3] values and the most frequent residual (the mode); median values of the residual distributions for each location (Table 3.1) were computed. Observatories with a high median or "FWHM" value ($\gtrsim$0.2 mag for both) are not suitable for the lightcurve inversion (e.g. observatories 644, 691 or 704 in Fig. 3.1). Data from only seven observatories, listed in Table 3.1 with non-zero weights, had sufficient accuracy and so could be used for modeling. Based on the values of medians and"FWHMs", we estimated weights for the photometric data from each observatory relative to dense data, which have unity weight (see Table 3.1). We assumed that the typical accuracy of dense lightcurves is ∼0.02 mag.

The U.S. Naval Observatory in Flagstaff (USNO-Flagstaff station, IAU code 689) and the Hipparcos satellite are clearly the best observatories with respect to the photometric accuracy. Other observatories are less accurate but they still hold some information about rotational states and shapes of asteroids. For any given asteroid, we have typically 2–4 sparse lightcurves from different observatories covering the last ∼10–15 years.

[2]the Sun–asteroid–Earth angle

[3]the width of the distribution in the half of its maximum

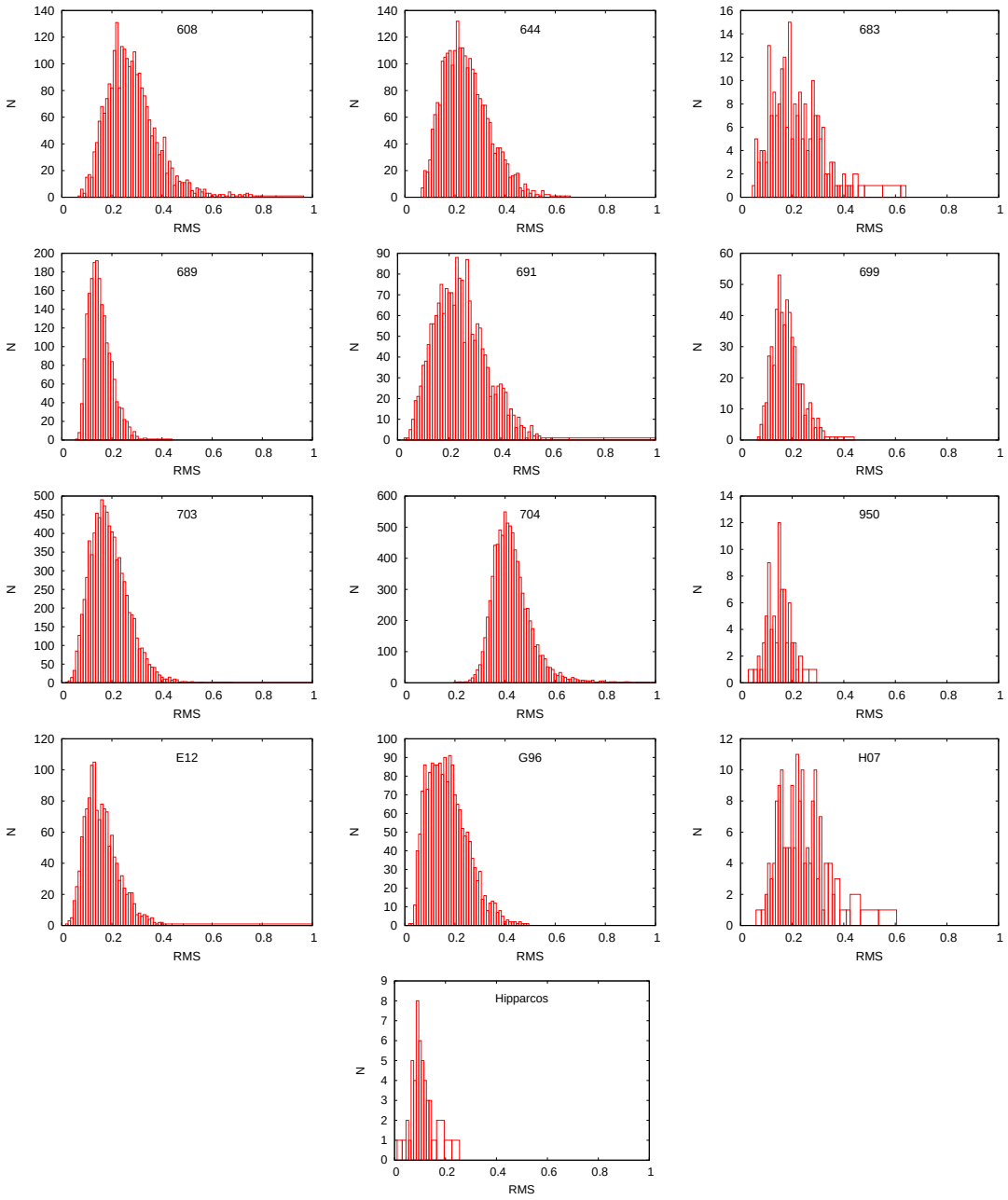

Figure 3.1: *Histograms of residuals comparing actual data against the model given by Eq (3.1) of all sparse lightcurves (with at least 30 data points) belonging to 13 studied observatories. Number of bins is* $\sim \sqrt{N}$*, where* N *is the total number of sparse lightcurves used for histogram construction.*

Table 3.1: *Comparison of estimated characteristics of residuals for 13 selected observatories: mode, "FWHM" and median. For each observatory, the table gives also the code designated by the International Astronomical Union, the number of sparse lightcurves $N_{\rm LC}$, the average number of data points for a single lightcurve $\bar{N}_{\rm P}$, the estimated weight of the sparse data with respect to the dense data (unity weight), and an official name of the observatory.*

Obs	$N_{\rm LC}$	Mode	FWHM	Median	$\bar{N}_{\rm P}$	Weight	Observatory name
608	2459	0.26	0.20	0.27	37	0	Haleakala-AMOS
644	2567	0.22	0.22	0.24	36	0	Palomar Mountain/NEAT
683	218	0.18	0.25	0.20	39	0	Goodricke-Pigott Observatory, Tucson
689	1970	0.14	0.12	0.15	118	0.3	U.S. Naval Observatory, Flagstaff
691	1893	0.23	0.22	0.24	39	0	Steward Observatory, Kitt Peak-Spacewatch
699	546	0.17	0.11	0.18	33	0.1	Lowell Observatory-LONEOS
703	8350	0.17	0.16	0.19	54	0.15	Catalina Sky Survey
704	8333	0.42	0.17	0.42	311	0	Lincoln Laboratory ETS, New Mexico
950	80	0.14	0.11	0.15	180	0.15	La Palma
E12	1354	0.14	0.16	0.15	41	0.1	Siding Spring Survey
G96	1810	0.14	0.22	0.17	43	0.1	Mt. Lemmon Survey
H07	161	0.20	0.18	0.23	47	0	7300 Observatory, Cloudcroft
Hip	49	0.10	0.10	0.11	53	0.3	Hipparcos satellite

Chapter 4

Reliability tests

In this chapter, we describe several reliability tests that we usually apply to derived models (Section 4.1). Some of the tests are performed independently on the type of the photometric data used for the model computation (general tests, Section 4.1.1). Other tests are intended to be used for models fully or partly based on sparse data (Section 4.1.2). The comparison between models derived only from low-quality sparse data (typically from the Catalina Sky Survey) and models based on dense data (previously published) allowed us to optimize the lightcurve inversion scheme and to eliminate false solutions (Section 4.2).

4.1 Tests of the models

Deriving a formally unique solution (according to our definition, see Section 2.4) for an asteroid does not necessarily mean that this model is correct. Due to the unknown systematic errors and photometric uncertainties, and the large variety in the photometric data, no consistent definition for the model uniqueness can be implemented. The definition we use is based on our long-term experience and numerical simulations and was optimized for different types of photometry (i.e., dense or sparse). Several circumstances can influence the solution, which could be then inaccurate or even incorrect. The most common case is the non-physicality of the shape, when the dimension along the rotational axis is overestimated due to the limited observing geometries. A false unique solution could be derived, e.g., if some of the lightcurves are affected by systematic errors or the photometry has a low signal/noise ratio (especially when we use only sparse data). In order to detect incorrect solutions, we introduced and performed several reliability tests. By using variety of reliability tests, there is always a chance that we reject also some good solutions. Although we loose a non-negligible amount of models by this, it is better to rather reject several correct models than miss even one false solution.

4.1.1 General tests

Let us first introduce a few simple tests that do not need to be described in a separate section. If we have dense lightcurves from one apparition that together cover the whole period cycle, the synodic rotational period can be easily deter-

mined. The synodic rotational period for a MBA has to be similar to the sidereal rotational period derived by the lightcurve inversion. We also visually check the shape appearance of the models and try to detect "weird" shapes.

Inertia tensor of the shape model

The lightcurve inversion method we use assumes that asteroids are in relaxed rotational states, which means that the derived models should rotate around the axis with a maximum momentum of inertia. For each derived shape, we computed principal moments of inertia (I_1, I_2, I_3) and a momentum of inertia along the spin axis I_z using equations presented by Dobrovolskis (1996) and checked if the rotation axis was close to the principal axis of the maximum momentum of inertia. Models for which the angle $\epsilon\,(I_z, I_{max})$ between the spin axis and the axis with a maximum momentum of inertia was larger than 30° or the ratio $\max\{I_1, I_2, I_3\}/I_z$ was larger than 1.1 indicated possible non-physical solutions. In Figure 4.1, an example of two shapes of asteroid (1111) Reinmuthia derived from a different amount of photometry is shown. The first model is too elongated along the z-axis ($\max\{I_1, I_2, I_3\}/I_z = 1.46$) and thus the shape is non-physical, the other one is physically correct, because of better coverage of observing geometries (based on 13 instead of 2 dense lightcurves, the amount of the sparse photometry was the same).

We always rejected models with the ratio $\max\{I_1, I_2, I_3\}/I_z$ larger than 1.1. However, the criterion $\epsilon\,(I_z, I_{max}) < 30°$ is too strict for elongated models with similar sizes along the rotational axis and the axis that is both perpendicular to the rotational axis and is the minimal size of the model. In this case, the principal moments for these two axes are similar, and even a small change in the dimension along the z-axis results in a large change of $\epsilon\,(I_z, I_{max})$. Under these circumstances, the angle between the spin axis and the axis with a maximum momentum of inertia can be large even for realistic shapes and so we allowed these models to pass this test.

The reason why we get non-physical models is usually the restricted geometry of observation. The model is then badly constrained in the dimension along the rotational axis. One way how to overcome the non-physicality of the model is to change the scale in the z-axis (i.e., the rotational axis) by multiplying the z-coordinates by a factor lower than one (e.g., 0.9). If the scaled model still fits the observed lightcurves well and is now physical, we have a unique solution. This approach is justified in cases when large amount of photometric data is available and so the period and the pole solution are well constrained.

It is common that we can find by the lightcurve inversion for an asteroid a unique period but we derive multiple pole solutions. In these cases we can construct models with all possible pole solutions and check their inertia tensors. Some of these solutions can be then rejected as non-physical. If only one solution (or mirror solution) remains, we have a unique model. By this approach, we derived almost a hundred new asteroid models (Section 5.1).

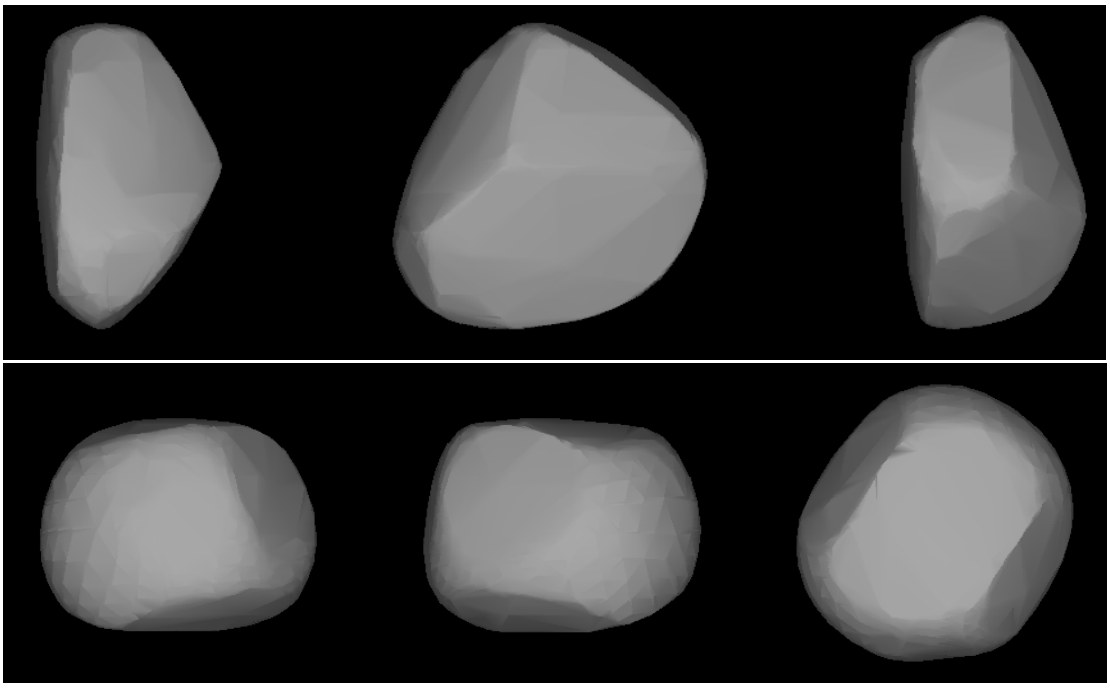

Figure 4.1: *Two shape models of asteroid (1111) Reinmuthia based on different number of lightcurves. The first shape model (*top panel*) corresponds to the solution with the pole (113°, 73°), which was derived from* 2 dense *lightcurves and 202 sparse data points. The second shape model (*bottom panel*) has a similar pole solution of (153°, 78°) but is based on* 13 dense *lightcurves and 202 sparse data points. In both panels, the first two figures are shown at equatorial view with rotational phases 90° apart, the third one is a pole-on view.*

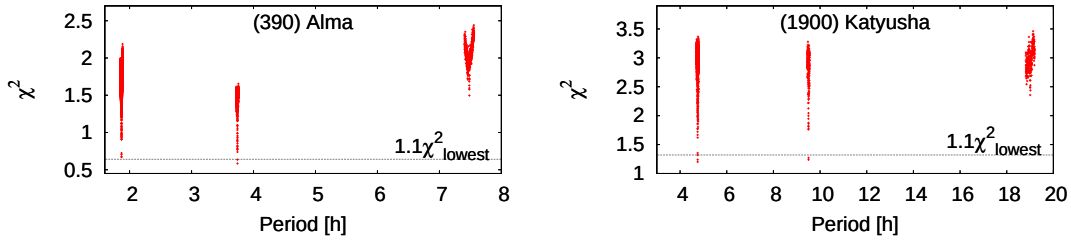

Figure 4.2: *Extended periodograms for asteroids (390) Alma (*left*) and (1900) Katyusha (*right*). For both of them, we tested intervals of periods near $P/2$, P and $2P$ values. The horizontal line represents the $1.1\chi^2$ value of the best solution near P (corresponds to our definition of a unique model).*

Half- and double-period models

In cases where we have only a few dense lightcurves for a given asteroid, it is easy to confuse the correct rotational period with its half or double value. If the a priori period value P in the Minor Planet Lightcurve Database is uncertain (corresponds to a low reliability code, see Section 2.3.7), it is necessary to check whether the half or the double period values do not give better fits. So, if the period was in doubt due to the low amount of dense lightcurves, we searched for a solution also around $2P$ and $P/2$. If we found a solution with chi-square lower than $1.1\chi^2$ of the solution with period P, we rejected the model as unreliable. In Figure 4.2 we plotted periodograms for asteroids (390) Alma and (900) Katyusha. While the model of asteroid (390) Alma with period P is significantly better (i.e., at least 10% difference between the χ^2 values) than its models with $2P$ and $P/2$, the model of asteroid (900) Katyusha for $P/2$ gives similar fit as the model for P, so the asteroids Katyusha fails to pass this test.

Lightcurve fit

Because we use dense lightcurves from individual observers or take them from several databases, we usually have to trust the data reduction of the observers. Unfortunately, several systematic errors in the lightcurves (e.g., inverse values of brightness, wrong information about the light-time correction, or clear outliers) can occur. The amount of adopted data is too high to be checked lightcurve by lightcurve. Some of the damaged lightcurves can be detected by visual check of their plots. An example of a wrong lightcurve in the data set for asteroid (574) Reginhild can be seen in Figure 4.3. If there are sufficiently many other lightcurves, the unique solution can be derived even with a few wrong dense lightcurves in the data set. Such lightcurves are then easily detectable by comparing modeled lightcurves with observed ones (Figure 4.4, where we show one clearly incorrect lightcurve that was present in the data set). However, even one corrupted lightcurve can usually spoil the determination of a unique solution. In such case, we have no model data for comparison, so the wrong lightcurve cannot be easily detected. This is a serious problem, because when there is a corrupted lightcurve presented in the data set, it can hide the solution even if we add new data. One way is to construct a model for the formally best solution, which is

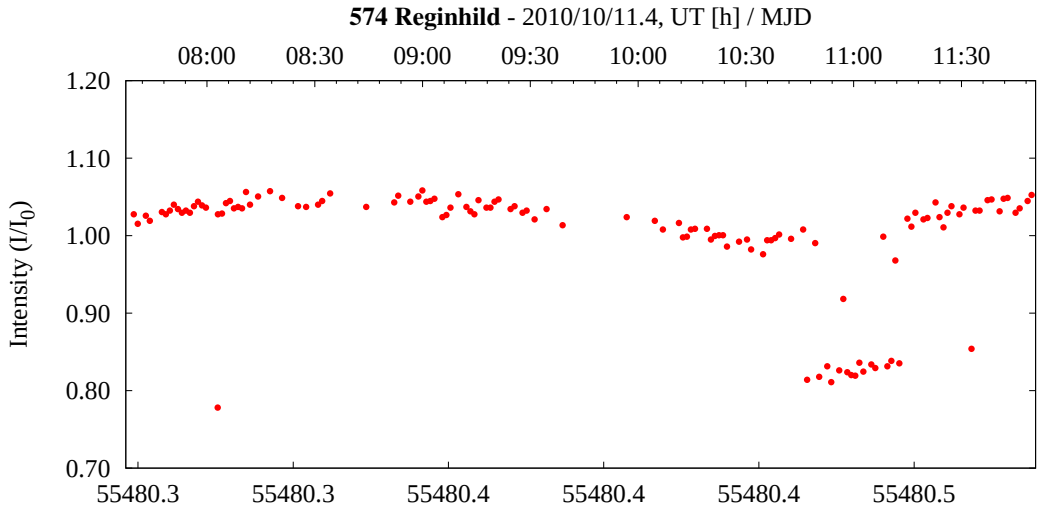

Figure 4.3: *Dense lightcurve of asteroid (574) Reginhild affected by systematic errors.*

not unique, and try to detect the wrong lightcurve by checking the lightcurve fit. This individual approach is legitimate for asteroids with many dense lightcurves from several apparitions when the unique solution is already expected.

4.1.2 Additional tests when sparse data are used

General tests described in the previous section are satisfactory for models fully based on dense data. For example, we usually have 20–30 dense lightcurves from at least three apparitions for such asteroids, so we can be quite confident with the solution. We have to perform additional tests when we use also sparse data in the modeling. These tests are intended to check mainly the stability of the solution on different types of sparse data modifications, e.g., we reduce the amount of sparse data points or we change the weights of the sparse data with respect to the dense data. False solutions are usually detected by all these additional tests. Additionally, it is relatively rare that the model do not pass these tests, because previous tests (general tests) are very efficient in false solution detection even if only a few dense lightcurves are available.

Reduction of the number of sparse photometric data

This test is performed only on models derived from sparse data. For each unique solution, we randomly reduce the original amount of observed sparse data points to 90% and use these new limited data sets again in the lightcurve inversion. Usually, in about 10% cases, we do not get any unique solution when using less data. These models are not necessarily wrong, but the amount of available data is probably just at the level when a unique solution can be derived. The important outcome from this test is, that for a given asteroid we did not find two different but formally correct solutions when using the full versus reduced data sets.

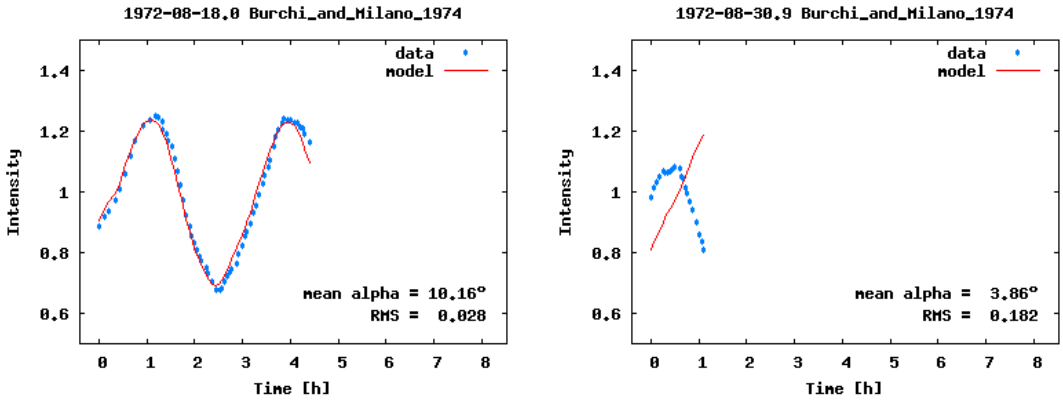

Figure 4.4: *Two dense lightcurves of asteroid (43) Ariadne observed by Burchi and Milano (1974) (blue) and corresponding lightcurves predicted by the shape model based on 45 dense and 2 sparse lightcurves (red). The observed lightcurve on the right panel is wrong (the other lightcurves in the data set are consistent with the model).*

Sparse data weights variation

We use fixed weights of the sparse data with respect to the dense data previously determined in Section 3. A correct and stable shape solution should not depend on the particular choice of sparse data weights (in reasonable borders) and should be derived also for different weight values. Let's assume, for example, a data set of ten dense lightcurves and one sparse lightcurve from USNO-Flagstaff station for an asteroid and that we were able to derive a unique solution for our fixed weight of the sparse data of 0.3. We consider this solution as stable if we derive same solutions also for weights 0.2 and 0.5. If we have for an asteroid sparse lightcurves from more sources, the possible weight combinations are numerous, so in praxis, we use only several reasonable combinations.

Models of "mock" objects

For asteroid shape models derived only from the sparse data, we create[1] a set of ten "mock" objects of roughly the same appearance and spin state (see an example of such shape in Fig. 4.5). For these synthetic objects, we compute their photometric data using same epochs and geometries and similar random noise level and use them in the lightcurve inversion method. The original model is reliable if we derive most of the models from the synthetic data of the "mock" objects. The dispersion of the periods and pole directions of the "mock" objects represent the typical uncertainties of these parameters. For all studied asteroids, we were able to derive unique models for most of their "mock" objects. In all cases when we did not get any unique solution for the "mock" object, the best fit corresponded to the correct solution although other solutions could not be ruled out. The typical uncertainty in the pole direction was $\pm 10°$. For the period, it

[1]We expanded the shape into spherical harmonic functions, we slightly and randomly modified the coefficients of the expansion (mainly higher order coefficients) and we computed the new shape.

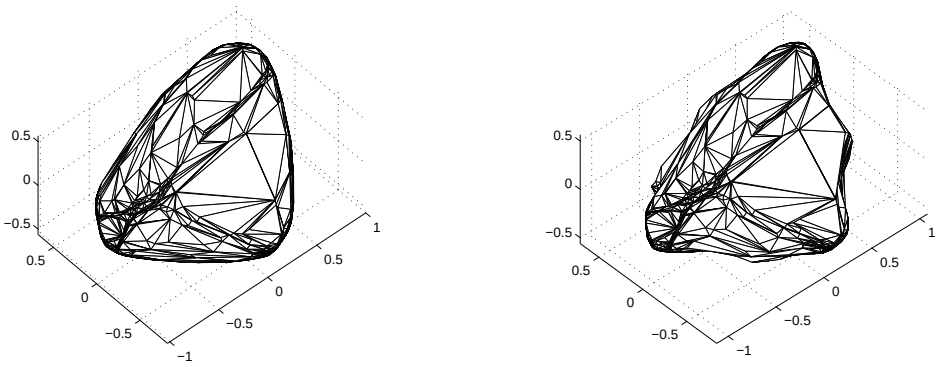

Figure 4.5: *Asteroid (810) Atossa: shape model (*left panel*) and an example of a "mock" shape model (*right panel*).*

was ~ 0.01 times the difference between the two local minims ΔP as determined by the period value and the time span of the data (see Equation (4.1)).

4.2 Reliability and stability of models based on sparse lightcurves

The stability of models derived from combined dense lightcurves and sparse data from USNO-Flagstaff station was already studied by Ďurech et al. (2009), where 24 new asteroid models based on such combined data were derived. In this section, we introduce several *reliability* and *stability* tests for models derived only from sparse data from different astrometric surveys.

Bootstrap

The bootstrap method is a powerful statistical technique that allows us to estimate the distribution of modeled parameters (see e.g., Press et al. 1986). Let's assume a set of N observational data points $D^{(0)}$. By using these data in the lightcurve inversion, we determine a solution $\mathbf{d}^{(0)}$ (set of parameters). The bootstrap method is based on generating a new data set $D^{(1)}$ by simply randomly drawing N data points from $D^{(0)}$. By doing this, we get a data set with a random fraction of original data points, about 37% ($\sim 1/e$) of them are duplicate. The new data set $D^{(1)}$ produce a solution $\mathbf{d}^{(1)}$. By repeating this procedure of generating synthetic data $D^{(I)}$ ($I = 1, 2, \ldots$) and computing corresponding solution $\mathbf{d}^{(I)}$, we get sets of simulated parameters $\mathbf{d}^{(1)}$, $\mathbf{d}^{(2)}$, ... that are distributed around $\mathbf{d}^{(0)}$ in close to the same way that $\mathbf{d}^{(0)}$ is distributed around the true solution. We applied this technique to data sets that consisted only from sparse data. An example of a realization of this test is as follows: For each successfully determined solution (from the actual observed data), we generate 10 synthetic data sets ($I = 1, \ldots, 10$) and try to derive the solution for each of them. The distribution of derived solutions, namely of rotational periods and spin directions describes the stability of the solution. The solution is stable, if (i) the dispersion in the rotational period

and the pole direction is $< \Delta P$ (see Equation (4.1) for explanation) and $\lesssim 30°$, respectively, and (ii) we derive unique solutions for the majority of data sets $D^{(I)}$.

Ellipsoid fitting

A simple way how to model shapes of asteroids is an approximation by a triaxial ellipsoid. This approach gives reasonable results for asteroids with shapes that are close to the rotational ellipsoids. For more complex shapes, this method usually fails to produce a unique solution or even gives an inaccurate parameter set. For example, for asteroids with rotational axes parallel to the ecliptic plane, the ellipsoidal models have the pole latitude systematically shifted about 20°, which causes the lack of asteroidal models with such rotational axes (see Marciniak et al. 2011).

The biggest advantages of this method are: (i) the shape is always physical, (ii) the low number of free parameters that needs to be optimized: two axes of the rotational ellipsoid (a/b, b/c, c=1), the rotational period and the pole orientation, and (iii) the projected area can be computed analytically (Ostro and Connelly 1984). The model computation of an asteroid with ~ 100 sparse data points is usually finished within few hours (we search the solution for periods of 2–100 hours). On the other hand, similar model computation by the lightcurve inversion takes several days. The disadvantages are the usual non-uniqueness of the solution and the previously mentioned systematic errors in the pole direction determination.

We use this method for two reasons: (i) for testing the reliability of the solution, and (ii) for saving computational time. After we derive a unique solution for an asteroid from the sparse data, we can quickly fit the data by a simple ellipsoidal model. The convex shape model is reliable, if the correct period is prominent also in the periodogram of the ellipsoidal model. An example of periodograms created by the lightcurve inversion and by the ellipsoidal modeling are plotted in Figure 4.6. The more general lightcurve inversion method gives for asteroid (16184) 2000 AD_{142} and its 97 observations from PS1 (the prototype single-mirror telescope of the Panoramic Survey Telescope & Rapid Response System, Pan-STARRS) several possible period solutions (i.e., with similar χ^2), some of them are well reproduced by the ellipsoidal model. Such nice fit by an ellipsoidal model is relatively rare when used on less accurate sparse data from the USNO-Flagstaff station or the Catalina Sky Survey or on an asteroid with a low lightcurve amplitude. Usually, a forest of similarly good minims (with χ^2 smaller than $1.1\chi^2$ of the lowest one) is present throughout the periodogram. In the case of asteroid (16184) 2000 AD_{142}, the lightcurve inversion do not give a unique solution, and thus more data are necessary. The ellipsoidal fit suggests the correct solution, but we use this simple method only for confirmations of unique solutions derived from the lightcurve inversion, not for excluding some solutions.

We investigated the possibility of using ellipsoidal fitting for reduction of the computational time consumed by the lightcurve inversion. The idea was that we first use an ellipsoidal model for the shape modeling and reduce the period interval of 2–100 hours according to the minims identified in the periodogram of the ellipsoidal fit. For each period minimum under a certain threshold, we took a period interval that corresponded in the frequency space to $\pm 1\%$ of $1/P$.

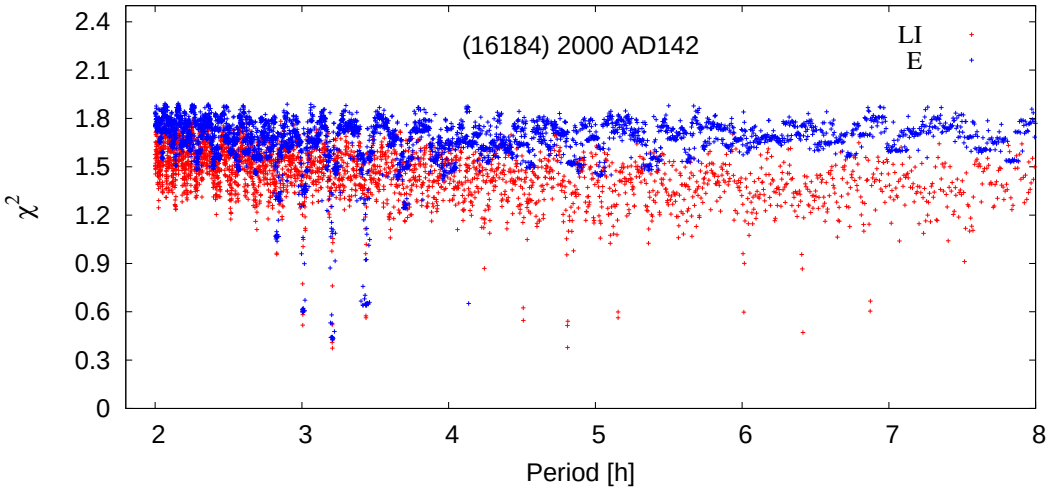

Figure 4.6: *Periodograms of asteroid (16184) 2000 AD_{142}. Result from the lightcurve inversion (*LI, red*) and from the fitting a simple ellipsoidal model (*E, blue*). The χ^2 for the ellipsoidal model is worse because fewer free parameters describing the model were used. Based on 97 sparse data points from Pan-STARRS project.*

Typically, we reduced the period interval to 10–30% of its full length (2–100 h). However, we were not able to find a relation for the threshold value that could be used for most asteroids. We also identified several cases when a correct period was not identified in the ellipsoidal periodogram and so the period was not present in the reduced period interval. These reasons led us to a decision of leaving this idea.

4.2.1 Models based fully on sparse data vs. DAMIT

Asteroid models derived from dense lightcurves represent the best opportunity how to test models based fully on sparse data. If we derive for the same asteroid two models based on different data sets, we can directly compare them (e.g., their rotational parameters). So far, about 100 asteroid models were derived purely from relative photometry and are stored in DAMIT database, from where we took their rotational parameters. For most of these asteroids, sparse data were also available. We used these sparse data in the lightcurve inversion for the model computation. In 13 cases, we were successful and derived independent models based on different photometric data sets than the adopted models (from DAMIT database). Rotational parameters of these two independent models for all 13 asteroids are listed in Table 4.1. We obtained similar models for 12 asteroids. The differences in rotational parameters are comparable with the uncertainties typically achievable by the lightcurve inversion (last decimal place in period values, 10–20° in pole directions). Model of asteroid (192) Nausikaa is different from the one published by Kaasalainen et al. (2002b). Their model based on 19 dense lightcurves gives the period $P = 13.62170$ h, our model purely from sparse data the period $P = 13.62515$ h. We tried to decide which model is correct by computing the model from all available photometric data (22 dense lightcurves and sparse

data from four observatories). We derived a unique model with $P = 13.62523$ h which is consistent with the model from the sparse data. We believe that the previous model is wrong because of inconsistencies in the processing of lightcurves from the apparition in 1965. Our model based on full data set is now included in DAMIT. This test shows the reliability of models based only on sparse data (we even detected a wrong solution previously published for (192) Nausikaa). For majority of these asteroids, sparse data are dominated by the USNO-Flagstaff station.

Table 4.1: *Comparison between rotational parameters of two different models of one asteroid derived (i) from dense lightcurves (taken from DAMIT database) and (ii) from sparse data (denoted D and S, respectively). For each asteroid, the table gives (i) the ecliptic coordinates λ_{S1} and β_{S1} of the pole solution with the lowest chi-square, the corresponding mirror solution λ_{S2} and β_{S2}, sidereal rotational period P_S, the number of sparse data points from astrometric surveys: N_{689}, N_{703} and N_{950} for the model based on sparse data, and (ii) the number of dense lightcurves N_{lc}, the ecliptic coordinates λ_{D1}, β_{D1}, λ_{D2} and β_{D2} and the sidereal rotational period P_D for the model from DAMIT based on relative data.*

Asteroid	N_{rel}	N_{689}	N_{703}	N_{950}	P_S [hours]	P_D [hours]	λ_{S1} [deg]	β_{S1} [deg]	λ_{D1} [deg]	β_{D1} [deg]	λ_{S2} [deg]	β_{S2} [deg]	λ_{D2} [deg]	β_{D2} [deg]
43 Ariadne	43	234	97		5.76197	5.76199	254	−14	253	−15	72	−12		
44 Nysa	72	271	63	218	6.42142	6.42142	104	47	99	58	298	54		
63 Ausonia	20	250	84	141	9.29759	9.29759	119	−23	120	−15	306	−31		
107 Camilla	29	332	68		4.84393	4.84393	73	46	73	54	246	63		
184 Dejopeja	17	196	76		6.44110	6.44111	198	63	200	52	13	61	18	54
192 Nausikaa*	19	320	67	127	13.62515	13.62170	337	−46	341	−50	142	−44		
283 Emma	24	148	96		6.89520	6.89522	85	26	85	37	260	12	251	22
382 Dodona	14	162	88		4.11324	4.11323	81	44	83	61	254	29	249	54
556 Phyllis	19	128	86		4.29262	4.29262	203	48	209	41	27	60	34	54
675 Ludmilla	38	205	68		7.71551	7.71549	26	60	49	74	193	45	196	49
984 Gretia	28	136	87		5.77804	5.77803	237	37	245	52	64	53		
1270 Datura	23	79	76		3.35810	3.35810	44	68	60	76	251	61	264	76
1620 Geographos	94	38	87		5.22331	5.22334	64	−46	58	−49				

* Our revised model based on 22 dense lightcurves and sparse data from the USNO-Flagstaff station, CSS, Carlsberg and Hipparcos satellite.

4.2.2 Models from the Catalina Sky Survey data

Most of the currently available photometric data were already used in the asteroid shape modeling. The only significant exception are data from the Catalina Sky Survey astrometric project (CSS for short, Larson et al. 2003). In this section, we investigate the possibility of determination of *reliable* asteroid shape models from only a small amount of sparse-in-time low-quality photometric measurements (~ 100) by the lightcurve inversion. Data from the CSS project are available for majority of known asteroids. Our motivation is to find out if these data are for asteroids with high lightcurve amplitudes of a sufficient amount and quality for a unique shape determination, and if so, how reliable these asteroid models are. The investigation of sparse data capabilities and the reliability of derived models is important, because (i) it can lead to a determination of new asteroid models without additional observational data, and (ii) in a few years, another huge amount of sparse data from three astrometric surveys will be available – from the Pan-STARRS (Panoramic Survey Telescope and Rapid Response System, Hodapp et al. 2004), and later also from the Gaia satellite (Perryman et al. 2001), and the LSST (Large Synoptic Survey Telescope, Ivezić et al. 2008). Understanding the CSS data with respect to the asteroid shape modeling will speed up future processing and use of the new sparse data.

Data from the Catalina Sky Survey project

The Catalina Sky Survey astrometric project has produced one of the largest amount of sparse photometric measurements. For most asteroids, no other data of sufficient quality are available (see the comparison of the sparse data amount for observatories USNO-Flagstaff station and the Catalina Sky Survey in Table 4.2). We used the CSS data in combination with other photometric data in Section 5.1, the typical photometric accuracy of the CSS data reached there $\sim 10-12\%$. Models from combined data were tested by tests described in Section 4.1.2. Although this accuracy of the CSS photometry seems very low, the data are valuable for asteroids with lightcurve amplitudes higher than $\gtrsim 0.25$ mag, which is about a half of all asteroids (we estimated that from the lightcurve data of the Minor Planet Lightcurve Database, Warner et al. 2009, , see Section 1.2). For an idea how significant the CSS data are, we estimated that for asteroids with numbers over ten thousand, there are dense data for ∼700 of them, on the other hand, we have at least 100 sparse data points from CSS for $\sim 6\,000$ of them.

Reliability of asteroid models derived only from the Catalina Sky Survey photometric data

Test 1: Previous models vs. models from the CSS data One way how to test the reliability of models based only on the CSS data is to compare them with models derived from different photometric data sets (similar to the test in Section 4.2.1). Here we used about a hundred of asteroid models from DAMIT derived from dense data (e.g., Kaasalainen et al. 2002a; Torppa et al. 2003; Slivan et al. 2003; Marciniak et al. 2007; Ďurech et al. 2007), and another ~ 100 models derived from combined dense and sparse data (Ďurech et al. 2009; Hanuš et al.

Table 4.2: *Number of sparse lightcurves n_{lc} with at least n_{p} sparse data points for observatories USNO-Flagstaff station and Catalina Sky Survey.*

n_{p}	n_{lc}	
	USNO	CSS
200	169	4
150	652	258
100	1276	7223
70	1658	24353
50	1837	45576
20	2159	85717
10	2574	95304

2011, listed in Table 5.1). These models are believed to be reliable and thus *correct*. For most of these ∼200 asteroids, CSS data are also available, so we tried to derive their independent models from only CSS data. We had at least 50 individual data points for 185 asteroids (out of ∼200). In 13 cases, we were able to derive a unique solution. For seven asteroids, the solution was in an agreement with the model based on an enlarged or completely different data set. Other six solutions were formally correct, but derived periods were different from the expected ones (see Table 4.3).

Table 4.3: *Comparison between rotational parameters of two different models of one asteroid derived (i) from dense or combined dense and sparse lightcurves (taken from DAMIT database) and (ii) from the CSS data (denoted D and C, respectively). For each asteroid, the table gives (i) ecliptic coordinates λ_{D1}, β_{D1}, λ_{D2} and β_{D2}, the sidereal rotational period P_D, the number of dense lightcurves N_{rel}, and the number of sparse data points from different observatories N_{689}, N_{703} and N_{950} for the model from DAMIT based on combined data, and (ii) the ecliptic coordinates λ_{C1} and β_{C1} of the pole solution with the lowest chi-square, the corresponding mirror solution λ_{C2} and β_{C2}, the sidereal rotational period P_C, and the number of the CSS sparse data points N_{CSS} for the model based on the CSS sparse data.*

Asteroid	N_{CSS}	N_{rel}	N_{689}	N_{703}	N_{950}	λ_{C1} [deg]	β_{C1} [deg]	λ_{D1} [deg]	β_{D1} [deg]	λ_{C2} [deg]	β_{C2} [deg]	λ_{D2} [deg]	β_{D2} [deg]	P_C [hours]	P_D [hours]	Correct?
52 Europa	86	39				233	50	251	35	49	49			8.8610	5.62996	✗
68 Leto	101	12	174	85	150	51	80	103	43	278	65	290	23	47.728	14.84547	✗
216 Kleopatra	52	55	276	52	93	82	19	72	21			237	38	4.36634	5.38528	✗
455 Bruchsalia	104		173	56		248	−62	231	−29			71	−31	17.8273	11.84002	✗
685 Hermia	152		93	148		52	71	197	87			29	79	50.387	50.387	✓
984 Gretia	115	28				229	54	245	52					6.57076	5.77803	✗
1022 Olympiada	111	3	107	91		48	27	39	17			241	67	3.83358	3.83359	✓
1382 Gerti	87	2	60	56		254	43	268	23	74	49	87	28	3.29338	3.08155	✗
1419 Danzig	102	1	135	87		11	56	22	76	160	62	193	62	8.1196	8.1196	✓
1568 Aisleen	93		82	37		141	−79	109	−68					6.6760	6.6760	✓
2156 Kate	62	4		44		45	71	49	74	247	54			5.62212	5.62215	✓
3678 Mongmanwai	139	2		103		130	−68	125	−65					4.18297	4.18297	✓
4483 Petofi	97	3		36		99	36	107	40					4.33301	4.33300	✓

Test 2: Periods from the MPLD vs. models from the CSS data Synodic rotational periods are known only for $\sim 3\,500$ asteroids (determined from dense lightcurves and stored in the Minor Planet Lightcurve Database). This a priori information is used in the shape modeling when we search for the model only near the assumed period (for example, we test the initial period values from an interval $(0.95\,P,\, 1.05\,P)$, where P is the published period value). Typically, we test a huge number of initial period values (∼thousands). The shorter the scanned period interval is, the less computational time we need. Another advantage of having a priori information about the period is that we gain a confidence on the model correctness if the derived period value is close to P. Unfortunately, for most asteroids, we do not know the period, so we have to search for the model on a period interval of all possible period values, typically 2–100 hours. This approach is extremely demanding on computational time and we loose the possibility of comparing the two period values.

In this test we used the a priori information about rotational periods. For some asteroids, we knew their periods, we had only CSS data (there exist their dense lightcurves, but we do not have them in an electronic form), and, based on that data, we were also able to derive their models near the published period. We extended the model search on the period interval of 2–100 hours and tried to find the model solutions again (as would be done if the period was unknown). This was performed for 11 asteroids. In seven cases, the previous solution derived on a shorter period interval was reproduced also on a larger period interval. For four asteroids, we did not get any unique period solution on the full period interval. In Fig. 4.7, we show a periodogram of asteroid (5647) 1990 TZ, where for each initial period a χ^2-value corresponding to the best shape model and the pole direction (a local minimum in the multi-dimensional parameter space) is plotted. This model computation was based on 87 individual measurements from the CSS, derived period $P = 6.13867$ h was in agreement with a period $P = 6.141$ h reported by Bembrick and Bolt (2003).

Test 3: Optimal number of shape parameters Since we derived several unique models that were clearly incorrect, we performed the next test to check more carefully the stability of the solution and to detect false solutions. The shape of an asteroid is parametrized by coefficients of its expansion into the spherical harmonic functions (see Section 2.3.3). The number of coefficients is given by the order n of the shape expansion we use, we call n the shape *resolution*. In the lightcurve inversion, we typically use $n = 6$, which corresponds to 49 coefficients ($(n+1)^2$). For asteroids with $\lesssim 100$ sparse data points from the CSS, so many coefficients could be to much and the LI could then lead to a random unstable solution that is even unique and physically correct. Another input parameter of the LI is the period step P_{step} between two subsequent periods from the scanned interval. The minimum difference between two local minims in the modeled parameter space of periods is given by

$$\Delta P \approx \frac{P^2}{2T}, \tag{4.1}$$

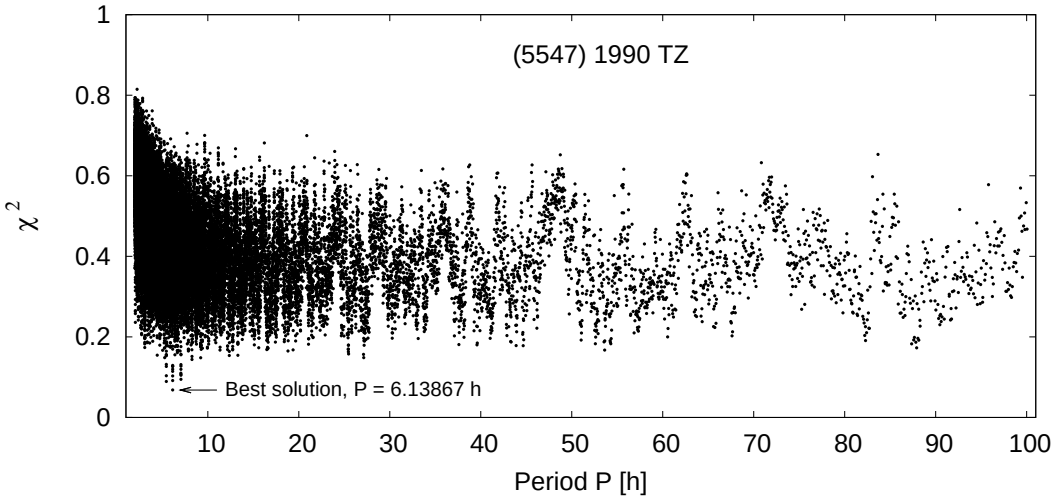

Figure 4.7: *Periodogram of asteroid (5647) 1990 TZ. Each point corresponds to a particular local minimum in the modeled parameter space of periods, pole directions and shapes.*

where P is the period value and T the timespan of the observational data. In our computations, we originally used for the period step a value $P_{\mathrm{step}} = 0.8\Delta P$.

We tested the stability of the solution using different values of the resolution n and two values of the period step P_{step} ($0.8\Delta P$ and $0.5\Delta P$). Table 4.4 summarizes the results of this test for all asteroids in *Test 1* where we derived unique solutions for $n = 6$ and $P_{\mathrm{step}} = 0.8\Delta P$ (corresponds to column 6). Correct unique solutions are marked by "✓", wrong unique solutions by "✗" and no unique solutions by "-".

In *Test 1*, where we compared derived models with corresponding models based on different data sets (stored in DAMIT), in seven cases out of 13, the solution was in a good agreement with the model based on a different and larger data set. From this point of view, the CSS data, which represent the largest data set of sparse photometry with photometric accuracy theoretically sufficient for a unique shape determination, seem to be promising for the asteroid shape modeling. Unfortunately, several clearly wrong models that fulfilled our conditions on a unique solution were derived (they had different sidereal rotational periods than was expected). Similar problem occurred in *Test 2*, where we compared the derived models with their previously known periods. One model was clearly incorrect.

There are several possible explanations why we derived incorrect models from the CSS data: (i) data for asteroids with low amplitudes are more noisy, (ii) low amount of data with respect to the number of modeled parameters, (iii) systematic errors of the survey. In cases (i) and (ii), the data are poor, contain not enough information about the period and shape, and could produce a random solution with an unrealistic rms value (the fit is "too perfect"). Oszkiewicz et al. (2011) have shown that photometric data sets from astrometric stations (such as the CSS) exhibit magnitude variations with apparent V-band magnitude. For the

Table 4.4: *Test of the stability of the model solution on the shape resolution n and the step in the period $P_{\rm step}$. The first column gives the asteroid number, symbol "✓" means that for a given n and $P_{\rm step}$, both unique and correct solution was derived, symbol "✗" means that a unique but wrong solution was derived, and finally, in the case if no unique solution was determined we use the symbol "-".*

	$P_{\rm step} = 0.8\Delta P$					$P_{\rm step} = 0.5\Delta P$				
Ast	n=2	n=3	n=4	n=5	n=6	n=2	n=3	n=4	n=5	n=6
685	✓	✓	-	✓	✓	✓	✓	-	-	✓
1022	✓	✓	-	-	✓	✓	✓	-	-	✓
1419	✓	✓	✓	✓	✓	✓	✓	✓	✓	✓
1568	✓	✓	✓	✓	✓	✓	✓	✓	✓	✓
2156	✓	✓	✓	✓	✓	✓	✓	✓	✓	✓
3678	-	-	✓	✓	✓	-	-	✓	-	✓
4483	✓	✓	✓	✓	✓	✓	✓	✓	✓	✓
52	-	-	✗	-	✗	-	-	✗	-	-
68	-	-	-	-	✗	-	-	-	-	✗
216	-	-	-	✗	✗	-	-	-	-	-
455	-	-	✗	✗	✗	-	-	✗	✗	✗
984	-	-	-	-	✗	-	-	-	✗	-
1382	-	-	-	-	✗	-	-	-	-	-

brightest asteroids, the images are saturated, and for the faintest, the background subtraction is imperfect. This consequence of (iii) is probably partially visible in our data – most of the incorrect models are brighter (have higher absolute magnitudes) than the correct ones. We are not able to distinguish between the effects of the amplitude and the noise from each other only from the sparse data without a model computation, so there is no way how to detect the case (i). The amount of data sufficient for a correct unique shape determination depends mainly on the geometry of observations and also on the signal-to-noise ratio, which is unknown. So, the sufficient amount of sparse measurements strongly varies from one asteroid to the other.

As seen in Table 4.4, models derived correctly for resolution $n = 6$ and period step $P_{\rm step} = 0.8\Delta P$ are mostly determined for other resolutions n and both period steps $P_{\rm step}$. No wrong solution appeared. In several cases, a unique solution was not found, but the correct period was still detected (we had multiple pole solutions). On the other hand, for incorrect models from *Test 1*, we got unique solutions for different resolutions n and period steps $P_{\rm step}$ only rarely and *never* for $n = 2$ or $n = 3$. All these unique solutions were always also incorrect. There is a weak dependence on the period step, $P_{\rm step} = 0.5\Delta P$ seems to be more convenient because when used, less incorrect models were derived. To minimize the determination of incorrect models that satisfy our requirement on unique solutions, we should use the values $n = 6$ and $P_{\rm step} = 0.5\Delta P$ for resolution and period step, respectively. If a unique solution is then determined, the computation should be

repeated with $n = 3$ and $P_{\text{step}} = 0.5\Delta P$. The model is reliable if we get similar unique solutions.

We repeated the computation for all eight successfully derived models from *Test 2* with $n = 3$ and $P_{\text{step}} = 0.5\Delta P$. Previously correct solutions were confirmed, the incorrect one was ruled out.

Our method assumes a single body in a relaxed rotation state (it rotates around the principal axis with the maximum momentum of inertia). Objects like tumblers or binary asteroids cannot be successfully modeled by convex inversion without including several additional parameters. The model determination of such objects usually fails because the single period model does not cover the more complex period features. The only exception are fully synchronous close binary systems with similar-sized components, such as (90) Antiope (Merline et al. 2000). These objects are reproduced as highly elongated single bodies, and because they have typically high amplitude lightcurves, they could be derived from low-quality sparse data such as CSS.

Sparse data from the Catalina Sky Survey are low efficient (we derived a unique solution in less than 1% cases) in unique model determination and seem more accurate for fainter asteroids. Incorrectly determined models could be indicated by unrealistic rms values, but not generally.

Correct period solutions for a single asteroid but different resolution n were always stable, the dispersion in the period was typically lower than ΔP (given by Eq. 4.1), which is for a period value of 10 hours and the timespan of the observations 10 years of the order of 10^{-3} h (typical values for the period and the timespan of the CSS data). The dispersion in the ecliptic latitude of the pole direction was usually $\lesssim 20°$, but in the ecliptic longitude of the pole direction often $\gtrsim 50°$. This significant dispersion in longitude was partially caused by models with high values of ecliptic latitudes (longitudes are more dense near the pole than near the equator) and because of the small *resolution* of the shapes.

Chapter 5

Models of asteroids

In this section, we list all asteroid models we derived. About a half of them were published in two papers in Astronomy and Astrophysics: Hanuš et al. (2011) and Hanuš et al. (2013, accepted for publication in A&A), the rest represent newly derived models, among which are 21 based fully on sparse data from the Catalina Sky Survey.

5.1 Asteroid models based on combined dense and sparse data

We used four main sources of dense photometric lightcurves: (i) the Uppsala Asteroid Photometric Catalogue (UAPC[1], Lagerkvist et al. 1987; Piironen et al. 2001), where lightcurves for about 1 000 asteroids are stored, (ii) data from a group of individual observers provided via the Minor Planet Center in the Asteroid Lightcurve Data Exchange Format (ALCDEF[2], Warner et al. 2009), (iii) data from another group of individual observers provided by Raoul Behrend, who maintains the Courbes de rotation d'astéroïdes et de comètes database (CdR[3]), and (iv) data from the Palomar Transient Factory survey (PTF[4], Rau et al. 2009). Polishook et al. (2012) recently analyzed a small fraction of PTF data and presented dense lightcurves for 624 asteroids. So far, only a fraction of photometric data from the PTF have been processed (four overlapping fields from four consecutive nights), which means that this source will become very important in the near future. We downloaded sparse data from the AstDyS site and gathered sparse lightcurves from seven astrometric surveys listed in Table 3.1 (with non-zero weights). For example, we got sparse data from the USNO-Flagstaff station (IAU code 689) for $\sim 2\,000$ asteroids, from the Roque de los Muchachos Observatory (La Palma, IAU code 950) for ~ 500 asteroids and $\gtrsim 100$ sparse data points from the Catalina Sky Survey Observatory (CSS for short, IAU code 703, Larson et al. 2003) for $\sim 7\,000$ asteroids.

We combined all the available relative data together with the sparse data.

[1] http://asteroid.astro.helsinki.fi/

[2] http://www.minorplanet.info/alcdef.html

[3] http://obswww.unige.ch/~behrend/page2cou.html

[4] http://www.astro.caltech.edu/ptf/

This gave us data sets with at least hundred measurements for ∼2 300 asteroids (in ∼900 cases, there were only sparse data available) to which we applied the lightcurve inversion method and, if a unique solution was determined, we used additional tests described in Section 4.1.2 to validate the solutions. We derived 282 new unique models, 58 of which are based only on sparse data. Basic characteristics of these models (photometric data properties, rotational states) are listed in Table 5.1. Based on previous results with limited data sets, we estimated the uncertainty in the pole direction as ±10–20°. As we expected, the uncertainty seemed dependent on the number of dense and sparse photometric data. These uncertainties in the pole directions are discussed also in Sections 2.3.7 and 6.1.1. The uncertainty of the rotational period depends on the time interval covered by the observational data and is of the order of the last decimal place of period values P in Table 5.1.

For some asteroids, we were able to determine a unique rotational period, but we had multiple pole solutions with similar ecliptic latitudes β. We computed models with all pole solutions and checked their physicality (we computed inertia tensors). Four different scenarios occurred: (i) only one or two models were correct, and in the case of two, we had a mirror solution (difference of ∼180° in the longitude), (ii) two models were correct, but it was not a mirror solution, (iii) three or four models were correct, and (iv) all models were not physical. If the solution from (i) successfully passed general tests, we got a new unique model which is then listed in Table 5.1. In (ii) and (iii), the models gave us accurate period values and in some cases also rough estimates of ecliptic latitudes β (if the biggest difference in latitudes of the models was $< 50°$), which are also important parameters. We call these models *partial models* and present results for 105 of them in Table 5.2. For the ecliptic latitude β, we used the mean value of all different models. We defined parameter $\Delta = |\beta_{\max} - \beta_{\min}|/2$ as being the estimated uncertainty of β, where $\beta_{\max}$ and $\beta_{\min}$ are the extremal values within all β. The threshold for partial models was $\Delta < 25°$.

In Hanuš et al. (2011), we presented 80 unique and 30 partial models. By using additional data in the modeling, we later derived for 16 out of these 30 partial models their unique models (also listed in Table 5.1). In Table 5.2, we list within the 105 partial models also the 14 remaining partial models published in Hanuš et al. (2011). In Hanuš et al. (2013), we published 119 unique models from combined data.

The motivation of constructing partial models was to enlarge the number of models for the parameter analysis (especially for the spin-axis direction study, see Section 6.1.2). All new unique shape models are/will be now included in DAMIT.

Table 5.1: *List of new asteroid models derived from combined data sets or sparse data alone. For each asteroid, the table gives also the number of dense lightcurves $N_{\rm lc}$ observed during $N_{\rm app}$ apparitions and the number of sparse data points for the corresponding observatory: N_{689}, N_{699}, N_{703}, $N_{\rm E12}$, $N_{\rm G96}$, N_{950} and $N_{\rm Hip}$. The uncertainty of the rotational period is of the order of the last decimal place of period values P, and of the pole direction $5-10^\circ/\cos\beta$ in λ and $10^\circ-20^\circ$ in β. Pole solutions preferred by asteroid occultation measurements (Ďurech et al. 2011) are emphasized by a bold font.*

Asteroid	λ_1 [deg]	β_1 [deg]	λ_2 [deg]	β_2 [deg]	P [hours]	$N_{\rm lc}$	$N_{\rm app}$	N_{689}	N_{699}	N_{703}	$N_{\rm E12}$	$N_{\rm G96}$	N_{950}	$N_{\rm Hip}$
10 Hygiea	312	−42	**122**	**−44**	27.6591	23	9	263					405	50
11 Parthenope	311	14	128	14	13.72205	107	13	297		24			147	66
13 Egeria	44	21	238	11	7.04667	13	4	255		74			203	34
14 Irene	97	−22	268	−24	15.02991	20	8	250			48		161	45
25 Phocaea	347	10			9.93540	22	5	272		100				
37 Fides	270	19	89	27	7.33253	23	5	270		61			135	31
40 Harmonia	22	31	206	39	8.90848	19	6	210		48			255	102
42 Isis	106	40	302	28	13.58364	28	7	210		36			128	51
60 Echo	270	−9	90	−19	25.2286	32	5	277		120				
62 Erato	87	22	269	23	9.21819	1	1	164		48				
68 Leto	103	43	290	23	14.84547	12	2	174		85	30		152	
69 Hesperia	250	17	71	−2	5.65534	35	7	222		44	40			
72 Feronia	287	−39	102	−55	8.09068	20	5	196		124			127	
79 Eurynome	228	30	54	24	5.97772	36	4	240		168				
97 Klotho	−1	30	161	40	35.2510	25	6	309		31			202	
119 Althaea	339	−67	181	−61	11.46514	4	2	149		59			222	
147 Protogeneia	269	15	90	14	7.85232	11	3	152		80				
149 Medusa	333	−73	156	−76	26.0454	13	4	134		60				
157 Dejanira	319	−64	146	−33	15.8287	14	2	94		123				
162 Laurentia	139	64	313	51	11.86917	4	2	166	31	40				
163 Erigone	194	−72	47	−64	16.1403	3	1	177		104				
166 Rhodope	345	−22	173	−3	4.714793	7	2	141		111				
174 Phaedra	94	36	266	14	5.75025	2	1	173		36				
178 Belisana	260	20	79	9	12.32139	35	3	147		127				
183 Istria	85	20			11.76897	8	2	142		174				
188 Menippe	32	48	198	25	11.9765	4	1	145		40				
191 Kolga	173	−64	310	−60	27.8346	5	1	178		116				
193 Ambrosia	141	−11	328	−17	6.58166	18	4	169		87				
199 Byblis	344	−24	165	9	5.22063	22	5	184		108				
220 Stephania	26	−50	223	−62	18.2087	9	2	117		99				
222 Lucia	106	50	293	49	7.83671	9	4	160		100				
239 Adrastea	205	−75	332	−66	18.4716			112		89				

Table 5.1: *continued.*

Asteroid	λ_1 [deg]	β_1 [deg]	λ_2 [deg]	β_2 [deg]	P [hours]	N_{lc}	N_{app}	N_{689}	N_{699}	N_{703}	N_{E12}	N_{G96}	N_{950}	N_{Hip}
242 Kriemhild	100	−40	285	−15	4.545174	25	7	179		144				
257 Silesia	5	−53	176	−46	15.7097	18	2	167		88				
258 Tyche	224	−4	40	−9	10.04008	10	2	162		44				
260 Huberta	23	−28	206	−19	8.29055	6	2	162		90				
264 Libussa	157	18	338	−9	9.22794	19	3	129		39	49			
265 Anna	109	−53			11.6903			114		79				
271 Penthesilea	225	49	41	55	18.7875	7	1	129		83				
272 Antonia	293	−90			3.85480	7	2	109		92				
274 Philagoria	74	−79	239	−66	17.9408	6	1	145		76				
281 Lucretia	128	−49	309	−61	4.349711	8	4	129		83				
290 Bruna	286	−80	37	−74	13.8055	9	1	97		66				
291 Alice	69	51	249	56	4.316011	9	4	75		46				
297 Caecilia	223	−53	47	−33	4.151388	15	5	149		130				
302 Clarissa	**28**	**−72**	190	−72	14.47670	8	2	102		104				
310 Margarita	225	−35	42	−33	12.0710	27	1	88	31	51				
312 Pierretta	82	−39	256	−58	10.20764	4	1	176		36	52			
313 Chaldaea	210	33	43	10	8.38992	9	3	186		92				
317 Roxane	315	−64			8.16960	10	1	163		133				
319 Leona	94	22	184	−18	635.9	21	2	147		88				
336 Lacadiera	194	39	37	54	13.69552	3	1	121		36	32			
340 Eduarda	188	−43	18	−47	8.00613	2	1	117		76	31	36		
345 Tercidina	346	−55			12.37082	42	8	161		155				
351 Yrsa	20	−70	193	−41	13.3120	2	1	183		52				
352 Gisela	24	−21	206	−28	7.48008	6	4	134		140				
353 Ruperto-Carola	183	−56	108	−53	2.738964	6	1	106		80				
354 Eleonora	144	54			4.277186	37	9	258		40			139	96
355 Gabriella	341	78	197	70	4.82899	4	1	128						
361 Bononia	295	12	116	44	13.80634	5	2	183		73				
364 Isara	172	58	354	47	9.15748	4	1	98		104				
367 Amicitia	203	38	21	32	5.05502	2	1	128		34				
371 Bohemia	93	49	256	43	10.73965	30	4	181		79				
372 Palma	221	−47	44	17	8.58189	28	6	214		52	36			
376 Geometria	239	45	63	53	7.71097	39	9	158		76				
390 Alma	53	−50	275	−76	3.74117	5	2	142		58				
399 Persephone	36	63			9.14639			166		36				
400 Ducrosa	328	56	158	62	6.86788	3	1	103						
403 Cyane	65	35	230	33	12.2700	7	3	186		104				
404 Arsinoe	25	57			8.88766	49	9	199		104				
406 Erna	357	−49	161	−60	8.79079	8	1	134		93				

Table 5.1: *continued.*

Asteroid	λ_1 [deg]	β_1 [deg]	λ_2 [deg]	β_2 [deg]	P [hours]	N_{lc}	N_{app}	N_{689}	N_{699}	N_{703}	N_{E12}	N_{G96}	N_{950}	N_{Hip}
413 Edburga	202	−45			15.7715	2	1	148		43				
436 Patricia	124	−30	339	−58	16.1320	4	1	97		53	91			
440 Theodora	80	−88			4.83658			123		103		48		
441 Bathilde	285	55	122	43	10.44313	32	7	158		112				
443 Photographica	349	−67			19.7975	13	2	147		110				
446 Aeternitas	150	82	317	51	15.7374			144		118				
471 Papagena	**223**	**67**	22	18	7.11539	13	2	293		72			203	112
486 Cremona	227	59	31	30	65.151	1	1	127		55	35			
499 Venusia	37	50	212	46	13.4871	4	1	122		39		31		
503 Evelyn	166	−65	264	−63	38.778			190		68				
507 Laodica	102	−55	312	−49	4.70657			162		103				
509 Iolanda	245	65	98	38	12.2907	1	1	178		85				
512 Taurinensis	324	45			5.58203	11	2	124		111				
519 Sylvania	106	9	286	−13	17.9647	5	2	147		76				
531 Zerlina	78	−84			16.7073	28	3	48		52				
537 Pauly	31	26	214	51	16.2961	7	3	157		124				
540 Rosamunde	302	80	126	62	9.34779	3	1	135		83				
543 Charlotte	333	59	172	49	10.7184	4	1	138		98				
544 Jetta	275	−84	31	−67	7.74528	3	1	139		60				
550 Senta	63	−40	257	−57	20.5726	9	1	151		85				
553 Kundry	289	55	198	71	12.6025	5	1	61		80				
565 Marbachia	348	−26	184	−48	4.58782	4	1	162		130				
567 Eleutheria	321	31	136	59	7.71742	14	2	128		116				
572 Rebekka	1	54	158	39	5.65009	5	2	155		63				
573 Recha	74	−24	252	−48	7.16586	3	1	161		85				
578 Happelia	338	63			10.06447	11	3	183		80				
584 Semiramis	106	−56	315	−32	5.06893	24	6	150		59	49			
590 Tomyris	273	−47	120	−46	5.55248	3	1	91		32				
600 Musa	0	−74	208	−46	5.88638	23	7	96		132				
601 Nerthus	173	44	20	32	13.5899			139		94				
606 Brangane	183	20	354	26	12.29067	2	1	108		70				
607 Jenny	217	−43	32	−21	8.52234	7	2	166		101				
621 Werdandi	140	−62	247	−86	11.77456	12	2	146		71				
629 Bernardina	40	33	236	48	3.76360			91		48				
631 Philippina	183	−2			5.90220	6	2	171		38				
669 Kypria	31	40	189	49	14.2789	5	1	142		126				
679 Pax	218	38	36	−27	8.45602	5	2	189		148				
685 Hermia	197	87	29	79	50.387			93		148				
695 Bella	87	−55	314	−56	14.21900	8	1	184		90	30			

Table 5.1: *continued.*

	Asteroid	λ_1 [deg]	β_1 [deg]	λ_2 [deg]	β_2 [deg]	P [hours]	$N_{\rm lc}$	$N_{\rm app}$	N_{689}	N_{699}	N_{703}	$N_{\rm E12}$	$N_{\rm G96}$	N_{950}	$N_{\rm Hip}$
698	Ernestina	215	−62	75	−51	5.03660			140		76				
708	Raphaela	37	27	217	22	20.8894	5	1	140		95				
725	Amanda	145	−63	320	−70	3.74311	18	7	70		77				
731	Sorga	83	40	275	21	8.18633	7	2	131		136				
732	Tjilaki	160	23	353	24	12.3411	3	1	140		153				
733	Mocia	305	54	191	49	11.37610	2	1	175		52				
753	Tiflis	5	36	199	57	9.8259			129		64				
762	Pulcova	22	−12	198	−45	5.83977	5	1	195		93				
784	Pickeringia	285	44	109	76	13.1700	1	1	193		83				
787	Moskva	331	59	126	27	6.05581	15	4	160		92				
792	Metcalfia	88	−14	274	−13	9.17821	9	3	164		56				
800	Kressmannia	345	37	172	34	4.460963	8	2	108		51				
803	Picka	218	34	53	41	5.07478			154		50				
807	Ceraskia	325	23	132	26	7.37390	2	1	132		111				
808	Merxia	26	54	192	57	30.630	4	1	158		87		32		
810	Atossa	12	67	188	69	4.38547			99		71		60		
812	Adele	301	44	154	69	5.85746			65		119				
816	Juliana	124	−8	304	10	10.5627	11	2	158		107				
819	Barnardiana	169	46	334	47	66.698			121		86				
822	Lalage	90	−54	271	−54	3.346506	4	2	124		94				
825	Tanina	46	48	231	60	6.93981	2	1	114		40				
832	Karin	242	46	59	44	18.3512	13	3	84			39			
847	Agnia	341	18	162	13	14.8247	3	1	136						
852	Wladilena	181	−48	46	−53	4.613301	30	8	138		101				
856	Backlunda	40	44	323	44	12.02894	2	1	155		103				
857	Glasenappia	227	48	38	34	8.20757	4	2	140		116				
867	Kovacia	200	−44	38	−50	8.67807			78		76				
874	Rotraut	201	−41	2	−36	14.3007	3	1	129		68				
875	Nymphe	42	31	196	42	12.6213	6	1	94		100				
881	Athene	102	−72	334	−39	13.8942			92		89				
889	Erynia	187	−60	335	−74	9.8749			94		65				
900	Rosalinde	276	70	90	39	16.6868	3	2	125		170				
920	Rogeria	238	−15	47	−35	12.5749			137		79				
925	Alphonsina	**296**	**41**	147	22	7.87754	4	1	134		48	79			
934	Thuringia	120	−52			8.16534			123		59				
936	Kunigunde	47	57	234	49	8.82653			154		88				
958	Asplinda	41	48	226	35	25.3050	2	1	98		68				
966	Muschi	125	−40	282	−71	5.35529	3	1	139		96				
986	Amelia	88	28	288	25	9.51857	4	1	147		110				

Table 5.1: *continued.*

	Asteroid	λ_1 [deg]	β_1 [deg]	λ_2 [deg]	β_2 [deg]	P [hours]	N_{lc}	N_{app}	N_{689}	N_{699}	N_{703}	N_{E12}	N_{G96}	N_{950}	N_{Hip}
994	Otthild	183	−50	41	-39	5.94819	26	5	140		125				
1002	Olbersia	220	35	16	54	10.2367			87		48	54			
1010	Marlene	302	42	114	57	31.0651	8	1	119		64				
1017	Jacqueline	364	68	115	85	7.87148			144		140				
1040	Klumpkea	172	48			56.588			114		88				
1056	Azalea	252	51	64	41	15.0276	3	1	122		112				
1087	Arabis	334	−7	155	12	5.79501	3	1	156		92				
1089	Tama	193	32	9	28	16.4461	90	7	108		79				
1102	Pepita	25	−34	231	−30	5.10532			147		47				
1111	Reinmuthia	356	68	153	78	4.007347	13	3	137		65				
1126	Otero	44	75	240	56	3.64800	2	1	101		110				
1130	Skuld	24	36	200	35	4.80764	14	1	92		106				
1140	Crimea	12	−73	175	−22	9.7869	3	1	96		116				
1148	Rarahu	148	−9	322	−9	6.54449			95		64				
1175	Margo	184	−41	−6	−10	6.01375	4	1	164		92				
1182	Ilona	67	−77			29.8755			117		104				
1188	Gothlandia	334	−84			3.491820	36	5	134		91				
1207	Ostenia	310	−77	124	−51	9.07129	2	2	87		71				
1241	Dysona	125	−68			8.60738	7	1	156		64				
1249	Rutherfordia	32	74	197	65	18.2183	6	2	187		75				
1255	Schilowa	156	−4	338	15	29.4674			143		106				
1286	Banachiewicza	131	35	311	51	8.63042			81		51				
1291	Phryne	106	35	277	59	5.58414	2	1	129		72				
1301	Yvonne	39	41			7.31968			78		56	33			
1307	Cimmeria	345	51	240	71	2.820724	2	1	91		54				
1317	Silvretta	45	−57	161	−46	7.06797	13	3	120		69				
1333	Cevenola	38	−86	220	−44	4.87932	3	1	104		91				
1353	Maartje	130	34	270	74	22.9927			154		139				
1366	Piccolo	352	49	202	52	16.1834	9	3	136		110				
1368	Numidia	62	−38	203	−60	3.640738	3	1	129		83				
1378	Leonce	304	−59	134	−57	4.32527			89		113				
1379	Lomonosowa	263	−52			24.4844	14	2	132		124				
1382	Gerti	268	23	87	28	3.081545	2	1	60		56		52		
1386	Storeria	227	−67	297	−67	8.67795	10	1	33		78				
1389	Onnie	183	−75		−79	23.0447	2	1	90		97				
1393	Sofala	319	28	134	41	16.5931			69		91				
1401	Lavonne	204	23	27	44	3.93261	3	1	109		88				
1419	Danzig	22	76	193	62	8.11957	1	1	135		87				
1423	Jose	159	−59			12.3127			121		134				

Table 5.1: *continued.*

Asteroid	λ_1 [deg]	β_1 [deg]	λ_2 [deg]	β_2 [deg]	P [hours]	N_{lc}	N_{app}	N_{689}	N_{699}	N_{703}	N_{E12}	N_{G96}	N_{950}	N_{Hip}
1432 Ethiopia	41	44	225	54	9.84425	11	1	88		101				
1436 Salonta	223	18	57	35	8.86985	10	2	132		90				
1446 Sillanpaa	123	82	221	68	9.65855	2	1	76		73				
1450 Raimonda	231	−56	71	−60	12.6344			74		116				
1459 Magnya	72	−60	203	−52	4.67911			137		96				
1464 Armisticia	195	−52	38	−69	7.46699	2	1	231		67				
1472 Muonio	249	61	42	62	8.70543	6	1	99		93				
1482 Sebastiana	262	−68	91	−67	10.48965	2	1	131		39	30			
1490 Limpopo	319	22	142	2	6.65164	5	1	103		107				
1495 Helsinki	355	−39			5.33131	13	2	62		109				
1503 Kuopio	172	−80			9.9586			116		68				
1514 Ricouxa	251	75	68	69	10.42468	3	1	68		56				
1518 Rovaniemi	62	60	265	45	5.25047	2	1	100		73				
1528 Conrada	250	−51	93	−66	6.32154	2	1	93		126				
1546 Izsak	124	35	327	62	7.33200	3	1	80		80				
1554 Yugoslavia	281	−34	78	−64	3.88766	3	1	75		75				
1559 Kustaanheimo	275	29	94	33	4.30435			53		82				
1568 Aisleen	109	−68			6.67597			82		37				
1572 Posnania	205	−82	85	−63	8.04945	46	7	141		83				
1607 Mavis	0	59	222	70	6.14775	4	1	141		179				
1630 Milet	304	34	121	40	32.485	3	1	72		92				
1633 Chimay	321	78	36	53	6.59064	2	1	127		83				
1634 Ndola	261	45	66	34	64.255	7	1	71		110				
1635 Bohrmann	5	−38	185	−36	5.86427	8	1	108		47				
1648 Shajna	227	58	46	47	6.41368			75		136				
1659 Punkaharju	259	−71	75	−22	5.01327	2	1	118		66				
1665 Gaby	207	64	17	34	67.905	1	1	81		119				
1672 Gezelle	243	64	64	67	40.6825	12	2	61		65				
1676 Kariba	8	38	292	67	3.167335	3	1	64		100				
1682 Karel	232	32	51	41	3.37485			54		84		36		
1691 Oort	152	48	46	65	10.2684			86		60				
1703 Barry	46	−76	222	−71	107.05			89		138				
1704 Wachmann	267	41	90	40	3.31391			54		135				
1709 Ukraina	165	−61	2	−40	7.30517	2	1	46		79				
1715 Salli	95	−24	254	−48	11.08867	2	1	84		97				
1719 Jens	286	−88	55	−42	5.87016	4	2	78		53				
1735 ITA	39	−46	177	−51	12.6103			148		107				
1738 Oosterhoff	14	−69	176	−65	4.44896			109		105				
1742 Schaifers	198	57	47	55	8.53270	3	1	106						

Table 5.1: *continued.*

Asteroid	λ_1 [deg]	β_1 [deg]	λ_2 [deg]	β_2 [deg]	P [hours]	N_{lc}	N_{app}	N_{689}	N_{699}	N_{703}	N_{E12}	N_{G96}	N_{950}	N_{Hip}
1746 Brouwer	85	−40	278	−56	19.7254	4	1	88		64				
1747 Wright	227	31			5.28796			70		55				
1772 Gagarin	85	−9	180	23	10.93792	3	1	46		110				
1785 Wurm	11	57	192	47	3.26934	2	1	43		115				
1835 Gajdariya	32	72	202	70	6.33768			66		86				
1837 Osita	167	−64	352	−54	3.81879			82		62				
1838 Ursa	40	61			16.1635			102		91				
1889 Pakhmutova	22	−76	167	−40	17.5157			68		46	35			
1905 Ambartsumian	52	−64	241	−68	92.153			50		101				
1927 Suvanto	74	73	278	23	8.16154	4	1	64		119				
1930 Lucifer	32	17	211	−19	13.0536	6	1	106		43	66			
1933 Tinchen	113	26	309	36	3.67062			72		103				
1946 Walraven	22	−61	251	−83	10.2101			101		73				
1950 Wempe	90	−41	258	−45	16.7953	1	1	96		46				
1963 Bezovec	219	7			18.1655	12	2	103		40				
1996 Adams	107	55			3.31114			82		120				
2002 Euler	30	44	188	47	5.99264	7	2			85				
2094 Magnitka	107	57	272	48	6.11219			25		84				
2156 Kate	49	74			5.62215	4	1			44				
2275 Cuitlahuac	315	−54	156	−68	6.29009	5	1			104				
2510 Shandong	256	27	71	27	5.94639	4	1			132				
2606 Odessa	25	−81	283	−88	8.2444	3	1	25		129				
2679 Kittisvaara	163	−36	334	−14	10.1003	4	1			108				
2709 Sagan	302	−14	124	−35	5.25636	6	2			160				
2725 David	205	−43	66	−54	9.95795	3	1	37		115				
2839 Annette	341	−49	154	−36	10.4609	8	1			99				
2957 Tatsuo	81	45	248	32	6.82043	13	1	33		102				
2991 Bilbo	277	54	90	51	4.06175	3	1			97				
3258 Somnium	117	−77			5.33806	7	1			121				
3279 Solon	189	−34			8.1041	3	1			137				
3428 Roberts	82	54	242	50	3.27835			24		129				
3497 Innanen	304	72	96	33	7.17650	6	1			109				
3678 Mongmanwai	125	−65			4.18297	2	1			103		31		
3722 Urata	260	−22	77	−9	5.5671	10	3			70				
3773 Smithsonian	150	−59	333	−63	6.98130	5	1			127				
3896 Pordenone	355	−26	180	−46	4.00366	3	1	22		71				
3918 Brel	71	63	338	42	3.09679	1	1			114				
4399 Ashizuri	268	−48	42	−59	2.830301	4	1	20		84				
4483 Petofi	107	40			4.33299	3	1			36				

Table 5.1: *continued.*

Asteroid	λ_1 [deg]	β_1 [deg]	λ_2 [deg]	β_2 [deg]	P [hours]	$N_{\rm lc}$	$N_{\rm app}$	N_{689}	N_{699}	N_{703}	$N_{\rm E12}$	$N_{\rm G96}$	N_{950}	$N_{\rm Hip}$
4570 Runcorn	120	55	285	43	20.1511	11	1			87				
4606 Saheki	41	69	223	66	4.97347	6	1			123				
4954 Eric	86	−54			12.05207	7	2			68				
5281 Lindstrom	238	−72	84	−81	9.2511	2	1			76				
5559 1990 MV	185	−24	1	−52	14.9645	4	1			139				
6406 1992 MJ	229	−70	34	−77	6.81813	3	1			107				
7043 Godart	73	61	331	59	8.4518	4	1			121				
7517 1989 AD	314	−60	123	−51	9.7094	4	1			81				
8132 Vitginzburg	33	−66	193	−48	7.27529	3	1			100				
8359 1989 WD	121	−68	274	−68	2.89103	6	1			105				
10772 1990 YM	16	46			68.82	5	1			73				
16403 1984 WJ_1	216	30	13	48	7.53748	1	1			94				
31383 1998 XJ_{94}	110	−74	279	−63	4.16818	4	1			71				
33116 1998 BO_{12}	242	69	45	58	6.34669	4	1			122				
52820 1998 RS_2	228	−57	58	−48	2.13412	1	1			45				
57394 2001 RD_{84}	65	68	241	59	6.7199	4	1			47				

Table 5.2: *List of partial models derived from combined data sets. For each asteroid, there is the mean ecliptic latitude β of the pole direction and its dispersion Δ, the other parameters have the same meaning as in Table 5.1. The uncertainty of the rotational period is of the order of the last decimal place of period values P.*

Asteroid	β [deg]	Δ [deg]	P [hours]	N_{lc}	N_{app}	N_{689}	N_{699}	N_{703}	N_{E12}	N_{G96}	N_{950}	N_{Hip}
104 Klymene	56	4	8.98059	7	2	163		100				
180 Garumna	−71	10	23.8590	23	2	153		76				
187 Lamberta	−68	5	10.66703	11	3	166		92				
214 Aschera	53	10	6.83319	5	1	168		62				
252 Clementina	65	18	10.86193	12	2	155		108				
270 Anahita	−60	2	15.05908	12	4	286		76				
391 Ingeborg	−68	13	26.4145	24	2	141		96				
394 Arduina	−69	23	16.6218	8	1	167		72				
407 Arachne	−49	12	22.6264	5	1	164		89				
430 Hybris	−68	14	7.21655			105		54				
502 Sigune	−50	9	10.92667	9	2	157		52				
510 Mabella	−59	12	19.4304	6	2	145		60				
523 Ada	−69	3	10.03239			145		43				
564 Dudu	−71	19	8.88503	3	1	120		118				
604 Tekmessa	64	1	5.55927			176		80				
616 Elly	66	24	5.29771	4	1	101		133				
622 Esther	−59	11	47.5040	5	1	128		139				
638 Moira	16	9	9.87515			172		90				
670 Ottegebe	54	6	10.03993			224		100				
686 Gersuind	51	16	6.31240			153		141				
689 Zita	−72	17	6.42391			99		103				
692 Hippodamia	−36	19	8.99689	3	1	152		102				
706 Hirundo	75	5	22.0161	6	1	119		84				
707 Steina	−66	14	428.0	5	1	163		103				
718 Erida	−52	9	17.4462			128		108				
734 Benda	59	6	7.10552	10	1	143		83				
746 Marlu	−67	1	7.78887	3	1	146		55				
782 Montefiore	−64	16	4.072747	1	1	130		118				
789 Lena	65	10	5.84234			135		96				
823 Sisigambis	57	9	146.58	8	1	123		90				
851 Zeissia	66	7	9.33173	1	1	90		88				
868 Lova	−53	23	41.151	2	1	148		135				
877 Walkure	53	12	17.4217	3	1	141	45	104		32		
885 Ulrike	−66	10	4.90616			133		55				

Table 5.2: *continued.*

Asteroid	β [deg]	Δ [deg]	P [hours]	N_{lc}	N_{app}	N_{689}	N_{699}	N_{703}	N_{E12}	N_{G96}	N_{950}	N_{Hip}
899 Jokaste	−58	19	6.24812	3	1	140			43			
1003 Lilofee	70	6	8.24991			107		83				
1013 Tombecka	55	3	6.05017	1	1	160		87				
1021 Flammario	51	17	12.15184	10	2	153		90				
1023 Thomana	−60	11	17.5610	8	1	161		102				
1044 Teutonia	64	13	3.156903			125		104				
1103 Sequoia	−48	19	3.037977	2	1	111		36	30			
1119 Euboea	62	10	11.3981			132		147				
1125 China	−43	15	5.36865			69		72				
1135 Colchis	−74	16	23.4829			142		97				
1185 Nikko	46	12	3.78615	3	1	91		46	32			
1192 Prisma	−84	14	6.55836	5	1	44		43				
1214 Richilde	−59	15	9.86687	4	1	101		78				
1231 Auricula	−72	6	3.98158			73		84				
1244 Deira	−58	3	216.97	20	1	146		63				
1251 Hedera	−51	10	19.9020	9	1	123		116				
1276 Ucclia	−67	2	4.90748			114		45				
1281 Jeanne	15	24	15.3038			132		133				
1282 Utopia	−39	21	13.6228	4	1	116		72				
1321 Majuba	53	8	5.22032	2	1	114		74				
1331 Solvejg	−70	13	19.2893	2	1	176		116				
1335 Demoulina	59	8	74.940			91		93				
1339 Desagneauxa	67	20	9.37510			78		120				
1350 Rosselia	−58	13	8.14011	1	1	114		48				
1369 Ostanina	−67	20	8.39993			98		104				
1388 Aphrodite	51	10	11.9438	11	1	89		81				
1396 Outeniqua	60	8	3.08175	2	1	112		68				
1400 Tirela	−68	18	13.3538			57		95				
1403 Idelsonia	6	21	5.45924			108		100				
1424 Sundmania	63	22	94.537	14	1	133		128				
1493 Sigrid	70	4	43.179			78		103				
1494 Savo	−61	8	5.35059			79		92				
1496 Turku	−74	6	6.47374			79		91				
1505 Koranna	−58	16	4.45185			117		115				
1527 Malmquista	51	10	14.0591			49		107				
1545 Thernoe	−69	11	17.2030			70		50				
1547 Nele	55	20	7.09742			132		76				
1592 Mathieu	−6	10	14.2404	9	1	41		121				
1617 Alschmitt	−62	7	7.06064			101		134				

Table 5.2: *continued.*

Asteroid	β [deg]	Δ [deg]	P [hours]	N_{lc}	N_{app}	N_{689}	N_{699}	N_{703}	N_{E12}	N_{G96}	N_{950}	N_{Hip}
1618 Dawn	−58	5	43.219			93		91				
1619 Ueta	36	5	2.717943	5	1	122		51				
1623 Vivian	−82	4	20.5235			77		58				
1662 Hoffmann	−44	5	8.78225			81		80				
1701 Okavango	−70		13.1918	1	1	93		96				
1722 Goffin	−66	18	29.0873	3	1	104		92				
1728 Goethe	66	1	79.299			129		96				
1797 Schaumasse	79	3	6.11175	4	1	84		110				
1805 Dirikis	57	1	23.4544			117		91				
1825 Klare	−77	10	4.74289			89		44				
1826 Miller	−13	10	26.1847			110		83				
1841 Masaryk	69	10	7.54302			105		99				
1847 Stobbe	−68	23	5.61757			237		108				
1892 Lucienne	−59	16	9.31556	1	1	79		125				
1900 Katyusha	−63	7	9.50366			82		60				
2001 Einstein	−51	22	5.4850	2	1			84				
2086 Newell	−62	10	78.09	10	1	24		84				
2393 Suzuki	55	12	9.2876					92				
2430 Bruce	−48	20	129.75	15	1			112				
3017 Petrovic	−50	13	4.08037	3	1			114				
3544 Borodino	−56	12	5.43460	2	1			74				
3577 Putilin	14	10	29.5176	30	2			76				
3737 Beckman	−43	23	3.120262	2	1			40				
3786 Yamada	55	14	4.03295	3	1			71				
4209 Briggs	−70	16	12.2530	2	1			64				
4265 Kani	44	3	5.72753	4	1	21		183				
6179 Brett	−40	22	9.4063	6	1			93				
6403 Steverin	46	15	3.49119	2	1			74				
7055 1989 KB	−61	10	4.16879	7	1			117				
7304 Namiki	−48	1	8.8738	3	1			131				
7360 Moberg	−24	13	4.58534	3	1			103				
28736 2000 GE_{133}	−68	16	4.65442	3	1			118				

5.2 Asteroid models based on the Catalina Sky Survey data

Here we present new asteroid models derived only from the CSS data. Because of the poor quality of the photometry, it was necessary to apply additional tests to validate these models. We used the tests described in Section 4.1.2, which were sufficient if photometry from the USNO-Flagstaff station was present. In Section 4.2.2, we have shown that reliable asteroid models can be derived also from the Catalina Sky Survey data alone and have given a manual how to proceed during the computation when the rotational period is unknown: The solution should be searched for all periods in an interval of 2–100 hours, and the stability of the solution should be tested for at least two different shape parametrization. The correct solution had to be stable for both low ($n = 3$) and high ($n = 6$) shape resolutions. We followed this scenario: We searched for the model in the multi-dimensional parameter space for shape resolutions $n = 3$ and $n = 6$ and compared the derived rotational states.

There are two different groups of asteroid model based on the CSS data: (i) models with previously reported synodic periods determined from dense data (we did not have these dense data, period values were taken from the literature, usually from the Minor Planet Lightcurve Database), and (ii) models with previously unknown rotational periods. In the first case, we could compare the published period with the period derived by the lightcurve inversion (see Table 5.3, columns 7 and 9). If both periods agreed within their uncertainties, we considered the solution to be reliable. This test could not be performed for the second group of models, so we had to use only additional reliability tests from Section 4.2.2.

In Table 5.3, we present 21 asteroid models based fully on the CSS data. Previous period estimates were not available for 13 of them. All of these 21 models have higher uncertainties of pole orientations and lower shape resolution than models based on combined data and are possible candidates for follow up observations for the period confirmation and a more detailed shape determination.

While the lightcurve inversion is more successful for asteroids with higher lightcurve amplitudes, the derived sample of asteroid parameters is significantly biased. For example, shapes are more elongated than it is usual in the whole population. Careful de-biasing of the model sample will be necessary before its use in any statistical study and physical interpretation.

Models based on the CSS data are good candidates for follow-up observations, additional dense photometry should confirm derived solutions and lead to more detailed shape models.

Table 5.3: *List of new asteroid models derived from the Catalina Sky Survey data alone. For each asteroid, the table gives the ecliptic coordinates λ_1 and β_1 of the pole solution, the corresponding mirror solution λ_2 and β_2, the sidereal rotational period P, the number of sparse data points N_{703} from the CSS, and the previously published period value P_{publ} with the reference.*

Asteroid	λ_1 [deg]	β_1 [deg]	λ_2 [deg]	β_2 [deg]	P [hours]	N_{703}	P_{publ} [hours]	Period reference
2112 Ulyanov	156	48	334	65	3.04071	118	3.000	Maleszewski and Clark (2004)
2384 Schulhof	196	−60	45	−42	3.29367	121	3.294	Ditteon et al. (2002)
2617 Jiangxi	224	76	1	54	11.7730	124	11.79	Carbo et al. (2009)
3170 Dzhanibekov	217	60	21	64	6.07168	105	6.0724	Molnar et al. (2008)
4507 1990 FV	143	55	323	49	6.57933	84	6.58	Yoshida et al. (2005)
5647 1990 TZ	253	77	119	−19	6.13867	87	6.144	Bembrick and Bolt (2003)
10826 1993 SK_{16}	260	−56	60	−34	13.8327	90	13.835	Galad (2008)
19848 Yeungchuchiu	190	−68			3.45104	104	3.450	Yeung (2006)
3097 Tacitus	229	71	72	62	8.7759	99		
4611 Vulkaneifel	5	−86	197	−50	3.75635	148		
5461 Autumn	249	−26	79	−43	20.0929	106		
5625 1991 AO_2	265	−52	97	−78	6.67411	110		
5960 Wakkanai	226	−69	69	−61	4.96286	102		
7201 Kuritariku	22	67	249	64	48.849	103		
7632 Stanislav	234	−50	46	−45	5.29073	99		
7905 Juzoitami	105	−76	226	−55	2.72744	118		
13002 1982 BJ_{13}	58	−50	245	−57	3.13844	110		
15621 Erikhovland	360	−35			5.34226	102		
16009 1999 CM_8	283	44			8.3476	124		
16847 Sanpoloamosciano	91	−24			8.1845	114		
26792 1975 LY	226	68			79.15	140		

Chapter 6

Analysis of asteroid's physical parameters

In this chapter, we present an analysis of asteroid parameters that we derived using the lightcurve inversion method (rotational periods, spin axis orientations) or adopted from different sources (e.g., proper elements from the AstDyS database or diameters from WISE, Masiero et al. 2011). We investigated properties of the whole population of asteroids, as well as of individual asteroid families. In Section 6.1.1, we present results of a numerical simulation that allowed us to estimate the bias in the pole directions derived by the lightcurve inversion method. Using these results, we corrected the observed pole distributions for this effect and present the de-biased pole distributions in Section 6.1.2. A study of spin vector properties among four asteroid families is presented in Section 6.1.3. Finally, to explain the de-biased pole-latitude distribution, we present a simple theoretical model of the temporal evolution of the spin-vector directions in Section 6.2. By this model, we also constrained the free scaling parameter c_{YORP} describing our uncertainty in the shape and the magnitude of the YORP momentum (i.e., how strong/weak the YORP effect is).

Previous studies have used spin state results determined by different techniques, such as amplitude–epoch, lightcurve inversion or radar methods (e.g., Kryszczyńska et al. 2007). If there were multiple solutions for a given asteroid, the most probable one or simply the weighted mean was taken. However, this could cause systematic deviations in the parameter interpretation. In our study, we used only results based on the lightcurve inversion method – i.e., unique and partial models (models with secure values of rotational periods and pole latitudes, pole longitudes are uncertain) presented in this work and models from DAMIT. Our sample consisted of 498 asteroid models: 281 new models, 18 updated models from DAMIT, 106 new partial models and 93 models from DAMIT. We had models for 481 MBAs, 12 NEAs, 3 Hungaria, and 1 Trojan, so a statistical study was possible only for the MBAs. In many cases, there was an ambiguity in the pole direction since there were two undistinguishable mirror solutions. For our statistical analysis we chose the one with the formally better fit.

In Fig. 6.1, we show (among other things that will be discussed later) the relation between the proper semi-major axis and the proper eccentricity for asteroids in our sample and for ∼100 000 main belt asteroids. The positions of studied

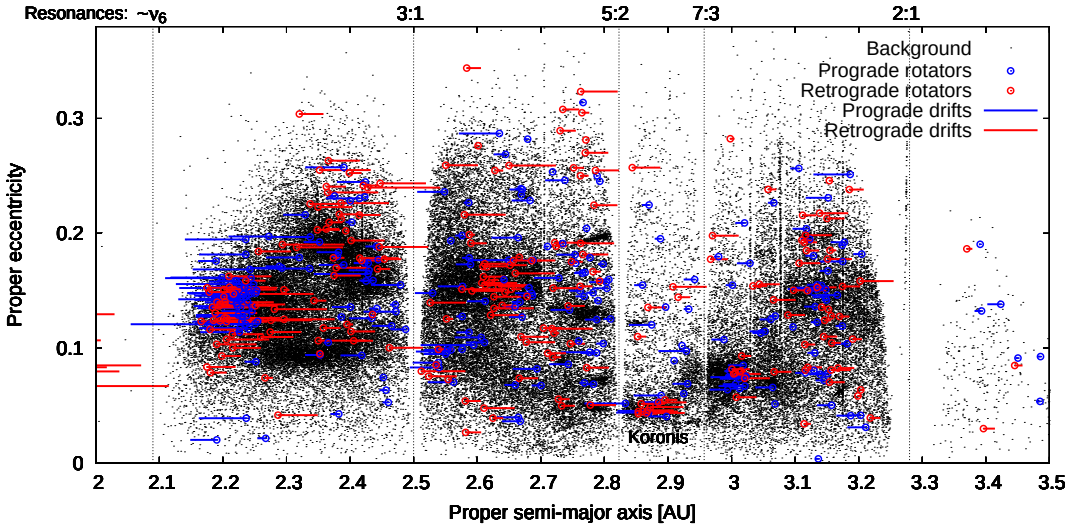

Figure 6.1: *Relation between the proper semi-major axis and the proper eccentricity for asteroids in our sample and for the first 100 000 numbered asteroids for comparison. Main resonances are shown by dotted lines. Prograde rotators are plotted with blue circles and retrograde rotators with red circles. The horizontal lines represent for each asteroid its estimated past Yarkovsky drift (i.e., where the asteroid came from) during the collisional lifetime computed with Eq. (6.6). Proper elements are adopted from the AstDyS database.*

asteroids correlate with the MBAs population and so derived models are not significantly biased with respect to orbits, e.g. they do not lie only in the inner main belt. However, due to the selection effect (higher albedo, closer to the Earth), the inner part of the main belt is more populated in our model sample than the outer parts. Several asteroids in Fig. 6.1 with semi-major axis $a > 3.3$ AU belong to the Cybele group, e.g. (121) Hermione.

6.1 Spin-vector distribution

First statistical analyses of the spin-vector distribution were presented by Magnusson (1986, 1990) and Drummond et al. (1988b, 1991), later by Pravec et al. (2002) and Skoglöv and Erikson (2002). They independantly observed a lack of poles close to the ecliptic plane. Kryszczyńska et al. (2007) used more objects in the analysis, finding that the distribution was strongly anisotropic with a moderate excess of prograde spins in the limited size range from 100 to 150 km. Interpretation of the depopulation of poles close to the ecliptic plane is still unclear. Probable candidates are selection effects, the role of inclination, the YORP effect[1] (Rubincam 2000; Vokrouhlický et al. 2003), or a combination of these. The YORP effect acts on timescales <4 Gyr only on small bodies with $D \lesssim 40$ km. Asteroids with these sizes have non-Maxwellian spin rate distribution (Pravec and Harris 2000), which is particularly evident for asteroids with $D < 14$ km (Warner et al.

[1]Yarkovsky–O'Keefe–Radzievskii–Paddack effect, a torque caused by the recoil force from the anisotropic thermal emission

2009). It is believed that the YORP effect is responsible for this trend since it can either spin up or spin down (i.e, decrease or increase of the rotational period) an irregularly-shaped asteroid on the timescale shorter than the typical time between collisions and also affects the obliquity of spin axes (Rubincam 2000; Bottke et al. 2006).

In the Near Earth Asteroids (NEAs) population, the latitude distribution of poles is different from that of MBAs (La Spina et al. 2004; Kryszczyńska et al. 2007). There is a significant excess of retrograde spins probably caused by the transport mechanism of MBAs to Earth-crossing space by gravitational resonances and the Yarkovsky effect[2] (Morbidelli and Vokrouhlický 2003).

According to Kryszczyńska et al. (2007), there is no statistically significant clustering in the longitude of poles of either MBAs or NEAs. Bowell et al. (2011) determined ecliptic longitudes for more than 30 000 asteroids using the data from the Lowell Observatory photometric database. They claim that for the main belt as a whole, there is a depletion of spin-axis ecliptic longitudes near 140° and excesses near 30° and 90°.

The observed latitude and longitude distributions of the spin vector can be biased by the convex inversion method and, therefore, this bias should be taken into consideration and the observed pole distribution should be correctly de-biased. In general, models for asteroids with higher amplitudes are more often successfully derived than those asteroids with lower amplitudes. This is because, while the accuracy of the sparse photometry in both cases is roughly the same, the signal-to-noise ratio is significantly better for higher amplitude lightcurves. If we assume two bodies with the same shapes and orbits and *different* ecliptic latitudes of the poles, the body with the higher absolute value of the ecliptic latitude usually has a higher amplitude. We investigated this effect numerically in Section 6.1.1. A study of de-biased latitude and longitude distributions is then presented in the Section 6.1.2. In Section 6.1.3, we focus on spin vector properties in four individual asteroid families – Flora, Koronis, Eunomia and Eos.

6.1.1 Biases of the LI method

We developed a numerical algorithm to estimate the selection effect of the lightcurve inversion method and used this approach to de-bias the observed distribution of asteroid pole directions. The algorithm was as follows:

1. For a model with a known shape, we randomly generated a new pole direction. The overall distribution of poles was *isotropic*.

2. For each shape with the new rotational state but with the period unchanged, we computed synthetic lightcurves for the same epochs as observed ones.

3. To each data point i of the synthetic lightcurve, we added the corresponding noise δ_i given by:

$$\delta_i = \frac{L_i^{\mathrm{obs}} - L_i^{\mathrm{mod}}}{L_i^{\mathrm{mod}}}, \tag{6.1}$$

[2]Yarkovsky effect, a thermal force acting on a rotating asteroid

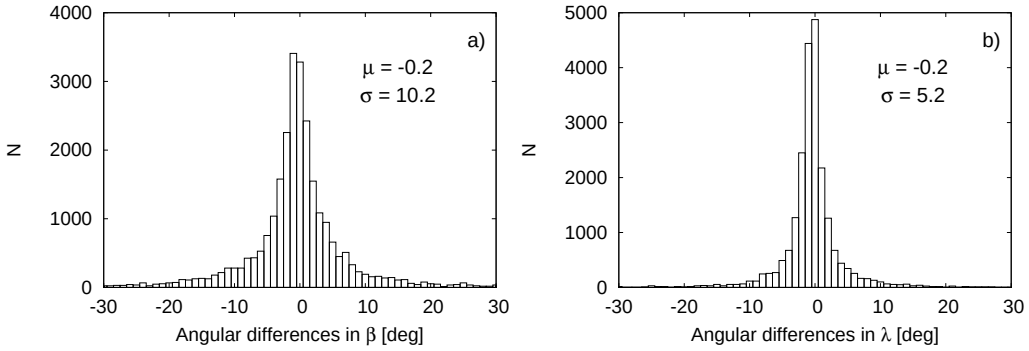

Figure 6.2: *Histograms of the angular differences between the generated and derived ecliptic latitudes and longitudes of the pole directions for all successfully derived synthetic models: a)* $\beta_{\mathrm{comp}} - \beta_{\mathrm{gen}}$*, where* β_{gen} *and* β_{comp} *are generated and computed ecliptic latitudes and similarly b)* $(\lambda_{\mathrm{comp}} - \lambda_{\mathrm{gen}}) \cos \beta_{\mathrm{gen}}$ *for ecliptic longitudes.*

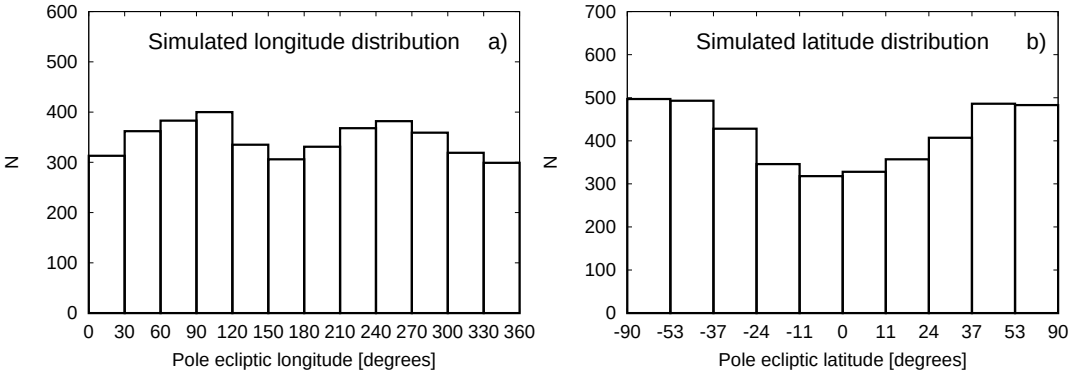

Figure 6.3: *Panel a) shows the simulated ecliptic longitude distribution of all successfully derived models, the latitude distribution is plotted in panel b). The bins are equidistant in* λ *and sin*β *for longitudes and latitudes, respectively.*

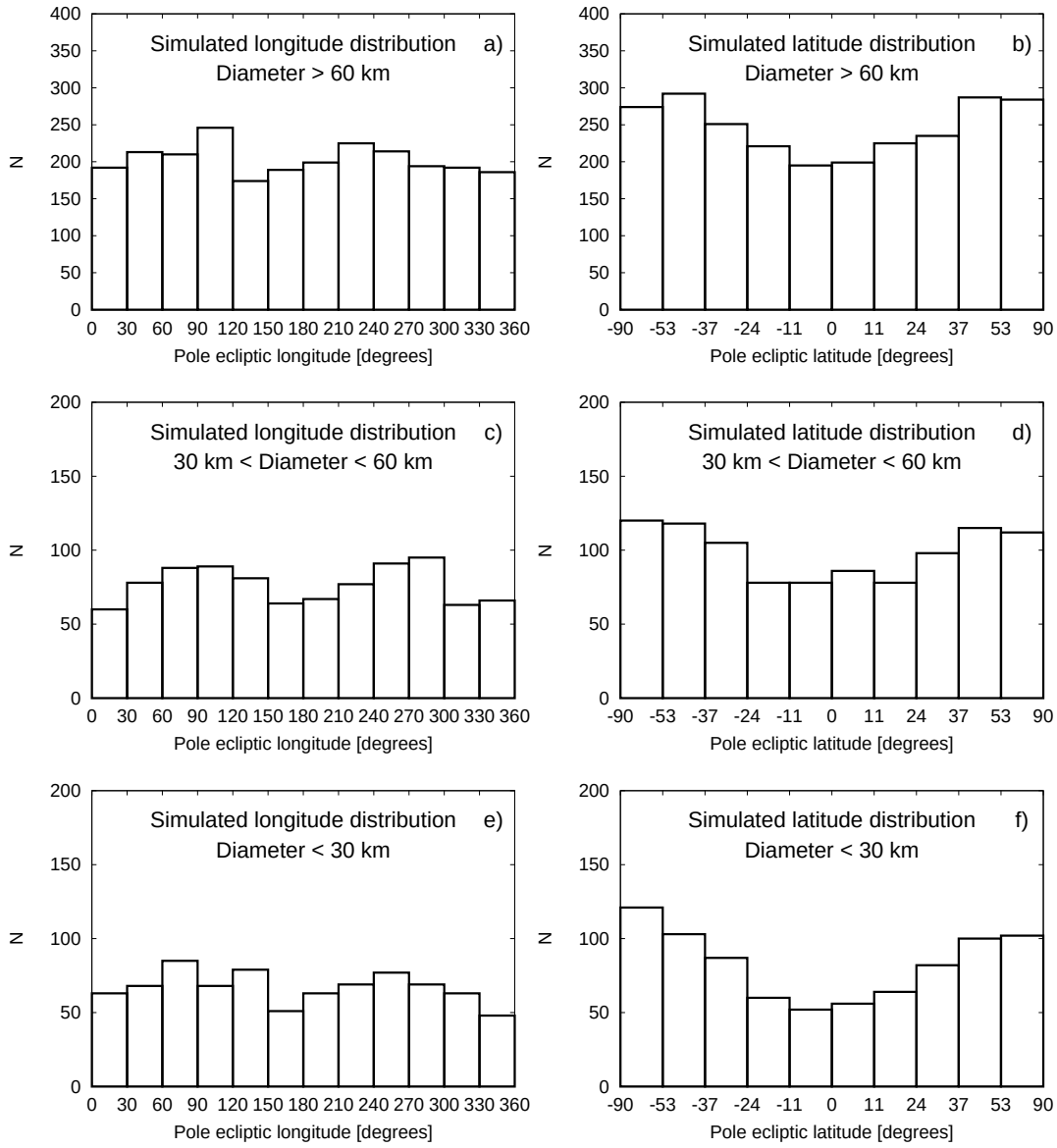

Figure 6.4: *Histograms showing the simulated longitude and latitude distributions of MBAs for different size groups, excluding the Koronis cluster members. Panel a) shows the simulated longitude distribution for asteroids with the diameters larger than 60 km, c) for asteroids with the size in range of 30–60 km, e) for asteroids with diameters smaller than 30 km. Similarly, panels. b), d) and f) show the simulated latitude distributions for different size ranges. The bins are equidistant in* λ *and* $sin\beta$ *for longitudes and latitudes, respectively.*

where $L_i^{\rm obs}$ is i-th brightness observed and $L_i^{\rm mod}$ is i-th brightness computed, both for the original model. This gave us synthetic lightcurve data equivalent to the original observed data, but for a new pole direction.

4. Finally, we performed a lightcurve inversion the same way as with the actual data and tried to derive a model.

5. We repeated steps 1–4 for 50 random poles for each asteroid model.

In this simulation, we used 80 models derived from combined dense and sparse data sets and 89 models from the DAMIT (a sample of models that was available in the time when the simulation was executed).

For each successfully derived model we have the generated pole direction ($\lambda_{\rm gen}$, $\beta_{\rm gen}$) and the period $P_{\rm gen}$, and also the computed pole and period: $\lambda_{\rm comp}$, $\beta_{\rm comp}$, $P_{\rm comp}$. We computed the angular differences between the generated and the derived ecliptic latitude and longitude of the pole direction: $\beta_{\rm comp} - \beta_{\rm gen}$ and $(\lambda_{\rm comp} - \lambda_{\rm gen}) \cos \beta_{\rm gen}$ (the $\cos \beta_{\rm gen}$ factor is used for the correction of the different distances of meridians near the equator and poles). In Fig. 6.2, we show the histograms of these differences in a) ecliptic latitudes and b) ecliptic longitudes. We computed the mean and the standard deviation (μ, σ) of the histograms. We found values of ($-0.2°$, $10.2°$) for latitudes and ($-0.2°$, $5.2°$) for longitudes. The standard deviation σ is directly related to the typical uncertainty that we can expect in the pole determination by the lightcurve inversion method, which is $\sim 5°/\cos\beta$ in λ and $\sim 10°$ in β.

In Fig. 6.3, we constructed histograms of the longitude and latitude distributions for all *successful* models. As in all similar plots, the width of the latitude and longitude bins corresponds to equal surfaces on the (λ, β)-sphere (bins are equidistant in $\sin\beta$ for latitudes and in λ for longitudes). The longitude and latitude distributions of *all* generated models were not exactly uniform, the amount of longitudes and latitudes in bins slightly differed. To remove this effect, we divided the longitude and latitude distributions of successfully derived models by the corresponding pole distributions of all generated models normalized to unity. This correction was also applied to pole distributions for different size ranges in Figs. 6.4b,d,f, and similarly to longitude distributions in Figs. 6.3a and 6.4a,c,e.

It is obvious that the LI method is more efficient for asteroids with higher $|\beta|$. The amount of successfully derived models with $|\beta| \sim 0°$ is about 30% lower than with $|\beta| > 53°$. In Figs. 6.4b,d,f, we constructed the histograms of latitude distributions for successfully derived models and distinguished three size ranges (the particular choice of the ranges will be discussed in Section 6.1.2). All three plots look very similar, except that with decreasing size, the ratio between models with $|\beta| \sim 0°$ and $|\beta| > 53°$ goes down. This ratio is $\sim$75% for $D > 60$ km, $\sim$65% for 30 km $< D <$ 60 km and $\sim$60% for $D <$ 30 km.

In Figs. 6.3a and 6.4a,c,e, we constructed histograms of the longitude distributions for all successful models in a similar way as for latitudes. There is a moderate excess of poles with longitudes $\lambda \sim 90°$ and $\lambda \sim 270°$. We investigated several hypotheses that could be responsible for this effect, but with a negative result. More careful analysis will be an object of our future work.

6.1.2 Analysis of pole directions

In the following study of spin axis directions, we did not use the Koronis family members because their spin vectors are clustered towards two values of the obliquity (Slivan 2002, will be discussed in more details in Section 6.1.3).

The histograms in Figs. 6.3b and 6.4b,d,f define the bias in latitude of the lightcurve inversion method and can be used for de-biasing the observed latitude distributions. The de-biased histogram of latitudes for the whole MBA population is plotted in Fig. 6.5b. We confirmed the expectation that there is a lack of asteroids with latitudes close to the ecliptic plane. The latitude distribution is clearly asymmetric: about half of the retrograde rotators have latitudes in the bin $(-53°, -90°)$. On the other hand, about a third of asteroids with prograde spins is in the corresponding bin $(53°, 90°)$. Moreover, the remaining prograde bins are more populated than the corresponding retrograde ones. From a detailed look at the plot we can see that there are up to 15% more prograde rotators among the MBAs in our sample.

In Fig. 6.6, we show the dependence of the ecliptic latitude β of the pole direction on the diameter D (most of the diameters used are based on the WISE data, or occultation profiles with typical uncertainties of ±10%, there should be no significant trend in these diameter values). Even for diameters $D \lesssim 50$ km, the clustering of the latitudes towards higher absolute values, and conversely, the depletion close to the ecliptic plane are obvious and markedly so for $D \lesssim 30$ km. Note that we plotted here the *observed* latitudes, the bias caused by the lightcurve inversion was not removed. Actually, there should be about 30–40% more asteroids with $|\beta| \lesssim 20°$. This plot is rather illustrative and gives us a qualitative view on the diameter-latitude dependence. While there are only few asteroids with $|\beta| \lesssim 20°$, the plot will look very similar also after the lightcurve inversion bias is removed. Asteroids with larger diameters have a more isotropic distribution of latitudes with a moderate excess of prograde rotators. Based on Fig. 6.6, we resolved three different size groups of asteroids: <30 km, 30–60 km and >60 km. In Figs. 6.7b,d,f, we plotted the latitude distributions of asteroids with respect to their diameters.

The latitude distribution for asteroids with $D > 60$ km (Fig. 6.7b) is flat for latitudes lower than 11° and for larger latitudes it exhibits an evident excess of prograde rotators. This is in agreement with theoretical arguments presented by Davis et al. (1989) and recently by Johansen and Lacerda (2010). On the other hand, the latitude distribution for asteroids with $D < 30$ km (Fig. 6.7f) exhibits a strong depopulation of poles close to the ecliptic plane (i.e. small $|\beta|$). The latitude distribution for asteroids with intermediate diameters of 30–60 km (Fig. 6.7d) is also somewhat clustered towards higher latitudes but the bins for small latitudes are more populated. Therefore, it is probably a transition region between the two distinct distributions.

It is evident that the depopulation concerns mainly objects with diameters $D \lesssim 30$ km (the distribution for the intermediate size sample shows that the limit is probably ∼50 km). This size roughly corresponds to the value, when the YORP effect starts to be important and hence it is a natural candidate for a physical explanation. It is known from previous studies (Pravec and Harris 2000; Rubincam 2000) that the YORP effect is significantly altering the *periods* and also

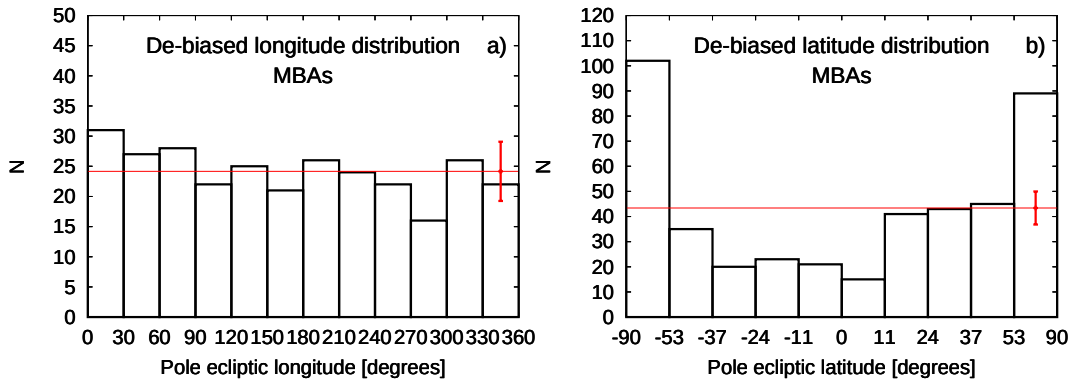

Figure 6.5: *Panel a) shows the de-biased ecliptic longitude distribution of all MBAs in our sample except the Koronis family members. The longitude bins are equidistant in λ. In panel b), the de-biased latitude distribution of all MBAs is plotted, again except the Koronis family members. The latitude bins are equidistant in $sin\beta$. The thin horizontal line corresponds to the average value $\bar{N}$ and the errorbar to $\sqrt{\bar{N}}$.*

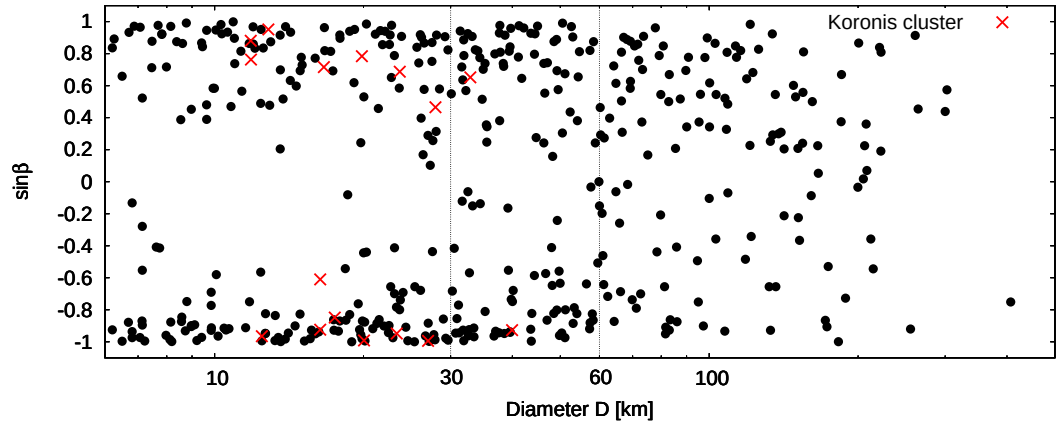

Figure 6.6: *Dependence of the ecliptic latitude β (plotted as $\sin\beta$) of the pole direction on the models diameter D. Notice the gap of small latitudes for asteroids with $D <$ 30 km. Members of the Koronis cluster are plotted with crosses.*

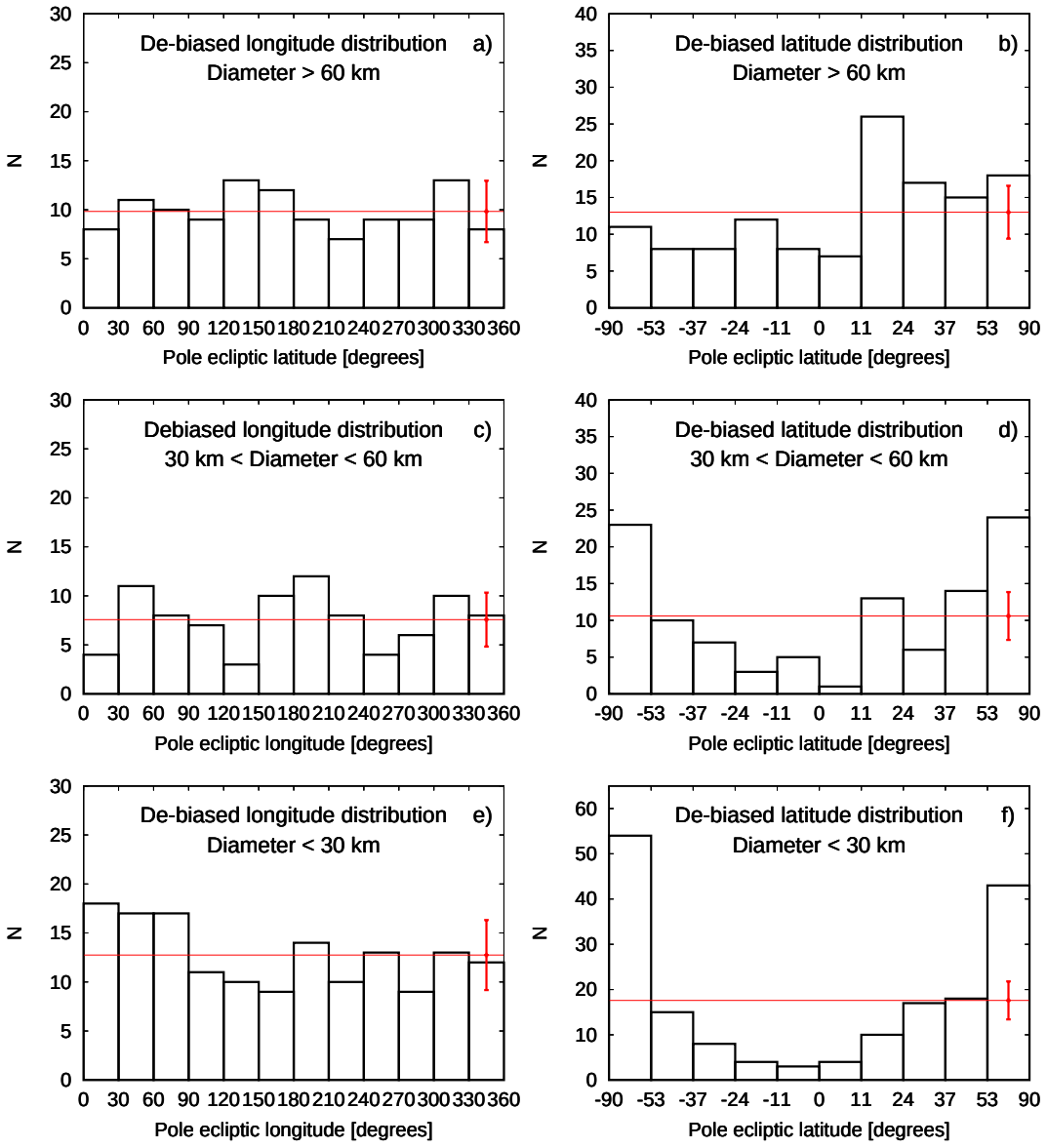

Figure 6.7: *Histograms showing the observed longitude and latitude distributions of MBAs (except Koronis cluster members) for different size ranges. Fig. a) shows the longitude distribution for asteroids with diameters larger than 60 km, c) for asteroids with diameters in the range of 30–60 km, e) for asteroids with diameters smaller than 30 km, and similarly b), d) and f) for latitudes. The bins width in the longitude λ and the latitude β corresponds to similar surfaces on the (λ, β)-sphere, so the bins are equidistant in λ and $sin\beta$. The thin horozontal line corresponds to the average value $\bar{N}$ and the errorbar to $\sqrt{\bar{N}}$.*

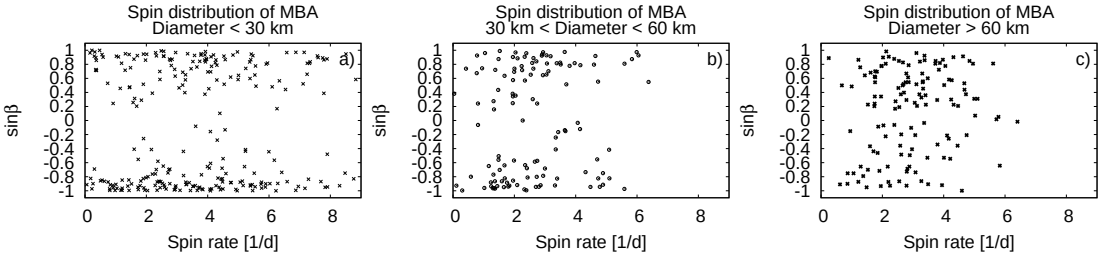

Figure 6.8: *Dependence of the ecliptic latitude β (plotted as $\sin\beta$) of the pole direction on the model's spin rate: a) for asteroids with diameters $D < 30$ km, b) for asteroids with diameters $30\ \text{km} < D < 60$ km, and c) for asteroids with $D > 60$ km.*

spin vectors of small asteroids on a timescale shorter than their typical collisional lifetime (timescales are discussed in more details in Section 6.2). In Fig. 6.8, we show the relation between the spin rate and the latitude for small ($D < 30$ km), intermediate ($30 < D < 60$ km), and large ($D > 60$ km) groups of asteroids. In concert with the YORP theory, the excess of fast and slow rotators and the evolution of the latitudes towards higher absolute values are evident in the small asteroid sample.

We are not aware of any other physical effects in the main belt that could explain the non-uniform de-biased observed latitude distribution of small asteroids ($D < 30$ km). Collisions are believed to produce uniform spin distributions and close encounters with planets are common only among NEAs.

There are many additional selection effects that influence the properties of derived models, e.g., the role of amplitude, orbit, time, accuracy and geometry of observations, among others. The significance of this bias is unknown and cannot be easily determined. The main problem here is that for almost every asteroid, the photometric data are from different observers with a different number of measurements, quality, and purpose. The significance of this effect can be determined only from a comparison of models derived from real and synthetic data of known properties. This may be possible in a few years when the photometry from the Pan-STARRS, Gaia or LSST is available (data from these surveys will be well described), but not now. In the meantime, the role of the selection effects seems to be small and does not significantly affect, for example, the latitude distribution.

The de-biased longitude distributions of MBAs are plotted in Figs. 6.5a and 6.7a,c,e. They are, contrary to the latitude distributions, without any statistically significant features and have distributions very close to uniform.

In all cases, we tested a hypothesis that the observed (only illustrative) and de-biased distributions of latitudes or longitudes are uniform (using a χ^2–test[3]). The computed χ^2 and corresponding probabilities are listed in Table 6.1. Higher χ^2-values and lower probabilities mean that the supposed hypothesis "the longitude/latitude distribution is uniform" does not fit the data. If we assume a probability of 5% or lower as a threshold for rejection, we can say that all the latitude distributions (for the whole sample and for asteroids with $D < 30$ km, $30\ \text{km} < D < 60$ km and $D > 60$ km do not agree with a uniform distribution.

[3]The results based on the χ^2–test are also in agreement with the Kolmogorov–Smirnov test.

On the other hand, all longitude distributions are consistent with uniform distribution. Latitude distribution for the MBAs with diameters $D > 60$ km disagrees with the uniform distribution because of the obvious excess of prograde rotators.

Skoglöv and Erikson (2002) discussed the role of the orbital inclination in the observed distribution of latitudes. No indications of this effect were found in the asteroid sample of Kryszczyńska et al. (2007). We also did not find any indications of such correlation in our sample and so we conclude that orbital inclination does not significantly affect the distribution of latitudes.

The overall view on the model positions within the main belt of asteroids, together with their estimated total drifts and the information about whether they are prograde or retrograde rotators (Fig. 6.1), show behavior consistent with the Yarkovsky/YORP theory: There is an asymmetry of prograde and retrograde rotators near the main resonances. Prograde asteroids drift outwards from the Sun and can reach the resonance only from the left. On the other hand, retrograde rotators drift in the opposite direction and depopulate the zone on the left of the resonance because the resonance prevents the entry of new retrograde asteroids. This creates an excess of prograde rotators. The same mechanism works also in the zone right of the resonance, in this case, an excess of retrograde asteroids is now created. This effect is obvious in the close neighborhood of the ν_6 resonance, where there are mostly retrograde rotators (more than 20 retrograde rotators against 2 prograde), and 3:1 resonance, where is an excess of prograde rotators in the zone on the left (5 prograde, 2 retrograde) and of retrograde rotators in the zone on the right (7 retrograde, 2 prograde). The total drift from an asteroid's original location during the collisional lifetime computed with Equation (6.6) is inversely proportional to the size of the asteroids. Larger asteroids ($D \gtrsim 50$ km) do not drift significantly while smaller asteroids often drift of ± 0.05 AU. Note that small asteroids are found mainly in the inner or middle part of the main belt (due to selection effect; they have high albedos and are closer to the Earth). Asteroids drifting through the resonances during their collisional lifetime are interesting because of their dynamical evolution. These asteroids were either recently affected by collisions, are larger or their shape models are wrong. There seems to be several candidates for such models, four of them near the 3:1 mean-motion resonance with Jupiter and 2 near the 5:2 mean-motion resonance with the Jupiter. These asteroids are good candidates for follow up observations in order to use the new data for the shape model validation.

6.1.3 Spin vectors in asteroid families

Asteroid families are clusters of asteroids with similar proper orbital elements and often spectra that were formed by catastrophic break-ups of parent bodies or cratering events. For a preliminary family membership determination, we adopted an on-line catalog published by Nesvorný (2012) who used the Hierarchical Clustering Method[4] (HCM, Zappalá et al. 1990, 1994). There are four asteroid families

[4]In this method, the distances in proper semi-major axis ($a_{\rm d}$), proper eccentricity ($e_{\rm d}$), and proper inclination ($i_{\rm d}$) space is computed. The members of the family are then separated in the proper element space by less than a selected distance (usually, it has a unit of velocity), a free parameter often denoted as "cutoff".

Table 6.1: *Test of the hypothesis that the observed and de-biased pole distributions are drown from a uniform distribution (a χ^2–test). N is the degree of freedom.*

	$\lambda_{\rm obs}$ $N=11$		$\beta_{\rm obs}$ $N=9$		$\lambda_{\rm deb}$ $N=11$		$\beta_{\rm deb}$ $N=9$	
Diameter	χ^2	%	χ^2	%	χ^2	%	χ^2	%
all	15	17	273	$< 10^{-10}$	6.9	80	181	$< 10^{-10}$
> 60 km	3.0	99	27	0.1	4.4	95	25	0.3
$30 - 60$ km	10	51	75	10^{-10}	12	34	53	10^{-6}
< 30 km	16	13	268	$< 10^{-10}$	8.8	64	154	$< 10^{-10}$

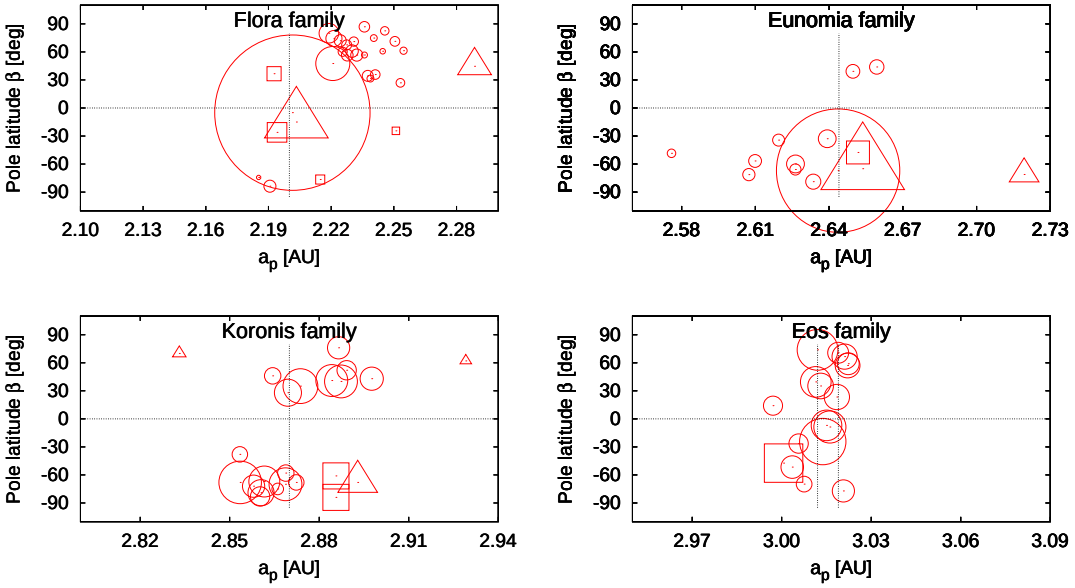

Figure 6.9: *Dependence of the pole latitude on the proper semi-major axis $a_{\rm p}$ for studied asteroid families: Flora, Eunomia, Koronis and Eos. Identified interlopers are marked by triangles, borderline cases by squares and family members by circles. Sizes of symbols are scaled with diameters (only the scale for (15) Eunomia and (85) Io was decreased by half to fit the figure). The vertical line corresponds to the likely center of the asteroid family. The Eos family is a bit asymmetric (probably due to the J 9/4 mean-motion resonance) which makes the center identification harder, so we marked two possible positions.*

for which we found at least ten members in our data set of asteroid models (we also included models based exclusively on the CSS data) – the Flora, Eunomia, Koronis, and Eos families (proper orbital elements and rotational parameters for all studied asteroids are listed in Tables 6.2, 6.3, 6.4, and 6.5). The HCM method extracts a statistically significant group of objects with similar proper orbital elements, but not all of these objects are actually real members of the collisionally born asteroid family. A fraction of objects has proper orbital elements similar to

typical proper elements of the asteroid family members only by a coincidence, the so called interlopers. Interlopers can be identified, for example, by:

- measurement of spectra, because they are usually of different taxonomic types than that of the family members,
- constructing a size distribution of the cluster, some asteroids can be too large to be created within the family and thus have to be interlopers (see, e.g., simulations by Durda et al. 2007; Benavidez et al. 2012).
- constructing a diagram of proper semi-major axis vs. absolute magnitude and computing the theoretical envelope of the family defined by the Yarkovsky semi-major axis drift and excluding outliers, i.e. relatively large asteroids far from the center (see Vokrouhlický et al. 2006b, for the case of Eos family).

These methods for family membership determination have one common characteristic – we have to determine or choose a range for a quantity that defines the family members (range of spectra, sizes, or distance from the family center), which affects the number of objects we include in the cluster.

We revised the family membership assignment by the HCM method according to above described methods for interlopers identification. In Table 6.6, we list the asteroids we excluded from the families with the reasons why we did that. Note, that we investigated the membership carefully only for asteroids which positions in the a_{p} vs. β diagram were not in agreement with the theoretical expectations according (see the next paragraph).

The theory of dynamical evolution of asteroidal families (Bottke et al. 2006) suggests that the Yarkovsky/YORP effect forces orbital parameters of smaller asteroids ($\lesssim 30 - 50$ km) to evolve – the semi-major axis of prograde rotators is slowly growing in the course of time, contrary to retrograde rotators which semi-major axis is decreasing. For each studied family, we plotted a dependence of the semi-major axes on asteroid's pole latitudes (Figure 6.9). If we remove the interlopers and borderline cases we can see for the Eunomia and Koronis families a clear trend (actually, the trend is obvious even without removing the interlopers and borderline cases): retrograde rotators lie on the left side from the center of the family, and on the other hand, prograde rotators on the right side.

In the case of the Flora family, only two retrograde rotators are present. The secular ν_6 resonance with Saturn is responsible for this deficit, because retrograde members of the Flora family are drifting towards this resonance and are subsequently removed from the family (they become NEAs).

In the Eos family, most of the studied asteroids are located close to the family center. These asteroids are, compared to the studied Flora or Eunomia members, larger and farther from the Sun, so their drifts in semi-major axis are rather small. The case of the Koronis family is discussed below.

Koronis family. A previous analysis of rotational state solutions for ten members of the Koronis asteroid family revealed a clustered distribution of their spin vectors (Slivan 2002; Slivan et al. 2003). This spin distribution was later explained by Vokrouhlický et al. (2003) as a result of the thermal YORP torques

and spin-orbital resonances that modified the spin states over the time span of 2–3 Gyr. Their modeling suggested an existence of two groups of asteroids: (a) low-obliquity retrograde objects with rotational periods $P < 5$ h or $P > 13$ h, and (b) prograde rotators with periods 4 h $< P <$ 7 h that became trapped in a spin-orbital resonance with the secular frequency s_6 and thus have similar obliquities (42° to 51°) and also similar ecliptic longitudes in the range of (24° to 73°) and (204° to 259°). All ten members of the Koronis family studied by Slivan (2002) and Slivan et al. (2003) have the expected properties except the periods of observed prograde rotators that were shifted only to higher values of 7–10 h. Slivan et al. (2009) published spin state solutions for another four members of Koronis family. Only the solution for (263) Dresda was not in agreement with the theoretical expectation.

Here, we derived seven new models of asteroids belonging to the Koronis family (according to the HCM method): (832) Karin, (1389) Onnie, (1423) Jose, (1482) Sebastiana, (1635) Bohrmann, (1835) Gajdariya and (3170) Dzanibekov, along with two partial models for (1350) Rosselina and (1618) Dawn. While most of the spin state solutions fit the theoretical expectations, rotational parameters for (832) Karin ($P = 18.3512$ h, $\lambda = 242°$, $\beta = 46°$) are outside both groups, and asteroids (1350) Rosselina and (1482) Sebastiana are low-obliquity retrograde rotators, but their periods (10.49 h for Sebastiana and 8.14 h for Rosselina) are in the middle of the "forbidden" range of $P = 5$–13 hours. Asteroid (832) Karin is the namesake and the largest member of a young (~ 5.8 My, Nesvorný and Bottke 2004) collisional family that is confined within the larger Koronis family. The spin state of (832) Karin was thus likely affected during this catastrophic event and changed to a random state that now disagrees with the clustered distribution (Slivan and Molnar 2012).

We are aware of two possible scenarios that could explain the peculiar spin state solutions of asteroids (1482) Sebastiana and (1350) Rosselina: (i) the initial rotational state and shape did not allow them to being captured in the resonance or (ii) the objects were randomly reoriented by non-catastrophic collisions. The timescales of such collisions (given by Eq. (6.6)) are $\tau_{\rm reor} \sim 7.5$ Gyr for asteroid (1482) Sebastiana and $\tau_{\rm reor} \sim 14.7$ Gyr for (1350) Rosselina. This leads to the probability of a collision during the Koronis cluster lifetime (estimated to $\sim$2.5 Gyr, Bottke et al. 2001) $\sim$1/3 for Sebastiana and $\sim$1/6 for Rosselina, respectively, which means that a random collisional reorientation of the spin axis is likely for at least a few of 24 asteroids in the Koronis cluster with known spin state solutions (most of them have $\tau_{\rm reor} \lesssim 20$ Gyr).

Being trapped in the spin-orbital resonance does not necessarily mean that the asteroid is a member of the Koronis family, it rather indicates that its initial orbital position, the rotational state and the shape was favorable for being trapped in the resonance. For example, asteroids (208) Lacrimosa, (277) Elvira, (321) Florentina, (1835) Gajdariya and (3170) Dzhanibekov have expected rotational states but their membership to the Koronis family is not certain (marked by triangles or squares in the Fig. 6.9, see Table 6.6 for reasons why we revised their family membership).

Table 6.2: *List of members of the Flora asteroid family for which the shape models from LI were derived. For each asteroid, the table gives the spin state solution (ecliptic coordinates λ and β of the spin axis and the sidereal rotational period P), proper orbital elements a, e, I, Ω, ω, the diameter D and references.*

Asteroid		λ_1 [deg]	β_1 [deg]	λ_2 [deg]	β_2 [deg]	P [hours]	a [AU]	e	sin$I$ [○]	Ω [○]	ω [○]	D [km]	Reference
8	Flora	335	−5	155	6	12.8667	2.2014	0.1449	0.0971	32.02	−35.51	141	Torppa et al. (2003)
9	Metis	180	22			5.07918	2.3864	0.1272	0.0817	38.75	−42.00	169	Torppa et al. (2003)
43	Ariadne	253	−15			5.76200	2.2034	0.1406	0.0706	32.67	−35.57	66	Kaasalainen et al. (2002b)
352	Gisela	205	−26	23	−20	7.48008	2.1941	0.1367	0.0748	32.30	−35.10	20	this work
364	Isara	281	48	88	45	9.157517	2.2208	0.1586	0.0965	32.71	−36.67	35	this work
376	Geometria	239	45	63	53	7.71098	2.2886	0.1712	0.1064	34.74	−39.66	35	this work
540	Rosamunde	302	80	126	62	9.347792	2.2189	0.1457	0.1042	32.43	−36.05	20	this work
553	Kundry	198	71	−2	64	12.602470	2.2308	0.1273	0.0831	33.31	−35.92	10	this work
685	Hermia	197	87	29	79	50.3869	2.2359	0.1447	0.0788	33.50	−36.74	11	this work
800	Kressmannia	345	37	172	34	4.46096	2.1927	0.1399	0.0750	32.24	−35.18	15	this work
823	Sisigambis	86	74			146.584271	2.2213	0.1388	0.0756	33.16	−36.04	17	this work
915	Cosette	350	56	189	61	4.46974	2.2277	0.1348	0.0898	33.07	−36.02	12	Ďurech et al. (2009)
1056	Azalea	242	61	49	48	15.02758	2.2300	0.1230	0.0795	33.32	−35.81	13	this work
1185	Nikko	359	34			3.786149	2.2375	0.1283	0.0883	33.41	−36.15	11	this work
1188	Gothlandia	133	−84	335	−81	3.49182	2.1907	0.1400	0.0769	32.15	−35.09	12	this work
1249	Rutherfordia	204	72	31	74	18.2183	2.2243	0.1288	0.0943	32.83	−35.68	12	this work
1307	Cimmeria	240	71	90	70	2.820723	2.2505	0.1212	0.0805	34.00	−36.43	10	this work
1446	Sillanpaa	123	82	287	64	9.658551	2.2457	0.1366	0.0834	33.78	−36.80	9	this work
1514	Ricouxa	251	75	68	69	10.4247	2.2404	0.1467	0.0715	33.87	−37.08	7	this work
1518	Rovaniemi	62	60	265	45	5.25047	2.2255	0.1558	0.1061	32.61	−36.64	9	this work
1527	Malmquista		68			14.059127	2.2274	0.1426	0.0855	33.16	−36.34	10	this work
1619	Ueta		36			2.717943	2.2411	0.1497	0.0919	33.46	−37.05	10	this work
1682	Karel	232	32	51	41	3.37485	2.2388	0.1405	0.0757	33.74	−36.72	7	this work
1703	Barry	46	−76	222	−71	107.045310	2.2148	0.1121	0.0662	33.08	−35.04	9	this work
1785	Wurm	11	57	192	47	3.26934	2.2359	0.1207	0.0753	33.61	−35.95	6	this work
2094	Magnitka	107	57	272	48	6.11219	2.2323	0.1470	0.0956	33.08	−36.63	13	this work
2112	Ulyanov	151	61	331	61	3.04071	2.2547	0.1234	0.0708	34.38	−36.73	7	this work
2510	Shandong	256	27	71	27	5.94639	2.2531	0.1502	0.0760	34.25	−37.65	9	this work
7043	Godart	73	61	231	72	8.451782	2.2447	0.1475	0.1069	33.21	−36.95	6	this work
7360	Moberg		−24			4.585340	2.2510	0.1369	0.1003	33.57	−36.84	8	this work
31383	–	110	−74	279	−63	4.16818	2.1853	0.1243	0.0793	31.89	−34.45	4	this work

Table 6.3: *List of members of the Eunomia asteroid family for which the shape models from LI were derived. For each asteroid, the table gives the spin state solution (ecliptic coordinates λ and β of the spin axis and the sidereal rotational period P), proper orbital elements a, e, I, Ω, ω, the diameter D and references.*

Asteroid	λ_1 [deg]	β_1 [deg]	λ_2 [deg]	β_2 [deg]	P [hours]	a [AU]	e	sin$I$ [o]	Ω [o]	ω [o]	D [km]	Reference
15 Eunomia	363	−67			6.08275	2.6437	0.1486	0.2266	42.50	−51.80	255	Kaasalainen et al. (2002b)
85 Io	95	−65			6.87478	2.6537	0.1514	0.2187	43.68	−52.88	161	Ďurech et al. (2011)
390 Alma	54	−48	263	−73	3.74117	2.6517	0.1723	0.2223	43.36	−54.27	24	this work
812 Adele	301	44	154	69	5.85746	2.6594	0.1359	0.2225	43.40	−51.94	15	this work
966 Muschi	282	−71	101	−65	5.355284	2.7193	0.1523	0.2264	45.35	−56.22	31	this work
1333 Cevenola	8	−79	201	−40	4.87933	2.6336	0.1537	0.2329	41.54	−51.36	16	this work
1495 Helsinki	356	−33			5.33131	2.6392	0.1373	0.2234	42.66	−50.96	18	this work
1503 Kuopio	23	−60			9.95861	2.6263	0.1448	0.2241	42.22	−50.75	18	this work
1554 Yugoslavia	281	−34	78	−64	3.88766	2.6194	0.1568	0.2237	42.16	−51.27	12	this work
1927 Suvanto	90	39	277	6	8.16150	2.6497	0.1767	0.2323	42.18	−54.04	14	this work
2384 Schulhof	194	−57	46	−36	3.29367	2.6099	0.1622	0.2304	41.29	−50.89	13	this work
3017 Petrovic		−71			4.080366	2.6074	0.1568	0.2231	41.92	−50.67	13	this work
4399 Ashizuri	268	−48	42	−59	2.830301	2.5759	0.1514	0.2244	41.46	−48.71	9	this work
8132 Vitginzburg	33	−66	193	−48	7.27529	2.6263	0.1347	0.2270	41.89	−49.99	12	this work

Table 6.4: *List of members of the Koronis asteroid family for which the shape models from LI were derived. The table also gives the spin state solution (ecliptic coordinates λ and β of the spin axis and the sidereal rotational period P), proper orbital elements a, e, I, Ω, ω, the diameter D and references.*

Asteroid	λ_1 [deg]	β_1 [deg]	λ_2 [deg]	β_2 [deg]	P [hours]	a [AU]	e	sin$I$ [o]	Ω [o]	ω [o]	D [km]	Reference
158 Koronis	225	−70	30	−64	14.2057	2.8687	0.0452	0.0375	71.01	−65.57	34	this work
	220	−68	35	−65	14.20569							Slivan et al. (2003)
167 Urda	249	−68	107	−69	13.06133	2.8535	0.0429	0.0371	69.74	−64.46	44	this work
	225	−73	40	−75	13.06135							Slivan et al. (2003)
208 Lacrimosa	170	−68	350	−71	14.076919	2.8929	0.0450	0,0372	73.14	−67.25	41	Slivan et al. (2003)
243 Ida	263	−67			4.633632	2.8616	0.0456	0.0364	74.35	−65.11	32	[1]
263 Dresda	105	76	285	80	16.81387	2.8865	0.0420	0.0372	73.39	−66.70	23	Slivan et al. (2009)
277 Elvira	121	−84			29.69219	2.8856	0.0528	0.0373	72.62	−67.06	27	this work
	50	−80	244	−81	29.69218							Slivan et al. (2009)
311 Claudia	214	43	30	40	7.5314	2.8976	0.0406	0.0372	73.68	−67.42	24	this work
	209	48	24	48	7.53139							Slivan et al. (2003)
321 Florentina	264	−61	93	−60	2.870866	2.8856	0.0459	0.0380	72.53	−66.76	27	this work
	264	−63	91	−60	2.870866							Slivan et al. (2003)
462 Eriphyla	108	35	294	34	8.65890	2.8737	0.0501	0.0362	73.88	−66.12	36	Slivan et al. (2009)
534 Nassovia	66	41	252	42	9.46889	2.8842	0.0529	0.0369	72.50	−66.97	33	this work
	58	50	244	50	9.46896							Slivan et al. (2003)
720 Bohlinia	239	40	33	52	8.91861	2.8873	0.5008	0.0359	72.80	−67.11	34	this work
	230	41	40	43	8.91862							Slivan et al. (2003)
832 Karin	242	46	59	44	18.35123	2.8644	0.0439	0.0369	70.64	−65.24	17	this work
	230	42	52	42	18.352							Slivan and Molnar (2012)
1223 Neckar	252	28	69	30	7.82401	2.8695	0.0436	0.0371	71.07	−65.57	28	this work
	259	41	73	40	7.82124							Slivan et al. (2003)
1289 Kutaïssi	158	−79	338	−74	3.624174	2.8605	0.0514	0.0366	74.39	−65.26	27	Slivan et al. (2003)
1350 Rosselia	166	−72			8.14011	2.8580	0.0516	0.0390	70.13	−65.07	23	this work
1389 Onnie	183	−75	0	−79	23.0447	2.8661	0.0435	0.0373	70.76	−65.33	12	this work
1423 Jose	78	−83			12.31269	2.8602	0.0448	0.0370	70.29	−64.98	20	this work
1482 Sebastiana	262	−68	91	−67	10.48965	2.8723	0.0487	0.0347	71.44	−65.99	16	this work
1618 Dawn		−58			43.219	2.8688	0.0459	0.0365	71.05	−65.61	17	this work
1635 Bohrmann	5	−38	185	−36	5.864273	2.8534	0.0448	0.0371	69.75	−64.51	16	this work
1742 Schaifers	57	52	247	68	8.53270	2.8892	0.0588	0.0358	73.07	−67.62	20	this work
1835 Gajdariya	32	72	202	70	6.33768	2.8331	0.0519	0.0366	69.47	−63.42	13	this work
3170 Dzhanibekov	216	62	30	63	6.0717	2.9291	0.0975	0.0347	77.79	−73.36	12	this work
4507 1990 FV	136.9	50	307	51	6.579323	2.8689	0.0454	0.0366	71.05	−65.60	12	this work

[1]The solution of asteroid (243) Ida is based on radar observations and photometric data (Davies et al. 1994; Binzel et al. 1993)

Table 6.5: *List of members of the Eos asteroid family for which the shape models from LI were derived. For each asteroid, the table gives the spin state solution (ecliptic coordinates λ and β of the spin axis and the sidereal rotational period P), proper orbital elements a, e, I, Ω, ω, the diameter D and references.*

Asteroid	λ_1 [deg]	β_1 [deg]	λ_2 [deg]	β_2 [deg]	P [hours]	a [AU]	e	sin$I$ [○]	Ω [○]	ω [○]	D [km]	Reference
573 Recha	74	−24	252	−48	7.165861	3.0138	0.0794	0.1790	73.06	−72.09	48	this work
590 Tomyris	273	−47	120	−46	5.552478	3.0006	0.0818	0.1733	72.37	−71.77	40	this work
669 Kypria	31	40	190	50	14.27889	3.0114	0.0765	0.1836	71.90	−71.41	32	this work
807 Ceraskia	325	23	132	26	7.373901	3.0185	0.0851	0.1797	73.63	−72.84	26	this work
1087 Arabis	334	−7	155	12	5.795005	3.0150	0.0802	0.1704	74.73	−72.84	32	this work
1148 Rarahu	148	−9	322	−9	6.544489	3.0161	0.0932	0.1725	74.71	−73.89	33	this work
1207 Ostenia	310	−77	124	−51	9.07130	3.0207	0.0738	0.1768	74.31	−72.31	23	this work
1286 Banachiewicza	222	59	61	44	8.63043	3.0223	0.0756	0.1757	74.77	−72.61	23	this work
1291 Phryne	106	35	277	59	5.584137	3.0130	0.0648	0.1701	74.23	−71.66	27	this work
1339 Desagneauxa		67			9.375104	3.0211	0.0670	0.1707	75.28	−72.31	26	this work
1353 Maartje	270	74	94	58	22.992610	3.0120	0.0734	0.1693	74.41	−72.17	42	this work
1388 Aphrodite		71			11.943793	3.0189	0.0747	0.1809	73.32	−71.99	22	this work
1464 Armisticia	195	−52	38	−69	7.466992	3.0035	0.0776	0.1821	71.20	−71.06	23	this work
1826 Miller		14			26.184845	2.9971	0.0800	0.1788	71.01	−71.02	20	this work
2957 Tatsuo	88	57	246	37	6.820432	3.0221	0.0748	0.1694	75.74	−73.04	26	this work
3896 Pordenone	355	−26	180	−46	4.003659	3.0057	0.0783	0.1828	71.34	−71.21	20	this work
5281 Lindstrom	238	−72	84	−81	9.25112	3.0125	0.0817	0.1755	73.48	−72.46	–	this work
19848 Yeungchuchiu	66	−70	190	−67	3.451035	3.0075	0.0573	0.1759	72.54	−70.44	16	this work

Table 6.6: *List of asteroids for which the HCM method suggested a membership to families Flora, Eunomia, Koronis or Eos, but other methods for the family membership determination identified them as interlopers or borderline cases. The table gives the name of the asteroid, the family membership according the HCM method, if it is an interloper or a bordeline case and the reason why. Peculiar SFD means a size frequency distribution that is incompatible with the SFD typically created by collisions or cratering events. Quantity v_{cutoff} corresponds to the cutoff value of the HCM method.*

Asteroid	HCM	Status	Reason
9 Metis	Flora	Interloper	Very far from the border on (a,H) plot, peculiar SFD
43 Ariadne	Flora	Interloper	Asociated at $v_{\mathrm{cutoff}} = 70$ m/s, peculiar SFD
352 Gisela	Flora	Borderline	Asociated at $v_{\mathrm{cutoff}} = 70$ m/s, big object
376 Geometria	Flora	Interloper	Far from (a,H), peculiar SFD
800 Kressmannia	Flora	Borderline	Asociated at $v_{\mathrm{cutoff}} = 70$ m/s, lower albedo
1703 Barry	Flora	Borderline	Asociated at $v_{\mathrm{cutoff}} = 70$ m/s
7360 Moberg	Flora	Borderline	Close to the (a,H) border, redder
85 Io	Eunomia	Interloper	Behind the (a,H) border, peculiar SFD, incompatible albedo
390 Alma	Eunomia	Borderline	Relatively big, borderline albedo
966 Muschi	Eunomia	Interloper	Far on (a,H), big
208 Lacrimosa	Koronis	Interloper	Far on (a,H), peculiar SFD
277 Elvira	Koronis	Borderline	Close to the (a,H) border, relatively big
321 Florentina	Koronis	Borderline	Close to the (a,H) border, relatively big
1835 Gajdariya	Koronis	Interloper	Close to the (a,H) border, incompatible albedo
3170 Dzhanibekov	Koronis	Interloper	Behind the (a,H) border, incompatible albedo
590 Tomyris	Eos	Borderline	Behind the (a,H) border

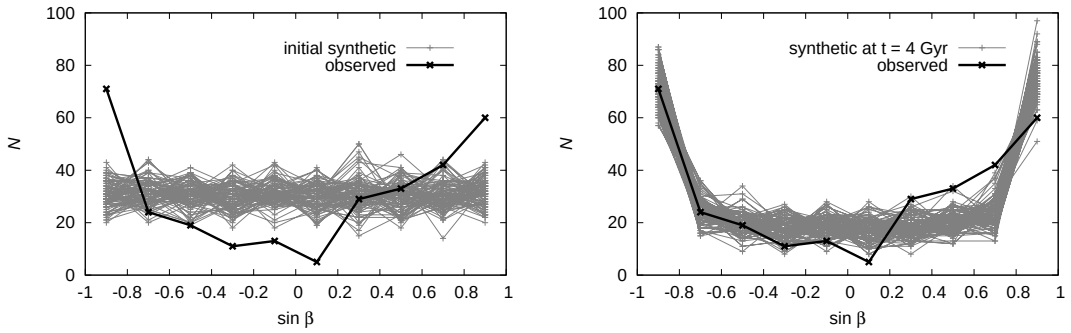

Figure 6.10: *Left panel: The distribution of the de-biased ecliptic latitudes β for the observed asteroids (thick line) and 100 synthetic samples (generated with a different random seed) at time $t = 0$ (thin lines). Right panel: synthetic latitude distributions at time $t = 4\,\mathrm{Gyr}$ (thin lines), evolved by the YORP effect ($c_{\mathrm{YORP}} = 0.20$), collisions, mass shedding and spin-orbital resonances. We also applied an observational bias to it.*

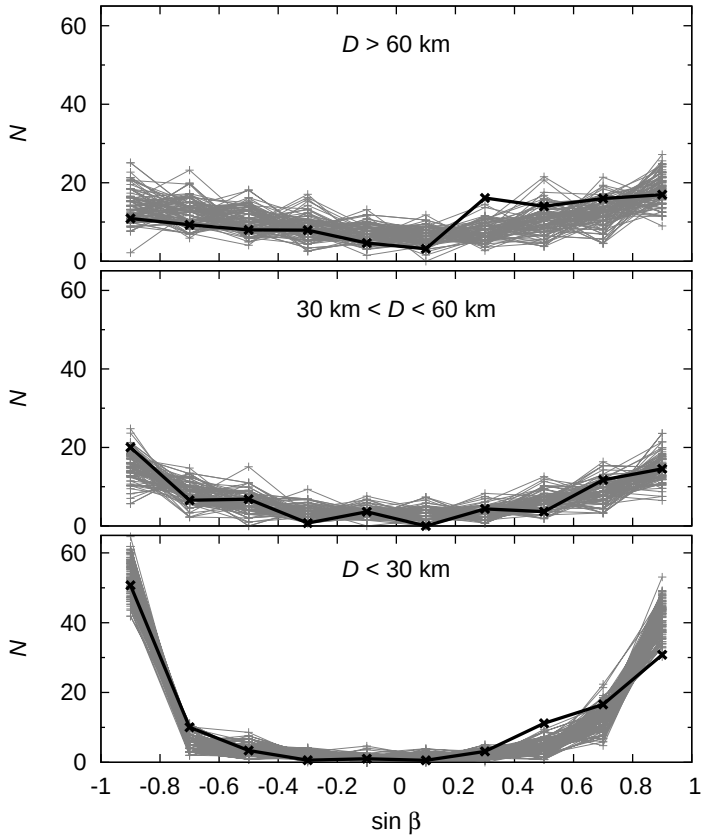

Figure 6.11: *Synthetic latitude distributions at $t = 4$ Gyr and $c_{\mathrm{YORP}} = 0.20$ for three different size ranges: $D > 60\,\mathrm{km}$ (top), $30\,\mathrm{km} < D < 60\,\mathrm{km}$ (middle) and $D < 30\,\mathrm{km}$ (bottom). The synthetic distributions are plotted by thin gray lines while the de-biased observed distributions by thick black lines.*

6.2 Theoretical model of the spin evolution

In order to understand observations of main belt asteroids, namely the de-biased distribution of their ecliptic latitudes β (Fig. 6.3b), we constructed a simple model for the spin evolution that contains the following processes: (i) the YORP effect, i.e., torques arising from the emission of thermal radiation, (ii) random reorientations induced by non-catastrophic collisions, (iii) oscillations caused by gravitational torques and spin-orbital resonances, and also (iv) mass shedding after a critical rotational frequency is reached.

Because we studied a large statistical sample of asteroids, the effect on the overall latitude distribution of pole directions caused by other processes (gravitational torques by the Sun, damping, or tumbling) was assumed to be only minor (although individual asteroids may be substantially affected by these processes).

De-biased observed latitude distribution of pole directions of MBAs represents fingerprints of the past evolution of this population. Direct comparison between the de-biased observed asteroid properties and predictions of theoretical models can validate/exclude some of the current theories for the asteroid dynamical evolution or constrain specific free parameters.

Our sample of physical parameters for $\sim$ 300 asteroids consisted of models from DAMIT ($\sim$ 200, December 2012), and models derived in Hanuš et al. (2013). This means that the orbits and sizes correspond to real asteroids. The model for spin evolution was similar to that of Brož et al. (2011), where it was used for studies of the long-term evolution of asteroid families. We assumed the following relations for the rate of the angular velocity ω ($\omega = 2\pi/P$) and the obliquity ϵ (Euler equations)

$$\frac{\mathrm{d}\omega}{\mathrm{d}t} = c f_i(\epsilon)\,, \qquad i = 1 \ldots 200\,, \tag{6.2}$$

$$\frac{\mathrm{d}\epsilon}{\mathrm{d}t} = \frac{c g_i(\epsilon)}{\omega}\,, \tag{6.3}$$

where f- and g-functions were given by Čapek and Vokrouhlický (2004) for a set of 200 shapes with the effective radius $R_0 = 1\,\mathrm{km}$, the bulk density $\rho_0 = 2500\,\mathrm{kg/m^3}$, located on a circular orbit with semi-major axis $a_0 = 2.5\,\mathrm{AU}$. We assigned one of the artificial shapes (denoted by the index i) randomly to each individual asteroid[5]. We had only to scale the f- and g-functions by a factor

$$c = c_{\mathrm{YORP}} \left(\frac{a}{a_0}\right)^{-2} \left(\frac{R}{R_0}\right)^{-2} \left(\frac{\rho_{\mathrm{bulk}}}{\rho_0}\right)^{-1}\,, \tag{6.4}$$

where a, R, ρ_{bulk} are the semi-major axis, the radius, and the density of the simulated body, respectively, and c_{YORP} is a *free* scaling parameter reflecting our uncertainty in the shape models and the magnitude of the YORP torque, which is dependent on small-sized surface features (even boulders Statler 2009) and other

[5]We did not use the convex-hull shapes derived in this work for two reasons: (i) the two samples of shapes are believed to be statistically equivalent and it is thus not necessary to compute the YORP torques again; (ii) the YORP effect seems sensitive to small-scale surface structure (Scheeres and Mirrahimi 2007) which cannot be caught by our shape model. Nevertheless, the YORP torque remains of the same order, so the random assignment of shapes seems reasonable.

simplifications in the modeling of the YORP torque. Because the values of f's and g's were computed for only a limited set of obliquities (with a step $\Delta\epsilon = 30°$) we used interpolation by Hermite polynomials (Hill 1982) of the data in Čapek and Vokrouhlický (2004) to obtain a smooth analytical functions for $f_i(\epsilon)$ and $g_i(\epsilon)$.

When the angular velocity approached a critical value (i.e., the gravity was equal to the centrifugal force)

$$\omega_{\rm crit} = \sqrt{\frac{4}{3}\pi G \rho_{\rm bulk}}\,, \tag{6.5}$$

we assumed a mass shedding event. We kept the orientation of the spin axis and the sense of rotation but reset the orbital period $P = 2\pi/\omega$ to a random value from the interval $(P_1, P_2) = (2.5, 9)$ hours (the choice of this period interval is justified later). We also altered the assigned shape since any change of shape can produce a different YORP effect. We did not change the mass, however.

The differential equations (6.2) and (6.3) were integrated numerically by a simple Euler integrator. The usual time step was $\Delta t = 1000\,{\rm yr}$. The time scale of the spin axis evolution for small bodies ($D \simeq 10\,{\rm km}$, $c_{\rm YORP} = 0.3$) is $\tau_{\rm YORP} \simeq 500\,{\rm Myr}$. After $\simeq 3$ times $\tau_{\rm YORP}$ most of these bodies have spin axes perpendicular to the ecliptic.

We also included a Monte-Carlo model for spin axis reorientations caused by collisions.[6] We used an estimate of the time scale by Farinella et al. (1998)

$$\tau_{\rm reor} = B \left(\frac{\omega}{\omega_0}\right)^{\beta_1} \left(\frac{D}{D_0}\right)^{\beta_2}\,, \tag{6.6}$$

where $B = 84.5\,{\rm kyr}$, $\beta_1 = 5/6$, $\beta_2 = 4/3$, $D_0 = 2\,{\rm m}$ and ω_0 corresponds to period $P = 5$ hours. These values are characteristic for the main belt. After a collision, we reset the spin axis periods to random values, using the interval $(P_1', P_2') = (2.5, 9)$ hours for the period. Since the time scale is $\tau_{\rm reor} \simeq 3\,{\rm Gyr}$ for the smallest ($D \simeq 5\,{\rm km}$) bodies, reorientations are only of minor importance. However, note that the probability of the reorientation is enhanced when the YORP effect drives the angular velocity ω close to zero.

There were several free parameters in our model: the $c_{\rm YORP}$ parameter, the thermal conductivity K, the bulk density $\rho_{\rm bulk}$, the initial distribution of β and the initial distribution of ω.

Our aim was to start with a simple β- and ω-distribution, perform the simulation for overall time of 4 Gyr, and then compare the resulting synthetic to de-biased observed latitude distributions. We applied an observational bias derived in Section 6.1 to the synthetic distribution.

We partly accounted for spin-orbital resonances acting on prograde asteroids by adding a sinusoidal oscillations to β with a random phase and an amplitude $\simeq 40°$, which are typically induced by resonances. This procedure naturally decreased the right-most bin ($\sin\beta = (0.8, 1)$) of the synthetic distribution and increased the next bin ($\sin\beta = (0.6, 0.8)$).

[6] Collisional disruptions are not important, since we are only interested in the steady state. We can imagine that whenever an asteroid from our sample is disrupted, another one with a randomly oriented spin axis is created by a disruption of a larger body.

We started with reasonable parameters of the thermal conductivity $K = 10^{-2}\,\mathrm{W/K/m}$, the bulk density $\rho_{\mathrm{bulk}} = 2500\,\mathrm{kg/m^3}$, a Maxwellian distribution of ω, a uniform distribution of $\sin\beta$ (i.e., an isotropic distribution of spin vectors). We tested the following values of the parameter c_{YORP}: 0.01, 0.05, 0.1, 0.2, 0.3, 0.4, 0.5, 0.6, 0.8. Values of $c_{\mathrm{YORP}} \gtrsim 1$ were already recognized as being unrealistic. For each value of c_{YORP}, we ran 100 simulations with different random seeds (to generate the isotropic distribution of spin vectors).

The resulting latitude distributions for $c_{\mathrm{YORP}} = 0.20$ are shown in Figures 6.10 and 6.11.

From these it can be seen that: (i) the de-biased observed distribution of β for small asteroids seems compatible with our model; the YORP effect is capable of creating such an uneven distribution and (ii) there is a discrepancy for large asteroids (especially in bins $\sin\beta \in (0.2, 0.6)$), which can be explained as a preference for prograde rotators in the primordial population (see Davis et al. 1989; Johansen and Lacerda 2010).

We also tested the sensitivity of our results with respect to the free parameters. The thermal conductivity did not seem important (we tested $K = 10^{-3}\,\mathrm{W/K/m}$). A simulation with $\rho = 1300\,\mathrm{kg/m^3}$, and a uniform distribution of orbital periods $P \propto 1/\omega$ produced almost the same resulting latitude distribution. There is only a weak dependence of our results on the period ranges that we used for resetting the orbital period after a mass-shedding event (P_1, P_2) and collision (P_1', P_2'). As would be expected, the values P_1, P_2, P_1', P_2' significantly affect the period distribution.

As described above, for each value of c_{YORP}, we ran 100 simulations with different random seeds. As initial conditions, we assumed a Maxwellian distribution of angular velocities ω and isotropically distributed spin vectors. The last assumption is not fulfilled for larger asteroids ($D > 60$ km), because this population has an excess of prograde rotators (see Fig. 6.3b), which is believed to be of a primordial origin. The second reason why we rejected asteroids with $D > 60$ km from the physical interpretation of our simulation is that their evolution is rather slow compared to the simulation time span.

The spin states of our synthetic asteroids are evolving during the simulation. At each time t of the simulation, we can construct a latitude distribution of the pole directions with latitude values split into 10 bins with a variable width corresponding to constant surface on the celestial sphere. Because we used ecliptic coordinates with the longitude λ and the latitude β, bins were equidistant in $\sin\beta$. In order to describe the temporal evolution of the simulated latitude distributions, we computed a χ^2 metric between the simulated and the de-biased observed latitude distributions of asteroids with diameters $D < 60$ km. For each time t within the simulation run j ($j = 1..100$), the corresponding chi-square value χ^2_{tj} is defined by

$$\chi^2_{tj} \equiv \sum_i \frac{(S_{tji} - O_i)^2}{\sigma^2_{tji}}, \tag{6.7}$$

where S_{tji} denotes the number of synthetic bodies with latitudes in bin i, O_i the number of observed latitudes in bin i and $\sigma_{tji} \equiv \sqrt{S_{tji} + O_i}$ corresponds to the uncertainty estimate.

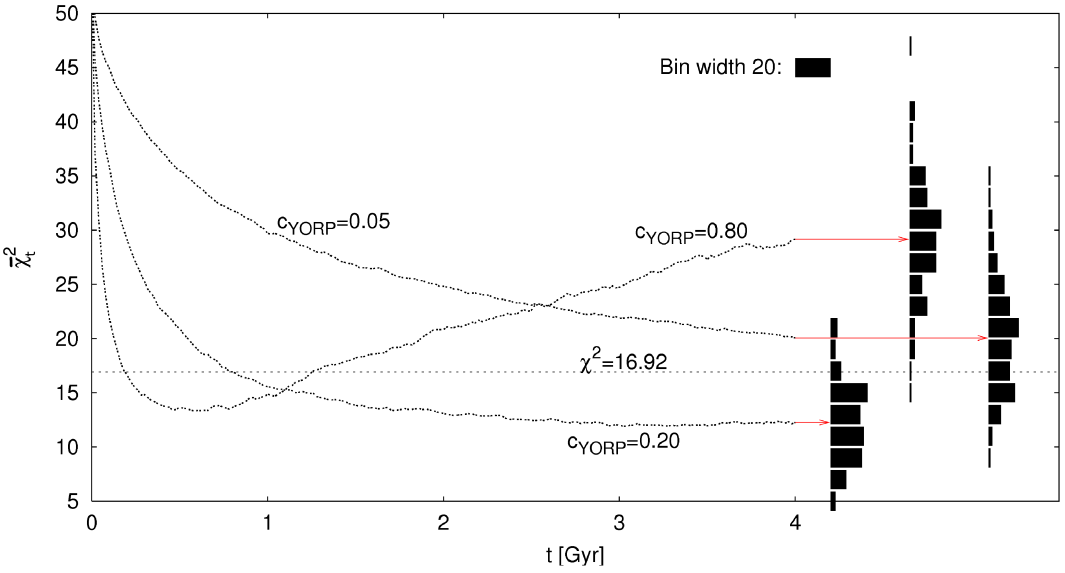

Figure 6.12: *Temporal evolution of the χ^2 which corresponds to the difference between the simulated latitude distributions, averaged over all 100 runs, and the debiased observed latitude distribution (i.e., $\bar{\chi}^2_t$) for three different values of parameter c_{YORP} = 0.05, 0.20 and 0.80 (we performed a chi-square test). Vertical histograms on the right-hand side represent the distributions of χ^2_{tj} at time $t = 4$ Gy for all 100 runs. Dotted line: the statistically significant probability value of 5%, i.e. $\chi^2 = 16.92$.*

In Fig. 6.12, we show the temporal evolution of the *average* chi-square $\bar{\chi}^2_t = \sum_{j=1}^{100} \chi^2_{tj}/100$ in course of our numerical simulations for different c_{YORP} values. We can distinguish three basic cases of the temporal evolution:

- In the case when the YORP effect is weak ($c_{\mathrm{YORP}} \lesssim 0.1$), the synthetic latitude distribution is evolving only slowly and is never similar to the observed latitude distribution, even at the end of the simulation, because χ^2 is still large (for $N = 9$, a statistically significant probability value[7] of 5% corresponds to $\chi^2 = 16.92$).

- A steady state (i.e., the state when the synthetic latitude distribution does not significantly evolve in time, and thus the $\bar{\chi}^2_t$ is approximately constant) is reached only for c_{YORP} values close to 0.2.

- For values $c_{\mathrm{YORP}} \gtrsim 0.3$, the synthetic latitude distribution is evolving faster and, at a certain time, is most similar to the observed latitude distribution (i.e., the minimum of $\bar{\chi}^2_t$). After that, the $\bar{\chi}^2_t$ is growing, because the YORP is significantly evolving also larger asteroids, and thus the bins with low latitudes are depopulated more than is observed.

Vertical histograms on the right-hand side of the Fig 6.12 represent the distributions of χ^2_{tj} at the time $t = 4$ Gy for all 100 runs. The average chi-square $\bar{\chi}^2_t$ of the model with $c_{\mathrm{YORP}} = 0.05$ is substantially higher than 16.92 and so this model

[7] Our latitude distributions consist of ten bins, the degree of freedom is then $N = 9$.

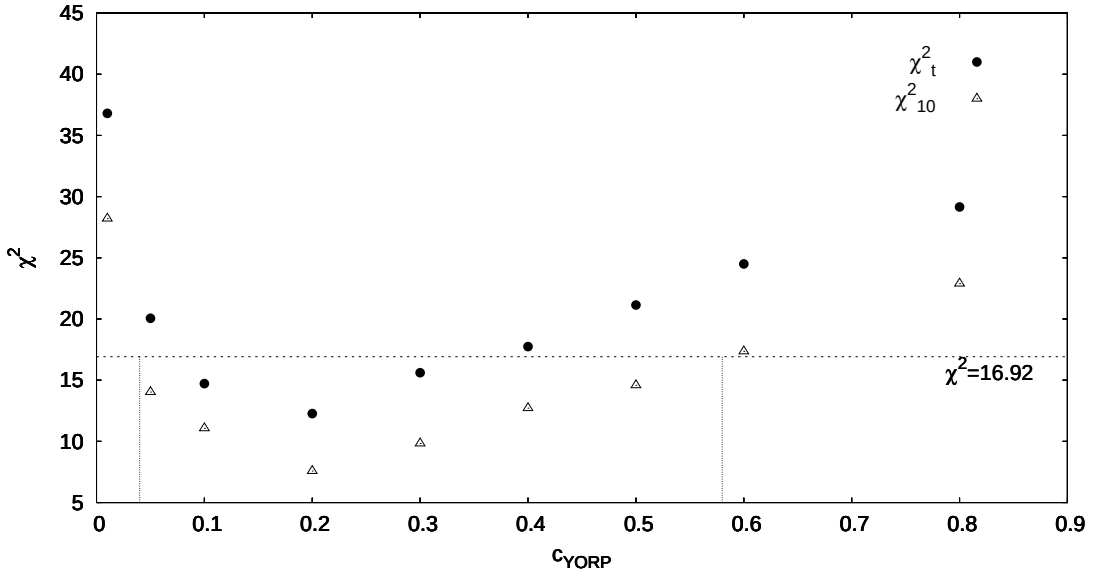

Figure 6.13: *Dependence of $\bar{\chi}^2_t$ and χ^2_{10} values calculated for the time $t = 4$ Gyr (i.e. the final state of the simulation) on different values of the c_{YORP} parameter. We also plotted the statistically significant probability value of 5% which corresponds to $\chi^2 = 16.92$ and the interval of plausible c_{YORP} values from 0.05 to 0.6.*

can be considered wrong. However, from the distributions of χ^2_{tj} we can see that about 25% of individual runs have χ^2_{tj} lower than 16.92. In order to avoid rejection of those c_{YORP} values which are partially compatible with observations, we should rather use a more representative value of χ^2 than the average $\bar{\chi}^2_t$, namely a value χ^2_{10}, for which 10% runs have lower χ^2_{tj} (see Fig. 6.13). Based on the χ^2_{10}, the most probable values of the c_{YORP} parameter are between 0.05 and 0.6.

Our preferred interpretation of the fact that the optimal c_{YORP} value is much lower than 1 is that small scale features (boulders) tend to decrease the YORP torque. This hypothesis is supported by the independent modeling of Rozitis and Green (2012) who estimated, by including rough surface thermal-infrared beaming effects into their long-term spin evolution model, that the surface roughness is on average responsible for damping the magnitude of the YORP effect typically by 1/2 of the smooth surface predictions. This would correspond to $c_{\mathrm{YORP}} = 0.5$ in our notation. The YORP effect is sensitive to the sizes of the boulders and can vary tens of percent. So, results of Rozitis and Green (2012) are in agreement with our model.

As an important application, let us mention that the constraint for the value of c_{YORP} can be used in simulations of the long-term dynamical evolution of asteroid families. So far, c_{YORP} was used as a free parameter (e.g., in the method presented by Vokrouhlický et al. 2006a). So, constraining c_{YORP} *removes* one free parameter from the simulations and should thus lead to a better determination of the ages of asteroid families.

The de-biased observed β-distribution of small asteroids ($D < 30$ km) cannot be explained by our simulation without accounting the YORP effect.

Chapter 7

Asteroid models application

In Section 5.1, we enlarged the number of asteroids with known shapes and rotational states to ∼500. Such models can help us in understanding the physical processes that take place in the asteroid populations, such as Near Earth Asteroids (NEAs), Main Belt Asteroids (MBAs) or even asteroids in individual families. In Section 6.1, we showed that current distribution of periods and spin axes are the direct result of the evolution of these objects starting with their formation until the present time (several hundreds of Myr to ~ 4 Gyr for the most studied asteroids), where the most prominent processes acting on asteroids are collisions and mass shedding, and the YORP effect. The knowledge of the shape and the rotational state can be used for several other purposes, where we can derive important physical properties of asteroids, e.g.:

- In combination with stellar occultations by asteroids. These events (observed for hundreds of asteroids) give us additional information about the shape (e.g. non-convexities) and can lead to a size estimation with a typical uncertainty of 10% (see Ďurech et al. 2011). We present sizes derived from stellar occultations for eight asteroids in Section 7.1.

- In combination with the adaptive optics (AO) images observed by 8–10m class telescopes. By combining resolved direct AO images of asteroids with the shape models derived by the lightcurve inversion method we infer sizes for 41 asteroids in Section 7.2.

Sizes are important characteristics of asteroids. If a mass estimate is also available, average densities can be computed. All derived models are stored and publicly available in the DAMIT database. Scientists can use our shape models for their research, e.g., for the construction of a thermal model, where the values for geometric albedo, size and surface properties can be determined.

7.1 Combination with star occultations by asteroids

From observations of star occultations by asteroids, we can reconstruct asteroid's projected silhouettes. These silhouettes can be then compared with the predicted contours of the convex shape models and used for the asteroid size determination

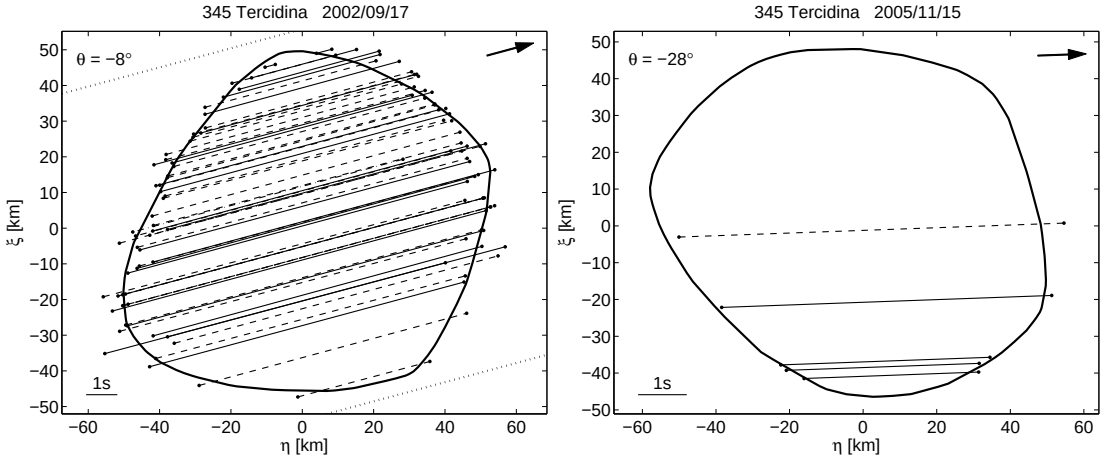

Figure 7.1: *Two observations of star occultations by asteroid (345) Tercidina. The solid contour corresponds to a scaled projected silhouette of the shape model with the pole* (346°,–55°)*, each chord represents one occultation observation (solid lines are CCD, video or photoelectric observations, dashed lines visual observations, and dotted lines negative observations). Each plot contains also the time scale (lower left corner), the latitude of the sub-Earth point θ for the time of occultation (upper left corner) and the direction of the relative velocity (the arrow in the upper right corner). East points to the left and north up. From Hanuš et al. (2013).*

by scaling the shape models to fit the occultation chords. The size of the model is usually represented by a volume-equivalent diameter $D_{\rm eq}$, which is a diameter of a sphere of the same volume as the scaled convex model. A detailed description of the procedure of scaling the convex shape model by using stellar occultations can be found in Ďurech et al. (2011). The typical relative uncertainty of the asteroid sizes derived by this method is $\sim 10\%$.

Reasonable amount of stellar occultations were available for eight asteroids we derived in Section 5.1. By using same methods as in Ďurech et al. (2011), we rejected mirror solutions for asteroids (10) Hygiea, (302) Clarissa, (345) Tercidina and (578) Happelia, and also determined volume-equivalent diameters for all eight asteroids (Table 7.1, the fifth column). An example of two different stellar occultations for asteroid (345) Tercidina is plotted in Fig. 7.1. In Table 7.1, we also included diameters $D_{\rm IRAS}$ derived from the IRAS infrared measurements (Tedesco et al. 2004) and diameters $D_{\rm WISE}$ based on WISE infrared data (Masiero et al. 2011). In most cases, our sizes were, within the uncertainties, in an agreement with diameters based on infrared data, the only exception was asteroid (10) Hygiea, where we got three different values for the size. The large dispersion in size is probably caused by the selection effect of the infrared surveys due to the observing geometry (will be discussed in more details in Section 7.2). This effect can result in an over- or underestimated size determination of more than about 30%. Preferred pole solutions by the stellar occultations are stressed by bold font in Table 5.1.

Table 7.1: *List of asteroids for which we derived equivalent diameters by comparing their shape models with stellar occultations. For each asteroid, the table gives the ecliptic coordinates λ and β of the spin axis, sidereal rotational period P, volume-equivalent diameter D_{eq} of the scaled model, diameters D_{IRAS} and D_{WISE} derived from the IRAS (Tedesco et al. 2004) and WISE (Masiero et al. 2011) infrared measurements, and references to convex models. In all cases, only one pole solution was in agreement with the stellar occultation data.*

Asteroid	λ [deg]	β [deg]	P [hours]	D_{eq} [km]	D_{IRAS} [km]	D_{WISE} [km]	Reference
10 Hygiea	122	−44	27.6591	351±27	407±7	453±19	Hanuš et al. (2011)
152 Atala	347	47	6.24472	65±8	–	61±1	Ďurech et al. (2009)
302 Clarissa	28	−72	14.47670	43±4	39±3	–	Hanuš et al. (2011)
345 Tercidina	346	−55	12.37082	96±10	94±5	99±11	Hanuš et al. (2013)
404 Arsinoe	25	57	8.88766	101±5	98±2	99±3	Hanuš et al. (2013)
471 Papagena	223	67	7.11539	137±25	134±5	–	Hanuš et al. (2011)
578 Happelia	338	63	10.06447	70±5	69±2	–	Hanuš et al. (2013)
925 Alphonsina	296	41	7.87754	58±16	54±3	58±5	Hanuš et al. (2011)

7.2 Combination with adaptive optics images

Convex shape models are not scaled in size because we do not possess measurements of asteroid albedos. We usually get two *mirror solutions* (due to the symmetry of the lightcurve inversion method), which differ only in the ecliptic latitude of the pole direction by $\sim 180°$.

By combining resolved direct images of asteroids collected with Adaptive optics (AO) systems with their shape models derived by the lightcurve inversion method, we can infer the sizes of these asteroids. By scaling the shape model to fit the estimated size of the resolved asteroid, we can derive a volume-equivalent diameter D_{eq}. Additionally, we can remove the ambiguity between two possible mirror solutions derived by the lightcurve inversion method. Thanks to the adopted mass values, it is also possible to compute average densities of several asteroids.

We used W.M. Keck AO images (Wizinowich et al. 2000) recorded within a campaign of observation aiming at identifying and studying multiple asteroid systems (Marchis et al. 2006). The data, collected between 2003 and 2010 with near-infrared NIRC-2 camera in H (1.63 μm), FeII (1.64 μm) or K (2.12 μm) filters, reach an angular resolution between 40 and 55 mas. To improve their sharpness and determine the silhouette (two dimensional projection of the shape onto the plane perpendicular to the line connecting the observer and the center of the asteroid), all images were deconvolved using AIDA deconvolution algorithm described in Marchis et al. (2006); Hom et al. (2007).

We gathered quality AO data for 50 main belt asteroids with shape models. In Figure 7.2, we show an example of four adaptive optics images of asteroid (45) Eugenia, where the contours were computed by the AIDA deconvolution algorithm.

We defined the fundamental plane that passes through the center of the asteroid and is perpendicular to the line connecting the observer and the center of the asteroid, and also the coordinate system (ξ, η) on the fundamental plane in the same way as in Ďurech et al. (2011). The coordinate system is centered into

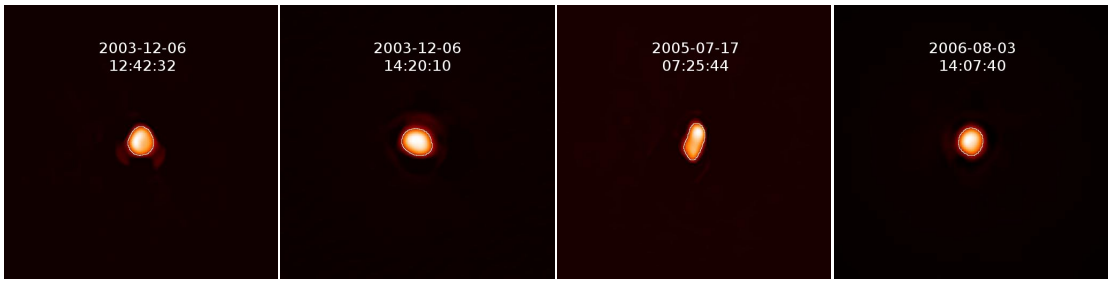

Figure 7.2: *Four adaptive optics images of asteroid (45) Eugenia, contours were computed by the AIDA deconvolution algorithm (Marchis et al. 2006; Hom et al. 2007).*

the center of the AO image. We derived the asteroid silhouette with coordinates $(\xi_j,\, \eta_j)_{\mathrm{AO}}$ directly from the AO observation (see Fig. 7.2). While we knew the distance L of the asteroid in the time of its observation with the AO system and the pixel scale of the image, we could express the contour coordinates directly in kilometers. The distance γ in mas (miliarcseconds) on the AO image correspond to the distance x in kilometers by a relation:

$$x[\mathrm{km}] = \frac{\pi L[\mathrm{km}]}{180 \cdot 10^3 \cdot 3600}\gamma[\mathrm{mas}]. \tag{7.1}$$

The convex hull of projected vertices (only both illuminated by the Sun and visible from the Earth) of the convex polyhedron onto the fundamental plane represent a silhouette of the model given by the coordinates $(\xi_j,\, \eta_j)_{\mathrm{m}}$. The model contour was calculated from the convex shape model orientation at the time of the AO observation. To determine the true size of the model, we minimized the difference between these two silhouettes. In order to compare successfully both contours, we needed to find on the model contour points that correspond to the points defining the AO contour. These points lie on the intersections between the model contour and the lines which goes from the center of the AO contour (i.e., center of the coordinate system) through the points $(\xi_j,\, \eta_j)_{\mathrm{AO}}$ (see Figure 7.3). By this, we created a new model contour with coordinates $(\xi_j,\, \eta_j)_{\mathrm{M}}$.

While the AO silhouette remains fixed in size, the dimension of the model silhouette is parametrized by a scale c. The shift between the centers of the silhouettes is parametrized by an offset $(\xi_0,\, \eta_0)$, which is also optimized (for more details see Ďurech et al. 2011). When we have AO observations of an asteroid from different time, we optimize *one* scale value for all AO and model contours. On the other hand, the offset is different for each pair of contours. We minimize the measure:

$$\chi^2 = \sum_{i=1}^{N} \sum_{j=1}^{n_i} \frac{[(\xi_j, \eta_j)^{(i)}_{\mathrm{AO}} - (\xi_j, \eta_j)^{(i)}_{\mathrm{M}}]^2}{(\sigma^i_j)^2}, \tag{7.2}$$

where N is the number of AO images, n_i the number of points defining the contour of the i-th AO image, $(\xi_j, \eta_j)^{(i)}_{\mathrm{AO}}$ the contour of the $i-th$ AO image, $(\xi_j, \eta_j)^{(i)}_{\mathrm{M}}$ the corresponding i-th model contour and $(\sigma^i_j)^2$ are errors of $(\xi_j, \eta_j)^{(i)}_{\mathrm{AO}}$.

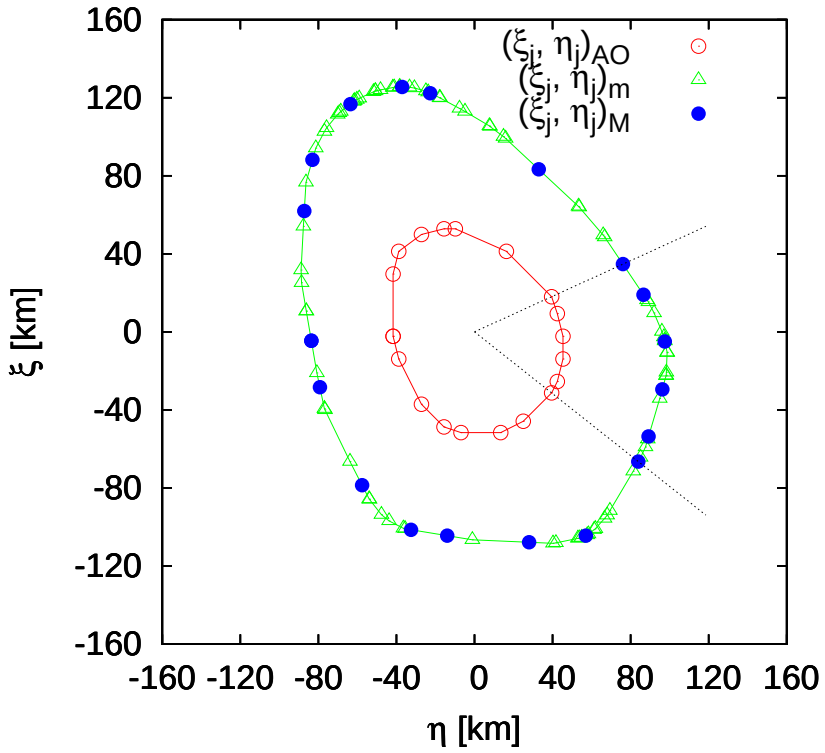

Figure 7.3: *Scaled contour* $(\xi_j, \eta_j)_{\mathrm{AO}}$ *of the disk-resolved image (AO contour) of asteroid (201) Penelope (red open circles connected with lines), unscaled contour* $(\xi_j, \eta_j)_{\mathrm{m}}$ *of the corresponding convex shape model computed for the time of the AO observation (green triangles connected with lines) and intersections* $(\xi_j, \eta_j)_{\mathrm{M}}$ *(blue full circles) between the model contour and the lines which goes from the center of the AO contour through the points* $(\xi_j, \eta_j)_{\mathrm{AO}}$ *(two such lines are displayed by thin dotted lines). East points to the left and north up.*

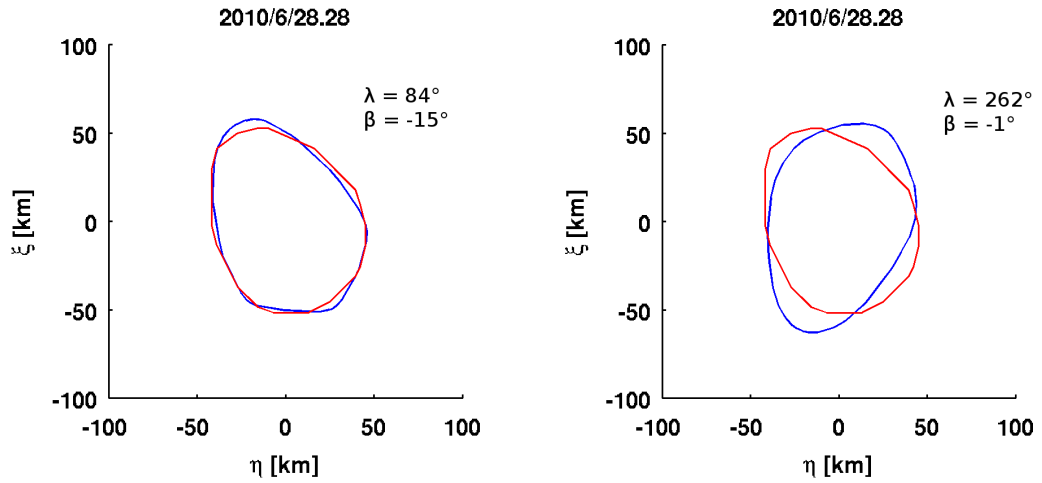

Figure 7.4: *AO contours (red) and scaled silhouettes (blue) of two mirror solutions of asteroid (201) Penelope. The model in the left panel is in agreement with the AO contour, on the other hand, the model in the right panel is clearly incorrect.*

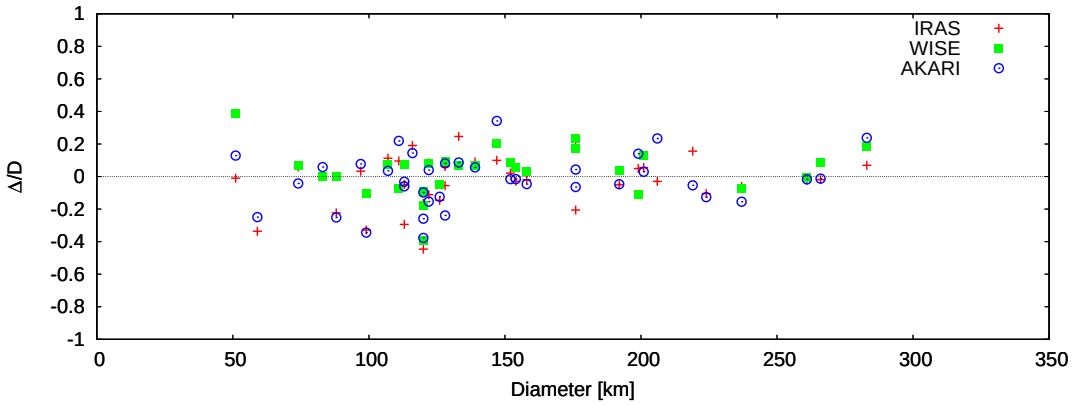

Figure 7.5: *Relative differences between effective diameters derived by IRAS, WISE and AKARI and volume-equivalent diameters based on AO observations.*

The measure (7.2) can be rewritten with parameters c and $(\xi_0, \eta_0)^{(i)}$ as follows:

$$\chi^2 = \sum_{i=1}^{N} \sum_{j=1}^{n_i} \frac{(\xi_{j\mathrm{AO}}^{(i)} - c\,\xi_{j\mathrm{M}}^{(i)} - \xi_0^{(i)})^2 + (\eta_{j\mathrm{AO}}^{(i)} - c\,\eta_{j\mathrm{M}}^{(i)} - \eta_0^{(i)})^2}{(\sigma_j^i)^2}. \qquad (7.3)$$

To find the optimal values of free parameters c and $(\xi_0, \eta_0)^{(i)}$, we optimize the measure (7.3) by a simple least-square minimization method.

According to simulations presented in Marchis et al. (2006), the size uncertainty of the AO contour determined by the AIDA deconvolution is dependent on the size of the image. If the size is between 5 and 12 pixels, the uncertainty is 5-10%, if larger, the uncertainty should be $\sim$ 5%. Most of the resolved asteroids are larger than 10 pixels (the diffraction limit of the Keck 10m telescope corresponds to $\sim$5 pixels in Kp band. The second important source of size uncertainties are

Table 7.2: *List of asteroids for which we removed the convex shape model pole ambiguity by comparing their shape models with images from adaptive optics observations. For each asteroid, the table gives the ecliptic coordinates λ and β of the correct spin axis, sidereal rotational period P, equivalent diameters $D_{\rm eq}$ of the scaled model and references to the convex models.*

Asteroid	λ [deg]	β [deg]	P [hours]	$D_{\rm eq}$ [km]	Reference
37 Fides	270	19	7.33253	122±10	Hanuš et al. (2011)
40 Harmonia	22	31	8.90848	126±10	Hanuš et al. (2011)
42 Isis	107	38	13.58364	97±6	Hanuš et al. (2011)
54 Alexandra	156	13	7.02264	133±8	Warner et al. (2008a)
79 Eurynome	228	30	5.97777	119±8	Hanuš et al. (2013)
80 Sappho	194	−26	14.03087	74±6	Ďurech et al. (2009)
88 Thisbe	72	60	6.04131	224±16	Torppa et al. (2003)
97 Klotho	−1	30	35.2510	83±6	Hanuš et al. (2011)
201 Penelope	262	−1	3.747453	88±6	Torppa et al. (2003)
349 Dembowska	322	18	4.701204	168±18	Torppa et al. (2003)

the convex model imperfections, which can be ∼5%. The overall size uncertainty is then ∼ 10% for most studied asteroids.

We computed the volume of a scaled convex polyhedron (with equations from Dobrovolskis 1996) and used it to determine the volume-equivalent diameters $D_{\rm eq}$. We derived volume-equivalent diameters for 41 out of 50 asteroids from our sample (see Table 7.3, where we also list the effective diameters $D_{\rm IRAS}$, $D_{\rm WISE}$, $D_{\rm AKARI}$ derived by IRAS, WISE and AKARI, respectively, and the volume-equivalent diameters $D_{\rm occ}$ derived by scaling the convex shape models to the stellar occultation measurements Ďurech et al. 2011)) with a typical size uncertainty of ∼ 10%. We used all available AO observations for each asteroid simultaneously in the size optimization process. We removed the pole ambiguity for 10 asteroids (see Table 7.2, where we list the correct pole solutions and volume-equivalent diameters), an example for asteroid (201) Penelope is shown in Figure 7.4. For all asteroids, for which their sizes were derived also from the stellar occultation observations, we got consistent sizes based on fitting the AO images.

For 9 out of 50 studied asteroids, we got a poor fit of the convex silhouette and the AO contour. While the AO contours are of a reasonable quality, the problem is probably caused by the convex model imperfections. The models need to be revised by using more data in the modeling or we have to introduce some non-convex features in to the size optimization. However, the possibility of some systematics in the AO contours cannot be with certainty excluded.

We computed the relative differences between effective diameters derived by IRAS (Tedesco et al. 2002), WISE (Masiero et al. 2011) and AKARI (Ishihara et al. 2010) and our volume-equivalent diameters $D_{\rm eq}$ for all 41 studied asteroids and plotted them in Fig. 7.5. In all three cases, the dispersion was ∼11% and we observed only a small systematic trend: diameters from IRAS and AKARI were in average ∼ 3% and ∼ 1% smaller, and diameters from WISE ∼ 5% larger. We can conclude that diameters derived from thermal observations and by scaling convex models to fit the AO images are in average consistent. Unlike the sizes based on infrared measurements, the sizes derived by comparing convex models

with AO observations are not biased by the observing geometry, and thus are more reliable. Infrared surveys assume for fitting the thermal measurements a spherical shape model (e.g., NEATM model Harris 1998). Because the thermal data are usually available only from one apparition, the resulting size strongly depends on the orientation of the asteroid, namely the position of its rotational axis with respect to the Earth. If the asteroid is observed pole-on, the size is overestimated (this orientation corresponds to the largest projected area of the asteroid). On the other hand, if we have thermal data observed in a configuration when the spin axis is perpendicular to the line connecting the observer and the asteroid (equator-on), the projected area is at minimum and we get an underestimated size. In average, the diameters from infrared surveys are reliable, but for individual asteroids (especially elongated once), the sizes could be shifted by more than about 30%.

Table 7.3: *List of volume-equivalent diameters $D_{\rm eq}^{(1)}$ (and $D_{\rm eq}^{(2)}$ for the mirror solution if any, if there are two solutions, their order is the same as in DAMIT or Table 5.1), effective diameters $D_{\rm IRAS}$, $D_{\rm WISE}$, $D_{\rm AKARI}$ derived from IRAS, WISE and AKARI infrared measurements, and volume-equivalent diameters $D_{\rm occ}^{(1)}$ (and $D_{\rm occ}^{(2)}$ for the mirror solution if any) derived by scaling the convex shape models to the stellar occultation measurements (Ďurech et al. 2011). The table also gives the references to the convex models and the number of AO images $N_{\rm AO}$ available for each asteroid.*

Asteroid	LC model reference	$N_{\rm AO}$	$D_{\rm eq}^{(1)}$ [km]	$D_{\rm eq}^{(2)}$ [km]	$D_{\rm IRAS}$ [km]	$D_{\rm WISE}$ [km]	$D_{\rm AKARI}$ [km]	$D_{\rm occ}^{(1)}$ [km]	$D_{\rm occ}^{(2)}$ [km]
5 Astraea	Ďurech et al. (2009)	1	107±14		119.1±6.5	115.0±9.4	110.8±1.4	116±6	
7 Iris	Kaasalainen et al. (2002b)	3	206±18	206±18	199.8±10.0		254.2±3.3	198±27	199±26
8 Flora	Torppa et al. (2003)	2	128±8	128±8	135.9±2.3	140.0±1.2	138.3±1.4	Wrong	140±7
9 Metis	Torppa et al. (2003)	2	144±10			204.5±3.7	166.5±2.1	169±20	
15 Eunomia	Kaasalainen et al. (2002b)	1	261±18		255.3±15.0	259.0±35.5	256.4±3.1		
16 Psyche	Kaasalainen et al. (2002b)	1	219±10	218±18	253.2±4.0		207.2±3.0	225±20	225±36
19 Fortuna	Torppa et al. (2003)	1	193±10			223.0±43.6	199.7±3.0		
23 Thalia	Torppa et al. (2003)	2	113±8	114±10	107.5±2.2		106.2±1.9		
28 Bellona	Hanuš et al. (2011)	1	128±14	125±8	120.9±3.4		97.4±1.4	98±11	100±10
29 Amphitrite	Kaasalainen et al. (2002b)	1	201±16		212.2±6.8	227.1±4.0	206.9±2.6		
30 Urania	Ďurech et al. (2009)	1	120±14	117±12	100.2±2.4	98.4±2.1	88.9±1.0		
37 Fides	Hanuš et al. (2011)	1	122±10	Wrong	108.3±1.9		103.2±1.4		
39 Laetitia	Kaasalainen et al. (2002b)	2	154±10		149.5±8.6	163.0±14.0	151.6±1.6	163±12	
40 Harmonia	Hanuš et al. (2011)	1	126±10	Wrong	107.6±6.2	119.7±1.3	110.3±1.3		
42 Isis	Hanuš et al. (2011)	1	97±6	Wrong	100.2±3.4		104.5±1.4		
45 Eugenia	Kaasalainen et al. (2002b)	13	176±20		214.6±4.2	206.1±6.2	183.6±2.9		
52 Europa	Kaasalainen et al. (2002b)	1	283±26		302.5±5.4	334.6±20.9	350.4±5.1	293±30	
54 Alexandra	Warner et al. (2008a)	2	133±8	Wrong	165.8±3.4	142.0±14.8	144.5±1.8	142±9	135±20
69 Hesperia	Hanuš et al. (2011)	1	116±8	116±6	138.1±4.7		132.7±1.5		
79 Eurynome	Hanuš et al. (2013)	1	Wrong	119±8	66.5±1.6	72.6±1.7	74.8±0.9		
80 Sappho	Ďurech et al. (2009)	2	74±6	Wrong	78.4±1.7	79.0±1.4	70.8±0.9	67±11	
85 Io	Ďurech et al. (2011)	1	158±10		154.8±3.8	163.0±18.6	150.7±1.9	163±15	
87 Sylvia	Kaasalainen et al. (2002b)	2	266±20		260.9±13.3	288.4±7.6	262.7±3.9		
88 Thisbe	Torppa et al. (2003)	1	224±16	Wrong	200.6±5.0		195.6±2.7	204±14	Wrong
89 Julia	Ďurech et al. (2011)	1	139±12		151.5±3.1	148.1±10.1	146.8±1.9	140±10	
97 Klotho	Hanuš et al. (2011)	1	83±6	Wrong	82.8±4.5	83.0±5.1	87.8±1.0		
107 Camilla	Torppa et al. (2003)	3	237±18		222.6±17.1	219.4±5.9	200.4±3.5	214±28	
129 Antigone	Torppa et al. (2003)	1	127±8			129.5±14.8	119.5±1.4		
130 Elektra	Marchis et al. (2006)	3	192±14		182.2±11.8	198.9±4.1	183.0±2.3		
146 Lucina	Ďurech et al. (2009)	2	122±10	120±10	132.2±2.4	131.8±4.8	126.9±1.6		
184 Dejopeja	Marciniak et al. (2007)	1	99±8	100±12	66.5±2.0	88.8±1.1	64.9±0.9		

Table 7.3: *continued.*

Asteroid	LC model reference	N_{AO}	$D_{\mathrm{eq}}^{(1)}$ [km]	$D_{\mathrm{eq}}^{(2)}$ [km]	D_{IRAS} [km]	D_{WISE} [km]	D_{AKARI} [km]	$D_{\mathrm{occ}}^{(1)}$ [km]	$D_{\mathrm{occ}}^{(2)}$ [km]
201 Penelope	Torppa et al. (2003)	1	88±6	Wrong	68.4±3.5	88.1±2.8	65.8±1.1		
230 Athamantis	Torppa et al. (2003)	1	120±8	120±12	109.0±2.0	109.0±13.0	108.3±1.2		
250 Bettina	Torppa et al. (2003)	1	113±16	116±16	79.8±4.6	121.3±2.0	109.4±1.5		
264 Libussa	Hanuš et al. (2011)	1	51±6	51±6	50.5±2.7	70.9±0.6	57.6±0.6		
276 Adelheid	Marciniak et al. (2007)	1	111±8	110±10	121.6±7.7	102.7±0.7	135.3±2.1	125±15	117±15
349 Dembowska	Torppa et al. (2003)	1	Wrong	168±18	139.8±4.3	216.7±7.4	164.7±1.8		
354 Eleonora	Hanuš et al. (2011)	1	152±12		155.2±8.5	165.0±15.6	149.6±2.0		
409 Aspasia	Warner et al. (2008a)	3	147±14		161.6±6.8	177.0±0.9	197.2±3.7	173±17	
423 Diotima	Marchis et al. (2006)	1	199±12		208.8±4.9	177.3±6.3	226.9±3.1		
714 Ulula	Hanuš et al. (2011)	1	59±10	58±8	39.2±2.4		44.3±0.5		

Chapter 8

Conclusions

The results of this Thesis can be briefly summarized as follows.

- We systematically gathered and processed all available sparse photometry from astrometric surveys and employed valuable data from seven observatories (see Table 3.1) in the lightcurve inversion.

- We showed that asteroid models based partialy or fully on sparse data are reliable. We presented several reliability tests that were applied on newly derived models.

- We optimized and automated the lightcurve inversion scheme to be used for thousands of asteroids without an excessive user interaction.

- For 282 asteroids, we derived convex shape models and rotational states from their combined dense and sparse disk-integrated photometry (58 models are based only on sparse data). The typical uncertainty of the sidereal rotational period is $\sim 10^{-5}$ h and 10°–20° of the pole direction. All new models will be included in DAMIT database.

- We derived 105 partial models, i.e., models with a unique rotational period, but multiple pole solutions with similar ecliptic latitudes β.

- We also derived 21 asteroid models based only on sparse data from the Catalina Sky Survey Observatory. The reliability of these models is supported by the fact that for eight of them, we got similar rotational period values that were previously reported in the literature and were derived from an independent data set (dense photometry). We do not have any previous information about the rotational periods for the other 13 asteroids. Due to the worse quality of the CSS sparse data, the typical uncertainty of the sidereal rotational period is $\sim 10^{-4} - 10^{-5}$ h and 20°–40° of the pole direction.

- By combining observations of stellar occultations by asteroids with derived convex shape models, we determined equivalent diameters for eight asteroids (Table 7.1).

- By combining disk-resolved images observed with the Keck II adaptive optics system with derived convex shape models, we determined equivalent

diameters for 41 asteroids (Table 7.3) and removed pole ambiguity for ten asetroids (Table 7.2).

- We investigate the spin vector distribution among MBAs and also four asteroidal families – Flora, Eunomia, Eos and Koronis.
- We constructed a simple dynamical model for the spin evolution of asteroids and compared the synthetic pole latitude distributions to the de-biased observed latitude distributions of 307 asteroids. Using several values (from 0.01 to 0.8) for the scaling parameter c_{YORP} defined by Equation (6.4), we constrained its value to $c_{\mathrm{YORP}} \in [0.05, 0.6]$. We interpreted the low value of c_{YORP} (<1) as a result of the surface roughness.

The de-biased observed ecliptic *longitude* distribution of asteroid spin vectors is independent of diameter and is compatible with a uniform distribution. Both the observed ecliptic longitude and latitude distributions are biased by the LI method. However, the effect of the lightcurve inversion bias is only minor and the global features of the observed longitude and latitude distributions do not change. The observed de-biased *latitude* distribution for asteroids with diameters $D > 60$ km shows an excess of prograde rotators in the latitude interval (11°, 90°). This excess is probably primordial. On the other hand, the latitude distributions for the entire sample and in particular for asteroids with $D < 30$ km, is strongly anisotropic.

The dynamical evolution of asteroid spins seems to be dominated by the YORP effect and also by collisions and mass shedding for asteroids with diameters $D \lesssim$ 30 km. We calculate that YORP (with a small contribution for the LI method's bias) is capable of producing the observed depopulation of spin vectors for small asteroids.

The observed spin distribution cannot be explained by using the Eqs. (6.3) without c_{YORP} as a free parameter ($c_{\mathrm{YORP}} = 1$). Only certain values of c_{YORP} produce synthetic spin distributions consistent with the observed spin distributions, and thus these values should be used in similar simulations to correctly account for the YORP effect.

In the future, quality sparse data sets will be produced by all-sky surveys such as Pan-STARRS, the Large Synoptic Survey Telescope (LSST), and the Gaia satellite. When these data are available, we will be able to apply the same methods to in order to derive more new asteroid models. These surveys will have one advantage over the dense data: their selection effects (e.g., with respect to the orbit) will be known. This will allow us to make a more accurate analysis of the asteroid population.

Acknowledgements This work has been supported by the grant GA UK 134710 of the Grant Agency of the Charles University in Prague, by the project SVV 265301 of the Charles University in Prague, by the grants GACR 205/08/H005 and GACR 209/10/0537 of the Grant Agency of the Czech Republic. The calculations were performed on the computational cluster Tiger at the Astronomical Institute of the Charles University in Prague (`http://sirrah.troja.mff.cuni.cz/tiger`). We also thank David Čapek for sending us the YORP effect data in an electronic form.

Bibliography

Barucci, M. A., Capria, M. T., Harris, A. W., & Fulchignoni, M. (1989). On the shape and albedo variegation of asteroids - Results from Fourier analysis of synthetic and observed asteroid lightcurves. *Icarus*, 78:311–322.

Barucci, M. A., Cellino, A., de Sanctis, C., et al. (1992). Ground-based Gaspra modelling - Comparison with the first Galileo image. *Astronomy and Astrophysics*, 266:385–394.

Bembrick, C. & Bolt, G. (2003). Lightcurves across Australia: period determination for minor planet (5647) 1990 TZ. *Minor Planet Bulletin*, 30:42–43.

Benavidez, P. G., Durda, D. D., Enke, B. L., et al. (2012). A comparison between rubble-pile and monolithic targets in impact simulations: Application to asteroid satellites and family size distributions. *Icarus*, 219:57–76.

Binzel, R. P., Slivan, S. M., Magnusson, P., et al. (1993). Asteroid 243 Ida - Groundbased photometry and a pre-Galileo physical model. *Icarus*, 105:310.

Bottke, J. W. F., Vokrouhlický, D., Rubincam, D. P., & Nesvorný, D. (2006). The Yarkovsky and Yorp Effects: Implications for Asteroid Dynamics. *Annual Review of Earth and Planetary Sciences*, 34:157–191.

Bottke, W. F., Vokrouhlický, D., Brož, M., Nesvorný, D., & Morbidelli, A. (2001). Dynamical Spreading of Asteroid Families by the Yarkovsky Effect. *Science*, 294:1693–1696.

Bowell, E., Hapke, B., Domingue, D., et al. (1989). Application of photometric models to asteroids. In Binzel, R. P., Gehrels, T., & Matthews, M. S., editors, *Asteroids II*, pages 524–556.

Bowell, E., Oszkiewicz, D. A., Wasserman, L., et al. (2011). Asteroid spin-axis longitudes from the Lowell observatory database. In *EPSC-DPS Joint Meeting 2011*, page 1549.

Brož, M., Vokrouhlický, D., Morbidelli, A., Nesvorný, D., & Bottke, W. F. (2011). Hilda Collisional Family Probably Affected by Planetary Migration. in press, MNRAS.

Burchi, R. & Milano, L. (1974). Photoelectric lightcurves of the minor planet 43 Ariadne during the 1972 opposition. *Astronomy and Astrophysics Supplement Series*, 15:173–180.

Čapek, D. & Vokrouhlický, D. (2004). The YORP effect with finite thermal conductivity. *Icarus*, 172:526–536.

Carbo, L., Kragh, K., Krotz, J., et al. (2009). Asteroid Lightcurve Analysis at the Oakley Southern Sky Observatory and Oakley Observatory: 2008 September and October. *Minor Planet Bulletin*, 36:91–94.

Cellino, A., Zappalá, V., di Martino, M., Farinella, P., & Paolicchi, P. (1987). Flattening, pole, and albedo features of 4 Vesta from photometric data. *Icarus*, 70:546–565.

Cellino, A., Zappalá, V., & Farinella, P. (1989). Asteroid shapes and lightcurve morphology. *Icarus*, 78:298–310.

Chapman, C. R. (2002). Cratering on Asteroids from Galileo and NEAR Shoemaker. *Asteroids III*, pages 315–329.

Cheng, A. F. (2002). Near Earth Asteroid Rendezvous: Mission Summary. *Asteroids III*, pages 351–366.

Davies, M. E., Colvin, T. R., Belton, M. J. S., et al. (1994). The North Pole Direction and the Control Network of the Asteroid 243 Ida. In *AAS/Division for Planetary Sciences Meeting Abstracts #26*, volume 26 of *Bulletin of the American Astronomical Society*, page 1154.

Davis, D. R., Weidenschilling, S. J., Farinella, P., Paolicchi, P., & Binzel, R. P. (1989). Asteroid collisional history - Effects on sizes and spins. In R. P. Binzel, T. Gehrels, & M. S. Matthews, editor, *Asteroids II*, pages 805–826.

Degewij, J., Tedesco, E. F., & Zellner, B. (1979). Albedo and color contrasts on asteroid surfaces. *Icarus*, 40:364–374.

Ditteon, R., Bixby, A. R., Sarros, A. M., & Waters, C. T. (2002). Rotation Periods and Lightcurves of 1858 Lobachevskij, 2384 Schulhof and (5515) 1989 EL1. *Minor Planet Bulletin*, 29:69.

Dobrovolskis, A. R. (1996). Inertia of Any Polyhedron. *Icarus*, 124:698–704.

Drummond, J., Eckart, A., & Hege, E. K. (1988a). Speckle interferometry of asteroids. IV - Reconstructed images of 4 Vesta. *Icarus*, 73:1–14.

Drummond, J. D., Weidenschilling, S. J., Chapman, C. R., & Davis, D. R. (1988b). Photometric geodesy of main-belt asteroids. II - Analysis of lightcurves for poles, periods, and shapes. *Icarus*, 76:19–77.

Drummond, J. D., Weidenschilling, S. J., Chapman, C. R., & Davis, D. R. (1991). Photometric geodesy of main-belt asteroids. IV - an updated analysis of lightcurves for poles, periods, and shapes. *Icarus*, 89:44–64.

Dunckel, P. B., Stephens, R., Oey, J., & Bernasconi, L. (2009). Shape and Spin Axis Model for 683 Lanzia. *Minor Planet Bulletin*, 36:48–49.

Dunham, D. W., Dunham, J. B., Binzel, R. P., et al. (1990). The size and shape of (2) Pallas from the 1983 occultation of 1 Vulpeculae. *Astronomical Journal*, 99:1636–1662.

Durda, D. D., Bottke, W. F., Nesvorný, D., et al. (2007). Size-frequency distributions of fragments from SPH/N-body simulations of asteroid impacts: Comparison with observed asteroid families. *Icarus*, 186:498–516.

Ďurech, J., Grav, T., Jedicke, R., Denneau, L., & Kaasalainen, M. (2005). Asteroid Models from the Pan-STARRS Photometry. *Earth Moon and Planets*, 97:179–187.

Ďurech, J., Kaasalainen, M., Herald, D., et al. (2011). Combining asteroid models derived by lightcurve inversion with asteroidal occultation silhouettes. *Icarus*, 214:652–670.

Ďurech, J., Kaasalainen, M., Warner, B. D., et al. (2009). Asteroid models from combined sparse and dense photometric data. *Astronomy and Astrophysics*, 493:291–297.

Ďurech, J., Scheirich, P., Kaasalainen, M., et al. (2007). Physical models of asteroids from sparse photometric data. In G. B. Valsecchi, D. Vokrouhlický, & A. Milani, editor, *IAU Symposium*, volume 236 of *IAU Symposium*, pages 191–200.

Ďurech, J., Sidorin, V., & Kaasalainen, M. (2010). DAMIT: a database of asteroid models. *Astronomy and Astrophysics*, 513:A46.

Farinella, P., Vokrouhlicky, D., & Hartmann, W. K. (1998). Meteorite Delivery via Yarkovsky Orbital Drift. *Icarus*, 132:378–387.

Galad, A. (2008). Part of Simple Lightcurves from Modra (October 2007- February 2008). *Minor Planet Bulletin*, 35:128–132.

Hanuš, J., Ďurech, J., Brož, M., et al. (2011). A study of asteroid pole-latitude distribution based on an extended set of shape models derived by the lightcurve inversion method. *Astronomy and Astrophysics*, 530:A134.

Hanuš, J., Ďurech, J., & el al. (2013). Asteroid physical models derived from combined dense and sparse photometry used for scaling of the YORP effect by the observed obliquity distribution. *Astronomy and Astrophysics*. Accepted January 15, 2013.

Harris, A. W. (1998). A Thermal Model for Near-Earth Asteroids. *Icarus*, 131:291–301.

Hill, G. (1982). Hermite. *Publ. Dom. Astrophys. Obs. Victoria BC*, 16, 67.

Hodapp, K. W., Kaiser, N., Aussel, H., et al. (2004). Design of the Pan-STARRS telescopes. *Astronomische Nachrichten*, 325:636–642.

Hom, E. F. Y., Marchis, F., Lee, T. K., et al. (2007). AIDA: An adaptive image deconvolution algorithm with application to multi-frame and three-dimensional data. *Journal of the Optical Society of America A: Optics and Image Science, and Vision*, 24(6):1580–1600.

Ishihara, D., Onaka, T., Kataza, H., et al. (2010). The AKARI/IRC mid-infrared all-sky survey. *Astronomy and Astrophysics*, 514:A1.

Ivezić, Z., Tyson, J. A., Acosta, E., et al. (2008). LSST: from Science Drivers to Reference Design and Anticipated Data Products. *ArXiv e-prints*.

Johansen, A. & Lacerda, P. (2010). Prograde rotation of protoplanets by accretion of pebbles in a gaseous environment. *Monthly Notices of the Royal Astronomical Society*, 404:475–485.

Kaasalainen, M. (2001). Interpretation of lightcurves of precessing asteroids. *Astronomy and Astrophysics*, 376:302–309.

Kaasalainen, M. (2004). Physical models of large number of asteroids from calibrated photometry sparse in time. *Astronomy and Astrophysics*, 422:L39–L42.

Kaasalainen, M. & Lamberg, L. (2006). Inverse problems of generalized projection operators. *Inverse Problems*, 22:749–769.

Kaasalainen, M., Lamberg, L., & Lumme, K. (1992a). Interpretation of lightcurves of atmosphereless bodies. II - Practical aspects of inversion. *Astronomy and Astrophysics*, 259:333–340.

Kaasalainen, M., Lamberg, L., Lumme, K., & Bowell, E. (1992b). Interpretation of lightcurves of atmosphereless bodies. I - General theory and new inversion schemes. *Astronomy and Astrophysics*, 259:318–332.

Kaasalainen, M., Mottola, S., & Fulchignoni, M. (2002a). Asteroid Models from Disk-integrated Data. *Asteroids III*, pages 139–150.

Kaasalainen, M., Pravec, P., Krugly, Y. N., et al. (2004). Photometry and models of eight near-Earth asteroids. *Icarus*, 167:178–196.

Kaasalainen, M. & Torppa, J. (2001). Optimization Methods for Asteroid Lightcurve Inversion. I. Shape Determination. *Icarus*, 153:24–36.

Kaasalainen, M., Torppa, J., & Muinonen, K. (2001). Optimization Methods for Asteroid Lightcurve Inversion. II. The Complete Inverse Problem. *Icarus*, 153:37–51.

Kaasalainen, M., Torppa, J., & Piironen, J. (2002b). Models of Twenty Asteroids from Photometric Data. *Icarus*, 159:369–395.

Karttunen, H. (1989). Modelling asteroid brightness variations. I - Numerical methods. *Astronomy and Astrophysics*, 208:314–319.

Karttunen, H. & Bowell, E. (1989). Modelling asteroid brightness variations. II - The interpretability of light curves and phase curves. *Astronomy and Astrophysics*, 208:320–326.

Kryszczynska, A., Colas, F., Berthier, J., Michałowski, T., & Pych, W. (1996). CCD Photometry of Seven Asteroids: New Spin Axis and Shape Determinations. *Icarus*, 124:134–140.

Kryszczyńska, A., La Spina, A., Paolicchi, P., et al. (2007). New findings on asteroid spin-vector distributions. *Icarus*, 192:223–237.

La Spina, A., Paolicchi, P., Kryszczyńska, A., & Pravec, P. (2004). Retrograde spins of near-Earth asteroids from the Yarkovsky effect. *Nature*, 428:400–401.

Lagerkvist, C., Barucci, M. A., Capria, M. T., et al. (1987). *Asteroid photometric catalogue.*

Lagerros, J. S. V. (1997). Thermal physics of asteroids. III. Irregular shapes and albedo variegations. *Astronomy and Astrophysics*, 325:1226–1236.

Lamberg, L. & Kaasalainen, M. (2001). Numerical solution of the Minkowski problem. *Journal of Computational and Applied Mathematics*, 137:213–227.

Larson, S., Beshore, E., Hill, R., et al. (2003). The CSS and SSS NEO surveys. In *AAS/Division for Planetary Sciences Meeting Abstracts #35*, volume 35 of *Bulletin of the American Astronomical Society*, page 982.

Magnusson, P. (1986). Distribution of spin axes and senses of rotation for 20 large asteroids. *Icarus*, 68:1–39.

Magnusson, P. (1990). Spin vectors of 22 large asteroids. *Icarus*, 85:229–240.

Maleszewski, C. & Clark, M. (2004). Bucknell University Observatory lightcurve results for 2003-2004. *Minor Planet Bulletin*, 31:93–94.

Marchis, F., Kaasalainen, M., Hom, E. F. Y., et al. (2006). Shape, size and multiplicity of main-belt asteroids. I. Keck Adaptive Optics survey. *Icarus*, 185:39–63.

Marciniak, A., Michałowski, T., Hirsch, R., et al. (2009a). Photometry and models of selected main belt asteroids. VII. 350 Ornamenta, 771 Libera, and 984 Gretia. *Astronomy and Astrophysics*, 508:1503–1507.

Marciniak, A., Michałowski, T., Hirsch, R., et al. (2009b). Photometry and models of selected main belt asteroids. VI. 160 Una, 747 Winchester, and 849 Ara. *Astronomy and Astrophysics*, 498:313–320.

Marciniak, A., Michałowski, T., Kaasalainen, M., et al. (2007). Photometry and models of selected main belt asteroids. IV. 184 Dejopeja, 276 Adelheid, 556 Phyllis. *Astronomy and Astrophysics*, 473:633–639.

Marciniak, A., Michałowski, T., Kaasalainen, M., et al. (2008). Photometry and models of selected main belt asteroids. V. 73 Klytia, 377 Campania, and 378 Holmia. *Astronomy and Astrophysics*, 478:559–565.

Marciniak, A., Michałowski, T., Polińska, M., et al. (2011). Photometry and models of selected main belt asteroids. VIII. Low-pole asteroids. *Astronomy and Astrophysics*, 529:A107.

Masiero, J. R., Mainzer, A. K., Grav, T., et al. (2011). Main Belt Asteroids with WISE/NEOWISE. I. Preliminary Albedos and Diameters. *Astrophysical Journal*, 741:68.

Merline, W. J., Close, L. M., Dumas, C., et al. (2000). Discovery of Companions to Asteroids 762 Pulcova and 90 Antiope by Direct Imaging. In *AAS/Division for Planetary Sciences Meeting Abstracts #32*, volume 32 of *Bulletin of the American Astronomical Society*, page 1017.

Michałowski, T. (1996). A new model of the asteroid 532 Herculina. *Astronomy and Astrophysics*, 309:970–978.

Michałowski, T., Kaasalainen, M., Marciniak, A., et al. (2005). Photometry and models of selected main belt asteroids. II. 173 Ino, 376 Geometria, and 451 Patientia. *Astronomy and Astrophysics*, 443:329–335.

Michałowski, T., Kaasalainen, M., Polińska, M., et al. (2006). Photometry and models of selected main belt asteroids. III. 283 Emma, 665 Sabine, and 690 Wratislavia. *Astronomy and Astrophysics*, 459:663–668.

Michałowski, T., Kwiatkowski, T., Kaasalainen, M., et al. (2004). Photometry and models of selected main belt asteroids I. 52 Europa, 115 Thyra, and 382 Dodona. *Astronomy and Astrophysics*, 416:353–366.

Molnar, L. A., Haegert, J. M., Beaumont, C. N., et al. (2008). Lightcurve Analysis of a Magnitude Limited Asteroid Sample. *Minor Planet Bulletin*, 35:9–12.

Morbidelli, A. & Vokrouhlický, D. (2003). The Yarkovsky-driven origin of near-Earth asteroids. *Icarus*, 163:120–134.

Mottola, S. & Lahulla, F. (2000). Mutual Eclipse Events in Asteroidal Binary System 1996 FG_3: Observations and a Numerical Model. *Icarus*, 146:556–567.

Muinonen, K., Piironen, J., Shkuratov, Y. G., Ovcharenko, A., & Clark, B. E. (2002). Asteroid Photometric and Polarimetric Phase Effects. *Asteroids III*, pages 123–138.

Müller, T. G., Ďurech, J., Hasegawa, S., et al. (2011). Thermo-physical properties of 162173 (1999 JU3), a potential flyby and rendezvous target for interplanetary missions. *Astronomy and Astrophysics*, 525:A145.

Nesvorný, D. (2012). Nesvorny HCM Asteroid Families V2.0. *NASA Planetary Data System*, 189.

Nesvorný, D. & Bottke, W. F. (2004). Detection of the Yarkovsky effect for main-belt asteroids. *Icarus*, 170:324–342.

Ostro, S. J. & Connelly, R. (1984). Convex profiles from asteroid lightcurves. *Icarus*, 57:443–463.

Ostro, S. J., Connelly, R., & Dorogi, M. (1988). Convex-profile inversion of asteroid lightcurves - Theory and applications. *Icarus*, 75:30–63.

Ostro, S. J., Hudson, R. S., Benner, L. A. M., et al. (2002). Asteroid Radar Astronomy. *Asteroids III*, pages 151–168.

Ostro, S. J., Hudson, R. S., Nolan, M. C., et al. (2000). Radar Observations of Asteroid 216 Kleopatra. *Science*, 288:836–839.

Oszkiewicz, D. A., Muinonen, K., Bowell, E., et al. (2011). Online multi-parameter phase-curve fitting and application to a large corpus of asteroid photometric data. *Journal of Quantitative Spectroscopy & Radiative Transfer*, 112:1919–1929.

Perryman, M. A. C., de Boer, K. S., Gilmore, G., et al. (2001). GAIA: Composition, formation and evolution of the Galaxy. *Astronomy and Astrophysics*, 369:339–363.

Piironen, J., Lagerkvist, C., Torppa, J., Kaasalainen, M., & Warner, B. (2001). Standard Asteroid Photometric Catalogue. In *Bulletin of the American Astronomical Society*, volume 33 of *Bulletin of the American Astronomical Society*, page 1562.

Polishook, D., Ofek, E. O., Waszczak, A., et al. (2012). Asteroid rotation periods from the Palomar Transient Factory survey. *Monthly Notices of the Royal Astronomical Society*, 421:2094–2108.

Pravec, P. & Hahn, G. (1997). Two-Period Lightcurve of 1994 AW_1: Indication of a Binary Asteroid? *Icarus*, 127:431–440.

Pravec, P. & Harris, A. W. (2000). Fast and Slow Rotation of Asteroids. *Icarus*, 148:12–20.

Pravec, P., Harris, A. W., & Michałowski, T. (2002). Asteroid Rotations. *Asteroids III*, pages 113–122.

Press, W. H., Flannery, B. P., & Teukolsky, S. A. (1986). *Numerical recipes. The art of scientific computing*. Cambridge: University Press, 1986.

Press, W. H., Flannery, B. P., Teukolsky, S. A., & Vetterling, W. T. (1994). Numerical Recipes in Fortran. *Cambridge Univ. Press, Cambridge, UK*.

Rau, A., Kulkarni, S. R., Law, N. M., et al. (2009). Exploring the Optical Transient Sky with the Palomar Transient Factory. *Publications of the Astronomical Society of the Pacific*, 121:1334–1351.

Rozitis, B. & Green, S. F. (2012). The influence of rough surface thermal-infrared beaming on the Yarkovsky and YORP effects. *Monthly Notices of the Royal Astronomical Society*, 423:367–388.

Rubincam, D. P. (2000). Radiative Spin-up and Spin-down of Small Asteroids. *Icarus*, 148:2–11.

Russell, H. N. (1906). On the light variations of asteroids and satellites. *Astrophysical Journal*, 24:1–18.

Scheeres, D. J. & Mirrahimi, S. (2007). Evolution of Asteroid Rotation States Subject to the YORP Effect. In *Bulletin of the American Astronomical Society*, volume 38 of *Bulletin of the American Astronomical Society*, page 416.

Skoglöv, E. & Erikson, A. (2002). The Influence of the Orbital Evolution of Main Belt Asteroids on Their Spin Vectors. *Icarus*, 160:24–31.

Slivan, S. M. (2002). Spin vector alignment of Koronis family asteroids. *Nature*, 419:49–51.

Slivan, S. M., Binzel, R. P., Crespo da Silva, L. D., et al. (2003). Spin vectors in the Koronis family: comprehensive results from two independent analyses of 213 rotation lightcurves. *Icarus*, 162:285–307.

Slivan, S. M., Binzel, R. P., Kaasalainen, M., et al. (2009). Spin vectors in the Koronis family. II. Additional clustered spins, and one stray. *Icarus*, 200:514–530.

Slivan, S. M. & Molnar, L. A. (2012). Spin vectors in the Koronis family: III. (832) Karin. *Icarus*, 220:1097–1103.

Statler, T. S. (2009). Extreme sensitivity of the YORP effect to small-scale topography. *Icarus*, 202:502–513.

Tedesco, E. F., Noah, P. V., Noah, M., & Price, S. D. (2002). The Supplemental IRAS Minor Planet Survey. *Astronomical Journal*, 123:1056–1085.

Tedesco, E. F., Noah, P. V., Noah, M., & Price, S. D. (2004). IRAS Minor Planet Survey V6.0. *NASA Planetary Data System*, 12.

Torppa, J., Kaasalainen, M., Michałowski, T., et al. (2003). Shapes and rotational properties of thirty asteroids from photometric data. *Icarus*, 164:346–383.

Veverka, J., Robinson, M., Thomas, P., et al. (2000). NEAR at Eros: Imaging and Spectral Results. *Meteoritics amp Planetary Science, vol. 35, Supplement, p.A164*, 35.

Vokrouhlický, D., Brož, M., Morbidelli, A., et al. (2006a). Yarkovsky footprints in the Eos family. *Icarus*, 182:92–117.

Vokrouhlický, D., Nesvorný, D., & Bottke, W. F. (2003). The vector alignments of asteroid spins by thermal torques. *Nature*, 425:147–151.

Vokrouhlický, D., Nesvorný, D., & Bottke, W. F. (2006b). Secular spin dynamics of inner main-belt asteroids. *Icarus*, 184:1–28.

Warner, B. D., Durech, J., Fauerbach, M., & Marks, S. (2008a). Shape and Spin Models for Four Asteroids. *Minor Planet Bulletin*, 35:167–171.

Warner, B. D., Harris, A. W., & Pravec, P. (2009). The asteroid lightcurve database. *Icarus*, 202:134–146.

Warner, B. D., Higgins, D., Pray, D. P., et al. (2008b). A Shape and Spin Model for 1600 Vyssotsky. *Minor Planet Bulletin*, 35:13–14.

Wizinowich, P., Acton, D. S., Shelton, C., et al. (2000). First Light Adaptive Optics Images from the Keck II Telescope: A New Era of High Angular Resolution Imagery. *Publications of the Astronomical Society of the Pacific*, 112:315–319.

Yeung, K. W. (2006). Lightcurve analysis for 19848 Yeungchuchiu. *Minor Planet Bulletin*, 33:49.

Yoshida, F., Dermawan, B., Nakamura, T., et al. (2005). Yoshida, F., Dermawan, B., Nakamura, T., Ito, T., Takahashi, S., Ibrahimov, M. A., Malhotra, R., Ip, W.H., Chen, W. P.: Asia-Oceana Geophys. Soc. abstract 58-PS-A1103. *Abstr. IAU Symp. 229*, page 82.

Zappalá, V., Cellino, A., Farinella, P., & Knežević, Z. (1990). Asteroid families. I - Identification by hierarchical clustering and reliability assessment. *Astronomical Journal*, 100:2030–2046.

Zappalá, V., Cellino, A., Farinella, P., & Milani, A. (1994). Asteroid families. 2: Extension to unnumbered multiopposition asteroids. *Astronomical Journal*, 107:772–801.